

On the optimization of laser shock peening induced residual stresses

Dem Promotionsausschuss der
Technischen Universität Hamburg-Harburg

zur Erlangung des akademischen Grades

Doktor-Ingenieur (Dr.-Ing.)

genehmigte Dissertation

von

Sergey Chupakhin

aus

Kursk, Russland

2017

1. Gutachter: Herr Prof. Dr.-Ing. habil. Norbert Huber

2. Gutachter: Herr Prof. Dr.-Ing. habil. Alexander Düster

Vorsitzender des Prüfungsausschusses: Herr Prof. Dr. rer. nat. Gerold Schneider

Tag der mündlichen Prüfung: 06.12.2017

Dedication

This dissertation is dedicated to the memory of my father, Sergey Ivanovich Chupakhin. Although he was my inspiration to pursue my doctoral degree, he was unable to see my graduation. But I still feel his impact every day. I greatly value his constant support and encouragement and deeply appreciate his belief in me.

My father used to take me with him to change his car system. I was directly involved in unscrewing the system taking it to pieces and my eyes were glued to the inner mechanics of the machine. He was always explaining me the serving functions of thin wires of different colors, gears that turned in unending circles and the microchips. At that time my passion for engineering and designing was sparked.

Now I see so much of him in myself – always spending more time (sometimes unproductive) trying to enhance the quality of a final product, rethinking the same thing over and over by looking at the problem from different perspectives. He would never be afraid of taking responsibility in difficult situations where a chance to fail was so high.

My father raised me with integrity, unconditional love and hard work. He would never talk to me directly about my achievements but he always praised me to his friends and colleagues. Dad did not teach me how to live but he let me watch him do it.

I remember once he said to me: “Son, I cannot imagine myself working on things I am not passionate about because I will never truly succeed in them, and so shouldn’t you do. Do not ever stop searching for your passion.” These words have always been on my mind ever since.

Dad, as you look down from heaven, I hope you’re proud of your son.

Acknowledgments

Firstly, I would like to express my sincere gratitude to my supervisor Prof. Norbert Huber for the continuous support of my Ph.D study and related research, for his patience, motivation, and immense knowledge. I would like to thank him for encouraging my research and for allowing me to grow as a research scientist. His guidance helped me in all the time of research and writing of this thesis. I could not have imagined having a better mentor for my Ph.D study.

Besides my supervisor, I would like to thank the rest of my thesis committee: Prof. Alexander Düster and Prof. Gerold Schneider, for their insightful comments and encouragement, but also for the hard question which incited me to widen my research from various perspectives.

I record my deep sense of gratitude to Dr. Nikolai Kashaev who provided me an opportunity to join his team, and who gave access to the laboratory and research facilities. Under his guidance, I was given the freedom to pursue my research in my own way and I greatly appreciated that freedom. It was a great pleasure to work and discuss with him despite his busy schedules. Thanks for supporting and encouraging me during travels for conferences and hard work and for sharing his wealth of knowledge.

I would like to thank Prof. Benjamin Klusemann for his constant academic support, helpful discussions and valuable suggestion in my quest for knowledge. I am very grateful for his interest in my work and beneficial cooperation.

A very special gratitude goes to Leonardo Moura, Görkem Günay and Arden Phua for their support during residual stress measurement and fatigue testing. It was fantastic to work shoulder to shoulder with you, conduct experimental research and discuss results.

I wish to express my gratitude to Stefan Riekehr, René Dinse and Kay Erdmann for their technical assistance with experimental facilities, Manfred Horstmann and Hamdi Tek for conducting mechanical tests, Falk Dorn for assistance with specimen preparation. I offer many thanks to Dr. Volke Ventzke and Peter Haack for valuable discussions of material structure and properties. I also appreciate support and resources provided by Dr. Peter Staron and Dr. Emad Maawad during synchrotron measurements.

I thank my fellow labmates Alexandre Amorim Carvalho, Födor Fomin, Sören Keller, Dr. Jin Lu and Dr. Jie Liu for the stimulating and pleasant discussions, for the sleepless nights we were working together before deadlines, and for all the fun we had had in the last four years. Also I thank all my group members in WMF for a pleasant and friendly working atmosphere. I truly treasure my time here.

I would like to thank my friends for accepting nothing less than excellence from me.

Words can not express how grateful I am to Liliya Akbasheva for her unconditional love, patience and sincere loyalty. She has been a constant source of support and encouragement and has made an untold number of sacrifices on my behalf. She is a great inspiration to me.

My acknowledgement would be incomplete without thanking the biggest source of my strength, my family. The blessings of my parents Sergey Ivanovich Chupakhin and Alla Batalina and care of my brother Andrew Chupakhin, have made a tremendous contribution in helping me reach this stage in my life. I thank them for putting up with me in difficult moments where I felt stumped and for goading me on to follow my dream of getting this degree. This would not have been possible without their unwavering and unselfish love and support given to me at all times.

Preface

The basis for this research originally stemmed from my passion for developing new methods for solving complex engineering problems, which I believe can contribute to technical progress in modern aerospace engineering. I became fascinated by aviation during my study at Bauman Moscow State Technical University which is regarded as a forge of Russian engineers. Many Bauman University graduates are world-renowned: Sergey Korolev for the first satellite in the space and first man and woman in the space, Andrey Tupolev for the world first supersonic passenger plane, Nikolay Dollezhal for the world first civil nuclear plant, Vladimir Shukhov for the world first petrol cracking plant as well as for the first hyperboloid structures in architecture, Nikolay Zhukovsky for the foundation of aerodynamics and hydrodynamics sciences, Pavel Sukhoi for outstanding work in the field of aeronautical science and engineering. I knew, one day I would start my own research in the aerospace field.

When I was working on my master thesis with the topic of laser beam welding of lightweight aluminum structures at the Helmholtz-Zentrum Geesthacht I was thinking of pursuing Ph.D work in aerospace engineering. And then I came across a story that played an important role in my subsequent choice. The story was about an aircraft incident of Aeroflot Flight 1491. This was a scheduled domestic passenger flight in the USSR that crashed on 18 May 1972 while descending to land in Kharkiv, which led to death of 122 passengers and crew aboard the Antonov An-10.

The probable cause of the crash was determined to be the center wing section failing due to a fatigue crack in the lower central wing panel. In the 60-70s the problem of the fatigue crack growth was not well investigated. Antonov An-10 was as a four-engined turboprop passenger transport aircraft developed in Antonov design bureau. After this accident, Aeroflot ceased the operation of An-10. But the tragic lesson regarding the fatigue resistance of the aircraft fuselage was learnt. And after several years of intensive experimental and computational research on fatigue behavior of fuselage structures, the Antonov design bureau came up with a completely new design of two giant aircrafts: Antonov An-124 Ruslan and Antonov An-225 Mriya. These aircrafts absorbed all the most modern ideas that have appeared in the world's aircraft design regarding fatigue resistance. The An-124 was, for thirty years, the world's heaviest gross weight production cargo airplane. While the An-225, a specialized shuttle-carrying/extra-heavy cargo derivative, has set up 240 world records including transportation of the heaviest cargo with mass of 253 tons, the heaviest single piece of cargo with mass of 186.7 t as well as the longest cargo having a length of 42.1 meters.

The huge technical breakthrough in aircraft construction has encouraged me to start a Ph.D work regarding the fatigue life improvement of lightweight structures through laser shock peening. The great aviation achievements of mankind were always the driving force throughout my work

and particularly at the experimental stage. By finishing I would like to cite a general designer of Antonov design bureau:

“Sometimes inexpensive and simple change of an aircraft, vehicle or machine can enhance the working accuracy and performance or can even give new properties to machines. Modification is always cheaper and faster than designing new aircraft or locomotive”.

O. K. Antonov
Aircraft designer

On the optimization of laser shock peening induced residual stresses

Sergey Chupakhin

*Institute of Materials Research, Materials Mechanics, Helmholtz-Zentrum Geesthacht,
21502 Geesthacht, Germany.*

Contact: sergey.chupakhin@hzg.de

Abstract

There is a strong economic motivation of the aircraft industry to explore novel residual stress-based approaches for the fatigue life extension, repair, and maintenance of the growing fleet of ageing aircrafts, although the effect of residual stresses is not taken into account by the established damage tolerance evaluation methods. Laser shock peening — the most promising life enhancement technique — has already demonstrated great success in regard to the mitigation of fatigue crack growth via deep compressive residual stresses. However, no comprehensive model exists which allows the prediction of generated residual stress fields depending on the laser peening parameters.

Furthermore, the hole drilling method — a well-established technique for determining non-uniform residual stresses in metallic structures — is based on measuring strain relaxations at the material surface caused by the stress redistribution while drilling the hole. However, the hole drilling method assumes linear elastic material behavior and therefore, when measuring high residual stresses approaching the material yield strength, plastic deformation occurs, which in turn leads to errors in stress determination.

In the light of these two points, the present work aims to optimize the laser shock peening process in regard to high residual stress profiles, their correct measurement by the hole drilling method and demonstration of the fatigue crack growth retardation through the laser peening treatment on the laboratory scale.

First, the methodology for the correction of the residual stresses approaching the material yield strength when measuring by the hole drilling is established and experimentally validated. The correction methodology utilizes FE modelling and artificial neural networks. In contrast to the recent studies, the novelty of this methodology lies in the practical and elegant way to correct any non-uniform stress profile for a wide range of stress levels and material behaviors typically

used in industrial applications. Therefore, this correction methodology can be applied in industry without changing the procedure of hole drilling measurement.

Second, the laser shock peening process is optimized in regard to the generated residual stress profiles using design of experiments techniques. The strategy involves laser peening treatment with different parameters and subsequent measurement of induced residual stress profiles through hole drilling. The measured stress profiles are subjected to correction using the neural network methodology. After that the regression model is fitted into the experimental data in order to find the relationship between the laser peening parameters and the stress profiles' shapes. In the final stage, it is experimentally demonstrated that the established regression model provides an accurate prediction of the residual stress profile when using defined laser peening parameters and vice versa.

Third, the regression model obtained in the design of experiments study is used for generating the desired residual stresses in the C(T)50 AA2024-T3 specimens for the fatigue crack propagation test. Significant retardation of the fatigue crack propagation of specimens due to the presence of deep compressive residual stresses is experimentally demonstrated on the laboratory scale.

Über die Optimierung der durch Laser-Shock-Peening-Behandlung induzierten Eigenspannungen

Sergey Chupakhin

*Institut für Werkstoffforschung, Werkstoffmechanik, Helmholtz-Zentrum Geesthacht,
21502 Geesthacht, Deutschland.*

Kontakt: sergey.chupakhin@hzg.de

Zusammenfassung

Die Flugzeugindustrie sucht nach neuen kosteneffizienten Ansätzen zur Erhöhung der Lebensdauer von Komponenten sowie zur Durchführung von Reparatur- und Wartungsarbeiten an zunehmend älter werdenden Flugzeugen. Ein vielversprechender Lösungsansatz besteht in der Anwendung von Verfahren zur Erzeugung von oberflächennahen Eigenspannungen, um Rissinitiierung zu vermeiden sowie die Ausbreitung bereits vorhandener Risse zu verzögern.

Jedoch unterliegen konventionelle Oberflächenmodifikationsverfahren gewissen Einschränkungen hinsichtlich der maximalen Eigenspannungswerten, der erzielbaren Eindringtiefen von Druckeigenspannungen und, aufgrund von geometrischen Randbedingungen, der Komplexität der zu behandelnden Strukturen. Daher gibt es eine starke ökonomische Motivation der Industrieunternehmen, neuartige eigenspannungsbasierte Ansätze der Ermüdungslebensdauer zu erforschen, obwohl der Effekt der Eigenspannungen nicht in den etablierten Regelwerken des Schadentoleranzdesigns berücksichtigt wird.

Das Laser Shock Peening (LSP) ist eine vielversprechende Methode, höhere Lebensdauern zu erzielen. Es hat sich gezeigt, dass lasergenerierte Druckeigenspannungen in Strukturen eine Verlangsamung der Ermüdungsrissausbreitung bewirken. Jedoch existiert aufgrund der Komplexität des LSP-Prozesses kein umfassendes Modell, das die Vorhersage von Eigenspannungsfeldern in Abhängigkeit der Prozessparameter erlaubt, weshalb eine Erhöhung der Lebensdauer durch Anwendung des LSP-Prozesses schwierig vorhersagbar ist.

Darüber hinaus ist die Bohrlochmethode eine bewährte Technik zur ortsabhängigen Bestimmung von Eigenspannungen in metallischen Strukturen durch Messung von Dehnungsrelaxationen in der Umgebung eines an der Materialoberfläche eingebrachten Bohrlochs. Die Berechnung von Eigenspannungswerten aus den gemessenen Dehnungsrelaxationen basiert hierbei auf der Annahme, dass linear-elastisches Materialverhalten vorliegt und demzufolge die Eigenspannungswerte geringer als die Streckgrenze sind. Messbohrungen, welche infolge

Überschreitung der Streckgrenze zu plastischen Verformungen in der Bohrlochumgebung führen, liefern jedoch ein verfälschtes Ergebnis. Daher ist zunächst die Entwicklung einer Methode erforderlich, mit der die durch plastische Verformung verfälschte Ergebnisse entsprechend korrigiert werden können und die zudem auf ein breites Spektrum von LSP-behandelten Werkstoffen anwendbar ist.

Ziel der vorliegenden Arbeit ist es, eine praktisch anwendbare Methode zur Korrektur der mit der Bohrlochmethode gemessenen Eigenspannungen zu entwickeln, auf diesem Wege um die Auswirkung der LSP-Behandlung auf das Ermüdungsrisswachstum präzise zu ermitteln und für die Einbringung maßgeschneiderter Eigenspannungsmessungen zu nutzen.

Im ersten Schritt wird die Methode zur Korrektur der mittels Bohrlochmethode bestimmten Eigenspannungen entwickelt, die bis zur Streckgrenze des Werkstoffes reichen können. Diese Korrekturmethode basiert auf der Kombination von Finite-Element-Modellierung und der Anwendung eines neuronalen Netzes. Die experimentelle Validierung der Korrekturmethode erfolgte durch Dreipunktbiegeversuche an der Aluminiumlegierung AA2024-T3 durch Messung von Spannungsprofilen mit linearem Gradient. Die Anwendbarkeit der entwickelten Korrekturmethode für die Messung der durch die LSP-Behandlung generierten hohen Eigenspannungen wird demonstriert. Im Unterschied zur Literatur besteht die Neuheit der entwickelten Korrekturmethode darin, dass in praktischer und eleganter Weise ein breites Spektrum an Eigenspannungsprofilen für unterschiedliches Werkstoffverhalten bestimmt und korrigiert werden kann ohne dass das Messverfahren an sich geändert werden müsste. Diese Korrekturmethode kann auch deshalb in der Industrie eingesetzt werden.

Im zweiten Schritt wird der LSP-Prozess hinsichtlich der erzeugten Eigenspannungsprofile mit Hilfe der statistischen Versuchsplanung (Design of Experiment) optimiert. Diese Vorgehensweise umfasst LSP-Behandlungen mit unterschiedlichen Parametern und anschließender Messung von LSP-induzierten Eigenspannungsprofilen mit der Bohrlochmethode. Danach wird das Regressionsmodell in die experimentellen Daten eingepasst, um Beziehungen zwischen LSP-Parametern und Eigenspannungsprofilen zu identifizieren. Mittels Experimenten wird gezeigt, dass das Regressionsmodell geeignet ist, eine genaue Vorhersage eines Eigenspannungsprofils durch Vorgabe von LSP-Parametern zu treffen und umgekehrt.

Im dritten Schritt wird das Regressionsmodell zur gezielten Erzeugung von Eigenspannungen in C(T)50-Proben, an denen Ermüdungsrissausbreitungsversuche durchgeführt werden, angewendet. Die Ermüdungsrissausbreitungsversuche zeigen, dass die Ermüdungsrissausbreitung in AA2024-T3 durch LSP-generierte Druckeigenspannungen erschwert wird. Die nachgewiesene signifikante Lebensdauererhöhung liefert die notwendige

Voraussetzung für die Akzeptanz des LSP-Verfahrens zur Behandlung von metallischen Strukturen seitens der Industrie.

Abschließend wird gezeigt, (i) dass die aus der Kombination von FEM und neuronalem Netz entwickelte Korrekturmethode eine robuste Bestimmung auch bei stark ungleichmäßigen Spannungsprofilen in unterschiedlichen Materialien ermöglicht; (ii) das Regressionsmodell eine Vorhersage der Eigenspannungsprofile durch Vorgabe von LSP-Prozessparametern liefert, was zur Kosteneffizienz beiträgt; (iii) wird für den Labormaßstab gezeigt, dass LSP die Lebensdauer von Aluminiumstrukturen der Luftfahrt signifikant erhöht.

Contents

1. Introduction	1
1.1 Motivation and objectives.....	1
1.2 Approach.....	4
1.3 Structure of the thesis	5
2. State of the art	7
2.1 Residual stresses	7
2.2 Residual stress modification techniques	7
2.2.1 Cold expansion.....	8
2.2.2 Shot peening.....	9
2.2.3 Low-plasticity burnishing and deep-rolling.....	9
2.2.4 Laser heating.....	11
2.2.5 Laser shock peening.....	11
2.2.6 Comparison of laser shock peening and the established processes	13
2.2.7 Challenges of LSP process optimization	15
2.3 Residual stress measurement techniques	18
2.3.1 Challenges of measuring residual stresses.....	18
2.3.2 Relaxation measurement methods	18
2.4 Fatigue life extension via the residual stresses generated by the LSP	24
2.4.1 High-cycle fatigue.....	24
2.4.2 Fatigue crack propagation.....	26
3. Methods	33
3.1 Experimental techniques.....	33
3.1.1 Material: AA2024-T3	33
3.1.2 Laser shock peening.....	33
3.1.3 Hole drilling system “Prism”	34
3.1.4 Three-point bending.....	35
3.1.5 Fatigue crack propagation test	36

3.1.6 Design of experiments	37
3.2 Numerical methods	41
3.2.1 Integral method	41
3.2.2 Finite element method.....	44
3.2.3 Artificial neural network.....	47
4. Methodology for correction of measured residual stresses	51
4.1 FE model validation.....	51
4.2 Application of the methodology to LSP-shaped stress profiles.....	54
4.3 Solution of inverse problem of stress correction using artificial neural networks	55
4.3.1 Identification of residual stress profile	56
4.3.2 Sensitivity of the neural networks to noise	64
4.3.3 Application to measured LSP residual stress fields.....	66
4.4 Conclusions.....	69
5. Optimization of laser shock peening process using design of experiments..	71
5.1 DOE: planning stage.....	71
5.2 DOE: factor screening analysis.....	72
5.2.1 Response <i>stress at 0.01 mm</i>	72
5.2.2 Response <i>stress area</i>	77
5.2.3 Response <i>stress at 0.5 mm</i>	81
5.3 DOE: optimization of LSP process regarding the residual stresses.....	85
5.4 DOE: experimental verification of the regression model	90
5.5 DOE based on corrected residual stress profiles	91
5.5.1 Correction of measured residual stresses through the established methodology.....	91
5.5.2 Correction of the DOE regression model.....	92
5.6 Application of residual stresses for improvement of fatigue crack growth behavior	94
5.7 Conclusions.....	98
6. Summary and conclusions.....	101
7. Bibliography	105

List of abbreviations

LSP	laser shock peening
ESPI	electronic speckle pattern interferometry
IM	integral method
DOE	design of experiments
FE	finite element
ANN	artificial neural network
C(T)	compact tension specimen
HZG	Helmholtz-Zentrum Geesthacht
ABAQUS	finite element analysis software
AA	aluminium alloy
Nd:YAG	neodymium-doped yttrium aluminium garnet
Q-Switched	giant laser pulse formation
HV	Vickers hardness
ASTM	American Society for Testing and Materials
COD	crack opening displacement
ReliaSoft DOE++	design of experiments software
MSC Patran	finite element analysis software
SF	stress factor
RS	residual stress
PD	predefined stress profile in hole drilling simulation
FCP	fatigue crack propagation

BM	base material
RD	rolling direction of a specimen
PEEQ	equivalent plastic strain in ABAQUS

1. Introduction

1.1 Motivation and objectives

The residual stresses induced in aircraft structures or components by production processes or surface modification techniques play an important role in the evaluation of damage tolerance [1]. In most cases, unwillingly induced residual stresses, for instance by welding or forging, decrease the fatigue life of aircraft structures, while laser shock peening or cold extension treatments enhance the fatigue behavior [2–4].

For many decades, scientists and engineers have been developing the approaches that allow for the accounting of residual stresses in the assessment of the fatigue crack propagation in metallic structures [5–10]. Originally, the study in this field was aimed at the investigation of the fatal residual stresses induced by production processes, because they clearly affected the fatigue performance of the components. As a result, special material manufacturing and processing conditions and subsequent heat treatment were established in production, providing significant mitigation of the residual stress formation. Subsequently, the research focus shifted to the development of simulation models, allowing for the prediction of fatigue crack propagation in metallic aircraft structures with existing residual stresses [7, 8, 10]. This has led to a rise in the development of surface modification techniques such as shot peening, cold expansion, surface finishing, etc. [2], all based on the same principle — the intentional generation of compressive residual stresses for the suppression of crack initiation or the mitigation of crack growth in the aircraft components. These techniques provide cost-efficient solutions for the repair and service of the growing fleet of ageing aircrafts [1].

The extensive studies of fatigue behavior of treated metallic structures have demonstrated significant life improvement, but the evaluation is rather of a qualitative nature than quantitative, because of the extreme difficulties of residual stress assessment in the components after the various manufacturing processes, and, moreover, because the residual stress state is changed during the exploitation period of time about 30 years for aircraft [1, 11]. For this reason, the residual stresses are not comprehensively regulated in damage tolerance evaluation and the accounting of the positive effect of residual stresses on the fatigue performance in damage tolerance behavior is denied by the authorities [12, 13].

Even though damage tolerance evaluation does not account for the residual stresses, the surface modification techniques have been extensively used in the few last decades in various industrial applications and have demonstrated significant cost reduction in service and repair, particularly in respect of the components under cycle loading, such as occurring in turbine blades [1, 2]. The manufacturers and operators have always been investing the resources in the improvement of existing treatment technologies and have been supporting the development of methods with the aim of obtaining economic benefits.

There is a strong economic motivation for industrial companies to explore the novel approaches of fatigue life improvement, because of the limitations of existing surface modification techniques regarding the residual stress maximum depth of approximately 0.5 mm or geometrical restrictions of the treated structures, such as holes or flat surfaces. One such promising approach is laser shock peening (LSP), which has already demonstrated great success in regard to the mitigation of fatigue crack growth, but is not comprehensively established in terms of the quantitative prediction of fatigue behavior [3, 14–17]. LSP has been adopted by many companies such as Toshiba, Rolls-Royce, Metal Improvement Company, LSP Technologies, Boeing, U.S. Air Force, etc. However, the fatigue life extension of treated components is not precisely defined; i.e. only a rough (and usually not reproducible) estimation of a number of cycles until failure of the structure is provided. In this regard, the development of a numerical model to predict fatigue life behavior depending on the process parameters would enhance the efficiency of LSP treatment and help to further decrease the operation cost. This does, however, first need a solid experimental and theoretical foundation.

LSP generates deep compressive residual stresses in the material, increasing the resistance against fatigue crack propagation and can prevent crack initiation [3, 17, 18]. There is a lack of knowledge regarding the prediction of residual stress profiles in dependence of the LSP parameters. Therefore, research should be focused more on the optimization of the LSP process parameters.

The hole drilling method — a well-known technique for measuring residual stresses in metallic structures — has received much attention over the last 30 years. This is particularly true since it was adapted for determining non-uniform stress fields [19–21]. The rising popularity of this method is related to its simple and practical realization in many applications, minimal damage to the target specimen, general reliability, and acceptable level of accuracy [22, 23]. The hole drilling procedure involves drilling a shallow hole in the specimen, which causes a residual stress redistribution and strain relaxation in the surrounding area of the hole. Optical interferometric measurement techniques are applied for capturing the strain relaxation at the top surface. The residual stress profile is obtained from the full-field data of the surface displacement by solving an inverse problem through analytical techniques such as Fourier analysis, regularization, smoothing, etc. [24–26]. However, due to the assumption of linear elastic deformation, the hole drilling measurement is limited to residual stresses of about max. 60–70% of the material yield strength [21, 27].

Over the last three decades, much research has been done regarding the drilling process [22], surface deformation measurements [28, 29], and analytical methods for determining the residual stress profile from the surface displacement data [24, 26]. Low-speed drills have substituted electrical discharge machining and electric endmills, while strain gauges have been replaced by

optical techniques such as electronic speckle pattern interferometry (ESPI) or Moiré interferometry, which are capable of capturing full-field data about surface displacement [28], [29–31]. In the 1980s, G.S. Schajer [32] proposed finite element calculations for relating the “removed stresses” to the measured strain at the surface, replacing experimentally determined calibration constants that had been restricted in terms of specimen shape, materials, and experimental procedure. Later, Schajer [19, 20] developed the Integral method (IM) for the identification of non-uniform residual stresses from strain relaxations, which substituted the previously applied Incremental strain and Average strain methods. Most recently, an advanced numerical approach for calculating stresses from ESPI data has been proposed [26]. The approach allows the reduction of thousands of displacements to a small number of representative values by utilizing a known mathematical relationship within the measured data. Therefore, the Integral method has become computationally very efficient and accurate.

Several studies have addressed the problem of plasticity in connection with the hole drilling method, which arises as soon as the residual stresses approach the material yield strength [27, 33–35]. Plastic deformation is the main source of error in the measured stress profiles, due to the violation of the underlying assumption of material linearity in the Integral method. However, the proposed solutions are time-consuming and, in most cases, not applicable for correcting non-uniform residual stress profiles with high gradients of up to 4000 MPa/mm. Furthermore, these studies [27, 33–35] have only dealt with specific materials, which does not allow the application to a wide range of engineering materials. Therefore, the focus should be on developing practical and elegant ways of residual stress correction, covering the full range of stress levels and the relevant range of material behaviors.

The contour method — a “destructive” residual stress determination technique — is based on similar mechanical principles like the hole drilling. The stresses are determined through measuring the out-of-plane relaxations on the cut surface, while, in case of the hole drilling, the in-plane component constitutes most of the measured relaxation (in projection on the sensitivity vector). Thus, the contour method experiences a similar plasticity effect due to the assumption of material linearity [36]. Recently, a novel approach was introduced for mitigating cutting-induced plasticity by changing the cutting path. The proposed double-embedded cutting configuration significantly improves the stress determination on the weld by eliminating the plastically affected regions in the cut surface from a back-calculation procedure [37, 38]. Such an approach is not applicable to the hole drilling method, because in this case, the cutting path is simply defined by the drill geometry and is normal to the surface. Thus, plasticity effects need to be investigated in detail and — based on this understanding — a stress correction approach needs to be developed.

The present work aims at (i) investigation of the limitations of the hole drilling method related to the effects of plasticity and development of a method for residual stress correction, capable of

covering a wide range of stress levels and material behaviors; (ii) optimization of the LSP in regard to generated residual stresses for the fatigue life improvement of metallic structures.

The three main objectives are defined as follows:

- A method for the correction of high equibiaxial residual stresses measured by hole drilling shall be developed and validated.
- The LSP process shall be investigated in regard to achievable residual stress profiles using design of experiments (DOE), and the prediction accuracy of the established regression model shall be experimentally validated.
- The potential for retardation of the fatigue crack propagation in thin-walled metallic structures through the LSP-induced residual stresses shall be experimentally demonstrated.

The ultimate goal of the current work is defined in the last objective, which addresses the enhancement of fatigue behavior and damage tolerance improvement of thin-walled metallic structures by means of application of the LSP treatment. Fatigue life improvement is of great interest for many different industrial applications; therefore, the present work contributes to the promotion of the surface modification techniques.

1.2 Approach

The objectives defined in the previous chapter can be reached by the following scientific approach, consisting of four steps.

In the first step, the hole drilling process will be represented in ABAQUS by using an axisymmetric Finite Element (FE) model involving plasticity; afterwards, the Integral method will be applied to the relaxation strain data for determining the stress field. The FE model will be validated experimentally on the three-point bending flexural test with AA2024-T3.

In the second step, an artificial neural network will be used to identify the relationship between predefined (“actual”) and simulated stress profiles (plastically affected data obtained through the Integral method) in dependence on the material behavior and the shape of the predefined stress profile. Afterwards, the neural network will be used for solving the inverse problem of stress profile correction for the given “virtually measured” stresses. Finally, stress correction will be demonstrated on LSP-induced stress profiles.

In the next step, the LSP treatment will be performed with different parameters on the AA2024-T3 specimens and generated residual stresses will be measured using hole drilling. Advanced DOE techniques will be used for the optimization of LSP process in regard to residual stress

profiles. Established DOE regression models with and without correction of plasticity affect by ANN methodology will be compared.

In the last step, fatigue crack growth behavior of the C(T)50 specimens treated by the LSP with the parameters achieved in DOE study will be investigated. The significant retardation of the fatigue crack growth due to the generation of compressive residual stress fields through the thickness will be demonstrated. Fatigue life enhancement for different conditions of the laser peening treatment will be shown and compared.

1.3 Structure of the thesis

The four steps of the proposed approach together with the state of the art of the used techniques and concepts as well as conclusions define the structure of the thesis.

In chapter 2 the most known surface modification techniques for fatigue life enhancement are described and compared with the LSP based on available literature. After that, the destructive (relaxation) residual stresses measurement methods are briefly introduced, with the focus on their main advantages and disadvantages. The hole drilling method is introduced and compared with the ring core method. At the end of the chapter the application of LSP-induced residual stresses for improvement of fatigue and fatigue crack growth behavior is described.

Chapter 3 provides the description of the experimental techniques and numerical methods used in the work. The experimental techniques involve the description of AA2024-T3 properties, the HZG (Helmholtz-Zentrum Geesthacht) LSP setup and hole drilling system “Prism.” The experimental techniques also cover the fatigue crack propagation test and three-point bending test. The theoretical background of DOE is provided. The numerical methods describe the integral method, the solution of inverse problem of stress determination from the measured strain data by the hole drilling, as well as the finite element modeling of hole drilling process. The chapter is closed by the theoretical background of artificial neural networks (ANNs).

In chapter 4 the residual stress correction approach of the hole drilling measurements using the ANN is presented. The hole drilling is simulated in ABAQUS using an axisymmetric FE model involving plasticity and, afterwards, the Integral method for determining the equibiaxial stress field is applied to the strain data. The finite element model is validated on the bending stress profiles generated by the three-point bending test. 203 FE simulations are conducted in order to cover wide range of LSP-shaped stress profiles and relevant range of material properties. The neural network is used for identification of the relationship between predefined (“actual”) and simulated stress profiles (plastically affected data obtained from the Integral method). The detailed description of the correction methodology is followed by its application to the measured

residual stresses, which are induced by the laser peening. The results described in the chapter are published in [39, 40].

Chapter 5 deals with the optimization of the LSP process using DOE techniques. The complex relationship between the laser peening parameters and the generated residual stress fields is established by performing 54 LSP treatments with different parameters and subsequent stress measurement by hole drilling. The feasible region of LSP process parameter variations for achieving defined stress profiles is shown and analyzed. Afterwards, the correction of measured residual stresses from DOE study through the established ANN methodology is performed. DOE regression models — both before and after correction — are compared. Finally, the fatigue crack growth behavior of the LSP-treated C(T)50 specimens is investigated experimentally. Significant retardation of the fatigue crack propagation and, therefore, extension of fatigue life due to the presence of deep compressive residual stresses are demonstrated.

Chapter 6 provides the concluding remarks regarding the novelty of the scientific results achieved in the study.

2. State of the art

2.1 Residual stresses

Residual stresses are the stresses that exist in the material when no external loading is applied [4, 41]. The resultant force and moment caused by the residual stresses always vanish, which means that the tensile stresses are balanced by the compressive stresses over the given material volume. Depending on the size of the area over which the residual stresses equilibrate, they can be distinguished as macroscopic or microscopic [42]. Residual stresses on the microscopic scale are often observed near the dislocations and between the grains in metals [4]. On the other hand, macroscopic residual stresses are generated on various scales in well-known applications such as shot peening [43], LSP, laser heating, etc., but also in areas close to martensitic structures in steel due to the martensitic transformations at low temperatures, which lead to the volume change [4]. The current work is concerned with the macroscopic residual stresses.

Residual stresses can be induced, for example, during the manufacturing process:

1. Non-uniform plastic deformations: rolling, casting, forging, etc. [44, 45];
2. Fabrication, such as welding, shot peening, laser heating [43, 46];
3. Shearing, bending, machining, grinding, and forming and shaping of metal structures [4].

Stress-relieving heat treatments mitigate residual stresses, while quenching generates stresses. Residual stresses are separated into two groups in accordance to the generation mechanisms: a) structural mismatching, b) uneven distribution of non-elastic strains, including plastic and thermal strains [46].

Non-elastic strains are generated, for example, by heating the material unevenly, which leads to its non-uniform expansion and, therefore, causing non-uniform plastic deformation. Another example is the LSP, in which the plastic strains are induced by the high-pressure shock waves propagating in the material.

2.2 Residual stress modification techniques

Airspace industry requires practical and effective approaches for maintaining and increasing the fatigue life of highly stressed metallic structures [47]. The most promising cost-effective solutions are provided by surface modification techniques. As a result, the operating life and damage tolerance are significantly enhanced by the generation of compressive residual stresses in the critical parts of the metallic structures [1, 48, 49]. Generally, all material treatment processes follow the same principle: induced compressive residual stresses highly suppress the crack propagation and prevent the crack initiation, which leads to the extension of fatigue life

[49]. The most well-known modification techniques that are widely used in aircraft applications are cold expansion, shot peening, deep rolling, heating, and LSP. The processes are briefly described in this chapter in regard to their working principle and the generated residual stress profiles [47].

2.2.1 Cold expansion

Since holes in metallic structures — e.g. from the insertion of rivets — are the sources of stress concentration that can lead to crack initiation and subsequent propagation, cold expansion has become the most commonly used method for the suppression of crack growth in such cases. For the last 40 years, the cold expansion has demonstrated significant fatigue life extension, even in the structures with existing small cracks [50, 51]. The split-sleeve cold expansion process is depicted in Figure 2.1a). The compressive residual stresses in the area around the hole are induced when the tapered mandrel of the larger diameter is drawn through a hole, widening the opening through the plastic deformation [48]. The compressive residual stress distribution in the area surrounding the hole, as shown in Figure 2.1b), is acting against the superimposed cyclic mechanical load, thereby mitigating the stress concentration [48]. However, induced compressive stresses can undergo relaxation when the treated structure experiences high temperature due to maintenance, operational, or accidental factors. The residual stress relaxation influences the static strength and fatigue life of the structures [52].

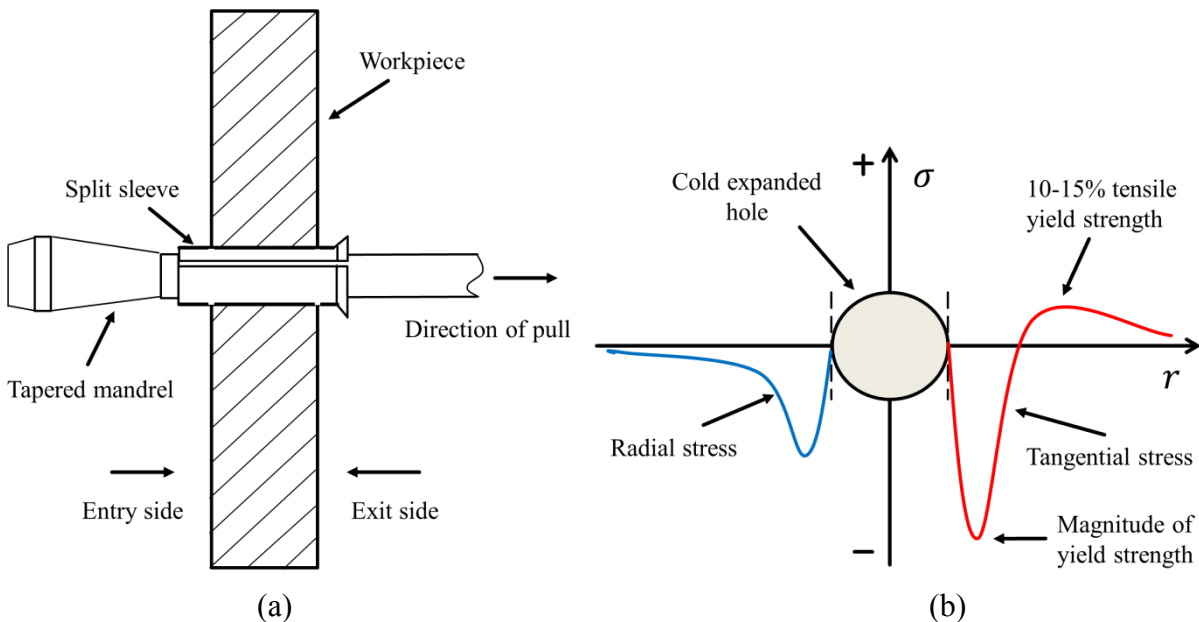


Figure 2.1 a) Split-sleeve cold expansion process, b) residual stresses generated via cold expansion. Depicted and adopted according to [48, 50].

2.2.2 Shot peening

Shot peening has gained a high degree of interest in aircraft applications, where the fatigue performance is of great importance [1]. In principle, the spherical particles bombard the surface of the metallic structure, thereby causing plastic deformation in the thin layer. As a result, the subsurface compressive residual stresses are induced within the depths of 0.2–0.3 mm in the workpiece, which are compensated by the tensile stresses presented deeper in the core [53]. The shot peening process and the resultant residual stresses are presented in Figure 2.2a) and b), respectively. In case of high peening intensities and soft materials, the surface roughness is increased significantly due to the presence of small dimples.

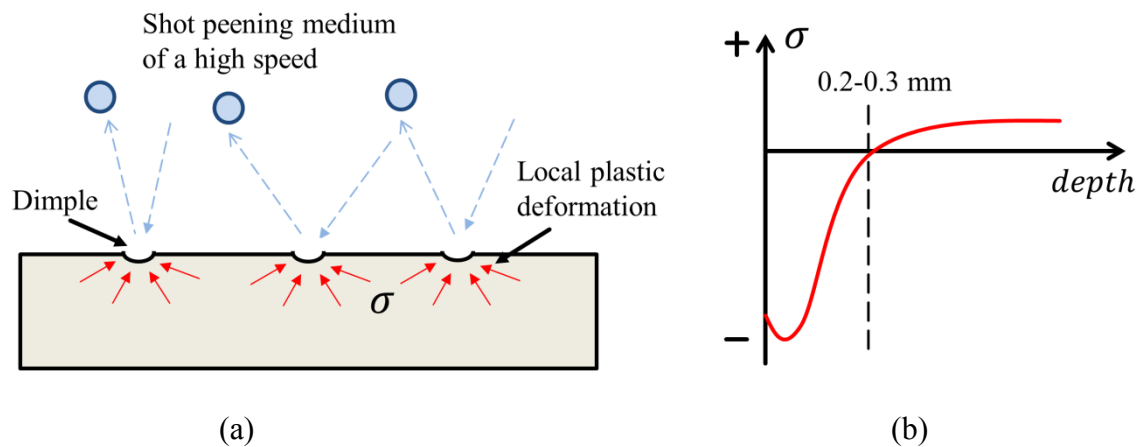


Figure 2.2 a) Shot peening process, b) residual stresses generated via shot peening. Depicted and adopted according to [1, 53].

The typical units of the metallic structures to which the shot peening is applied are gears, turbines, blades, welded joints, springs, and grooved shafts. Furthermore, shot peening is used for the enhancement of the resistance to corrosion fatigue and stress corrosion cracking [49]. Because of the low depth range of compressive residual stresses in the workpiece, shot peening is effectively used for fatigue life extension in metallic structures where the cracks are initiated at the surface, such as airframes and jet engine parts; it demonstrates almost no improvement when cracks through the thickness are present [1, 12, 53, 54]. Often, the shot peening process is compounded with the pre- or post-heat treatment, which has a synergetic effect on the fatigue life.

2.2.3 Low-plasticity burnishing and deep-rolling

Low-plasticity burnishing is the surface enhancement process widely used for fatigue life extension and stress corrosion cracking improvement, which is based on the principle of cold work hardening [55]. The low-plasticity burnishing is schematically illustrated in Figure 2.3. A single pass connected to a smooth free-rolling ball normally loads the workpiece surface. The

ball rolls on the burnishing surface, causing plastic deformation in the subsurface layer. A spherical fluid hydrostatic tool supports the burnishing ball. It provides constant cooling during the operation, which significantly increases the ball life and prevents surface damage. The low-plasticity burnishing is automatized by robots and can be applied on aircrafts for repair, maintenance, and manufacturing procedures. However, complex geometries cannot be treated because of the dimensional restrictions of a system.

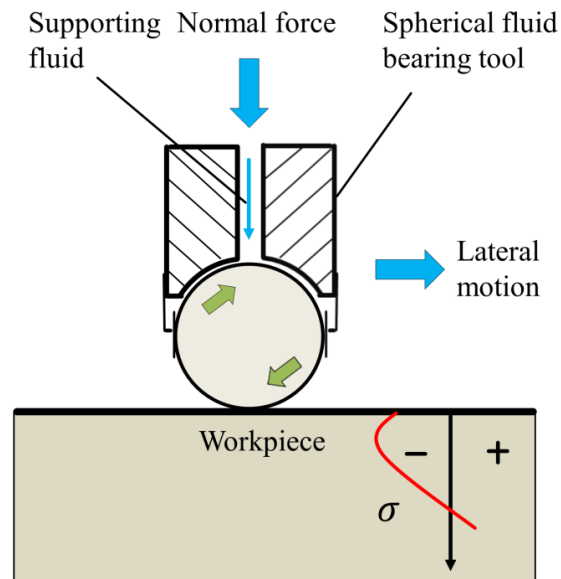


Figure 2.3 Low-plasticity burnishing process. Depicted and adopted according to [47].

The deep-rolling technique has many similarities to low-plasticity burnishing. Either a ball or roller tools have a mechanical contact at the point of the treated surface, which creates high 3D Hertzian compressive stresses distribution [56]. In contrast to low-plasticity burnishing, a finer surface finish and component sizing are achieved after several repeated deformation cycles. A common shortcoming of both methods is the compressive residual stress relaxation when the treated material experiences elevated temperature exposure or mechanical overload.

Low-plasticity burnishing and deep rolling significantly improve the damage tolerance, stress corrosion cracking, and fatigue behavior of highly loaded metallic structures through the generation of compressive stresses at the depth, ranging up to 12 mm and deep work-hardening layer; however, at the same time, they retain the smooth surface finish [57]. The surface enhancement is used in propellers, landing gears, medical implants, and nuclear components. The fatigue life of these components is improved by Factors 4–6 even if small cracks already exist.

2.2.4 Laser heating

The residual stresses induced by heating are normally considered as a side effect of the fabrication or maintenance process and have to be avoided. However, laser heating has recently received a great deal of attention as a surface enhancement technique that deliberately generates compressive residual stresses for the suppression of fatigue crack propagation in aircraft-grade aluminum alloy specimens [58–60]. The laser heating process and the generated residual stress distribution are shown in Figure 2.4a) and b), respectively. The defocused laser running parallel to the workpiece surface creates the heating line. The material subjected to heating tends to expand, but the surrounding material constrains it. Therefore, in the heated material, compressive stresses occur, which are compensated by the tensile stresses in the surrounding area. The material yield strength decreases with increasing temperature, but the compressive stresses grow. When the yield strength is exceeded, plastic deformation starts to occur, causing a formation of residual stresses. After the cooling of the workpiece to room temperature, high-tensile residual stresses in the longitudinal direction are present in the heated area; they are in equilibrium with the compressive residual stresses occurring around the treated material.

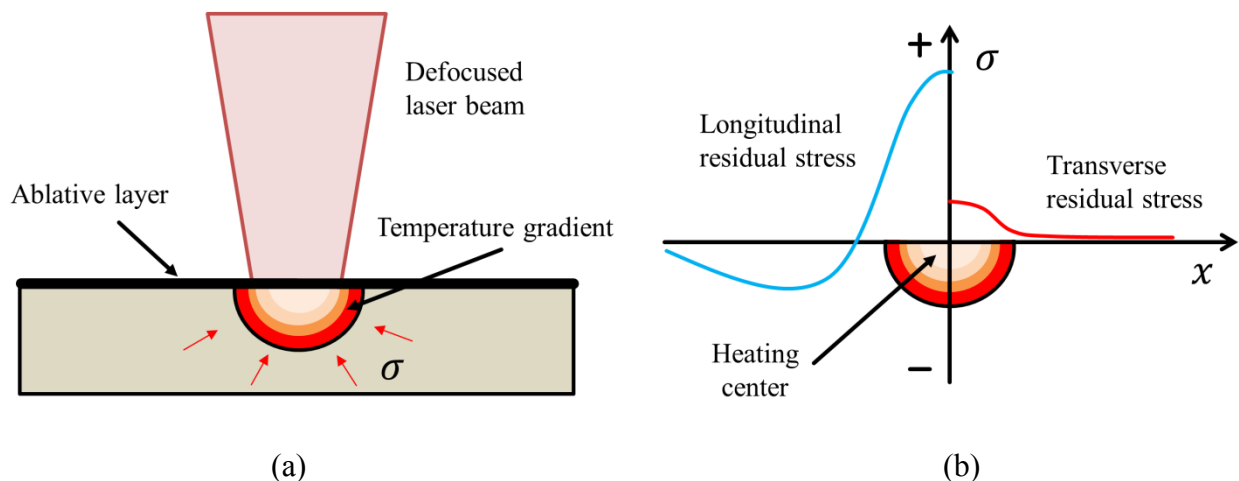


Figure 2.4 a) Laser heating process, b) Residual stresses generated via laser heating. Depicted and adopted according to [58–60].

The drawback of laser heating is the reduction of material hardness in the treated area, which affects the static strength of the lightweight structures [58]. Moreover, the application of multiple layers when treating the large panels causes a tempered microstructure [61].

2.2.5 Laser shock peening

LSP is a surface modification technique that is increasingly used for the improvement of material properties and microstructure modification. LSP induces compressive residual stresses deep into the material, which significantly increases fatigue life, especially in cases where damage is caused by the crack initiated at the surface [1, 62]. In comparison to conventional techniques,

LSP has many advantages [3], such as flexibility in processing different geometries and capability of use in existing production lines, low surface roughness, controllable laser pulse beam with the possibility to strengthen the material at the corners, and a clean process with no need for material recycling in comparison to shot peening.

The LSP process and the induced residual stress distribution are shown in Figure 2.5a) and b), respectively. The laser with high-pulse energy is used for treatment of the material surface, which is usually covered by a water-protecting layer. Having passed through water, the laser beam is absorbed by the material, which turns into plasma. Consequently, the plasma expands very rapidly by absorbing the laser energy during the pulse. The transparent water layer traps the plasma, causing a high pressure at the material surface. The energy of the high-pressure plasma partially turns into shock waves, which propagate into the material. Plastic material deformations occur when the shock wave pressure exceeds the dynamic yield strength, which in turn leads to compressive residual stresses in the treated area and tensile stresses in the surrounding area [3, 63]. LSP treatment increases the material hardness in the peened area, similar to cold working mechanisms.

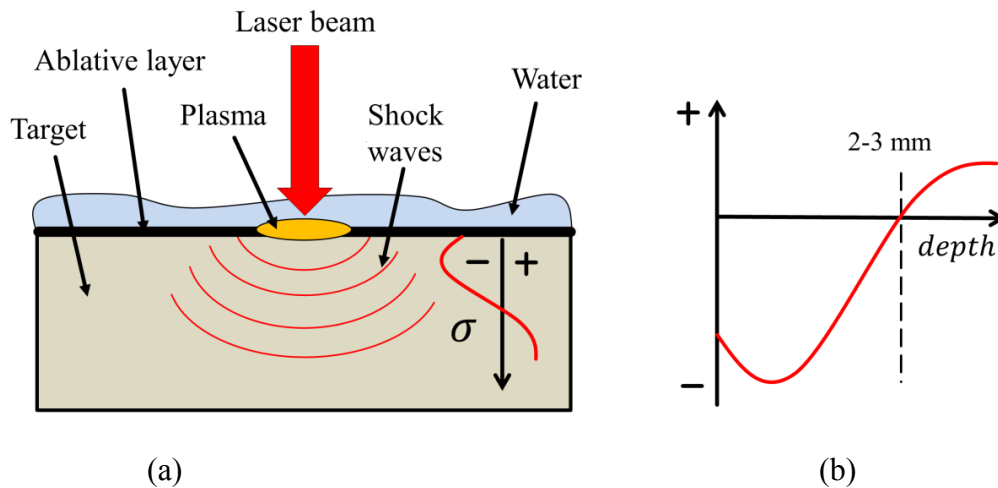


Figure 2.5 a) Residual stresses generated via LSP, b) LSP process. Depicted and adopted according to [1, 3].

Compressive residual stresses generated by the LSP are of a higher magnitude and up to 10 times deeper than stresses obtained through shot peening [64]. The induced residual stresses demonstrate no relaxation during and after treatment because the material remains cold during the process. However, LSP equipment is more expensive and also requires operator protection and particular operator knowledge.

At present, LSP is a well-established process for improving resistance to corrosion [65], reducing fretting fatigue damage [3], and increasing resistance to foreign object damage [18]. Numerous possible applications of these technologies to metallic aircraft structures include fatigue-critical

components such as wing attachment fittings, landing gear (including wheels and brakes), fasteners and fastener holes, welded aircraft parts, helicopter components, springs, turbine vanes, and blade bases [66–69]. Nowadays, compressive stresses are successfully used in the retardation or even complete suppression of fatigue crack formation and deceleration of the crack propagation, thereby enhancing the fatigue life and improving the damage tolerance of lightweight metallic structures [62, 66].

LSP without coating has gained a lot of interest in industrial applications, because it reduces the treatment cost and operation time while keeping the material surface damages minimum. Another innovative treatment modification, the so-called warm LSP, involves the dynamic aging of the material for the improvement of fatigue performance. Such treatment enhances surface strength, reduces surface roughness and causes higher stability of the dislocation arrangement in comparison to conventional LSP. Furthermore, the compressive residual stresses are deeper by a factor of 1.5. Such stress extension leads to a higher suppression of the crack propagation and, therefore, greatly enhances the fatigue behavior, especially in the high-cycle region.

2.2.6 Comparison of laser shock peening and the established processes

Laser heating induces high tensile stresses in the heated zone, which leads to the occurrence of the balancing compressive stresses of a lower magnitude in the large surrounding area. Considering the cold expansion, the compressive radial and tangential stress components generated in the vicinity of the treated hole is uniform throughout the thickness of the workpiece and is in equilibrium with the tensile stresses in the surrounding area. Shot peening is similar to the LSP in regard to the nature of the process, but the depth of compressive residual stress does not exceed 0.3 mm. Low-plasticity burnishing induces compressive residual stresses up to a depth of 12 mm while maintaining the surface roughness, but the treatment cannot be applied to the complex geometries and has a relatively high cost. Regarding the final residual stress state, LSP is the most promising surface modification approach, because it generates a compressive stress gradient within a depth range of 2–3 mm, with magnitudes comparable to the material yield strength.

Regarding the application geometry, the low-plasticity burnishing process is restricted to holes and flat surfaces, while other modification techniques can be applied to relatively arbitrary structures.

Low-plasticity burnishing, cold expansion, and shot peening have been successfully used for the last 40 years in industrial applications involving manufacturing, maintenance, and repair procedures. Laser heating and LSP are relatively new surface modification techniques, which have been recently established in industry but have already demonstrated significant improvement in the fatigue behavior of metallic structures. However, these techniques have not

been fully investigated yet due to the complexity of the processes encountered during the treatment procedures. Therefore, obey potential can be expected as a result of the ongoing research.

Comparing all surface modification techniques, LSP is seen the most promising approach for damage tolerance improvement and fatigue life extension due to its unique ability to generate compressive residual stresses throughout the thickness, e.g. aircraft thin and profile materials, while keeping surface damages to a minimum. LSP meets most of the objectives of industrial applications, where the possibility of application to the complex geometries and low operational cost are of primary importance. The various surface modification techniques are summarized in Table 2.1 for a quick comparison.

Table 2.1 Comparison of the processes reviewed in this study.

Process	Material and source	Plastic-affected distance (mm)	Compressive peak (MPa)	Fatigue life improvement
Cold expansion	AALY12-CZ [51]	2.5–3 from hole edge	~ -300	6 times
	AA2024-T351 [70]	1–2 times the hole radius from the hole edge	~ -300	2.2 to 3.8 times, major through SCG in SCS
	Titanium alloy TC4 [71]	1.1–1.8 from the hole edge	~ -400	1.5–3 times, minor CPR in low stress and SCS
Shot peening	Magnesium alloy GW103 [72]	~ 0.2 in depth	~ -80	HCF strengths improvement of ~ 40%
	St52 (S355) steel [73]	~ 0.2 in depth	-100 to -200	~ 75%
	AA7075 [74]	~ 0.2 in depth	-300 to -400	14 times
LSP	Magnesium alloy ZK60, 2 mm thick [75]	0.5–1 in depth	-160 to -200	From 72.9 to 78.5%

Note. Plastic affected distance = distance at which residual stress changes from compressive to tensile; SCG = slow crack growth; SCS = short crack stage; CPR = crack propagation rate; HCF = high cycle fatigue; FFR = fretting fatigue resistance; HZ = heating zone. According to [47].

Table 2.1 Comparison of the processes reviewed in this study.

Process	Material and source	Plastic-affected distance (mm)	Compressive peak (MPa)	Fatigue life improvement
LSP	AA6061-T6, 2 mm thick [76]	0.6 in depth	-210	7.3%–99.4%
	AA6061-T6, 3 mm thick [77]	1 in depth	-250 to -300	25% in HCF strengths
	AA2024-T351, 2 mm thick [78]	~ 1 mm in depth	~ -350	3.5 times
	Ti-6Al-4V, 34.3 mm thick [79]	~ 6 in depth	~ -400	-
Deep rolling/low-plasticity burnishing	AA2024-T851, 2.5 mm thick [57]	12–25 from the edge	-160 to -200	6 times; full restoration in pre-cracked
	AA7075-T6, 4.5 mm thick [80]	~1 in depth	~ -500	700% of FFR for HCF
	Ti-6Al-4V [81]	0.3–0.4 in depth	-400 to -800	-
	Ti-6Al-4Y [82]	0.6 in depth	~ -1000	-
Heating	AA2198-T8, 5 mm thick [58]	6 from the middle HZ	-160 to -200	300%
	304SS, 4.6 mm thick [83]	~10 from the middle HZ, 0.6 in depth at the middle HZ	-200	increase of fatigue crack resistance; decrease of CPR
	SS400, 15 mm thick [84]	12 from the notch	-300 to -350	8 times FCP or crack arrest

Note. Plastic affected distance = distance at which residual stress changes from compressive to tensile; SCG = slow crack growth; SCS = short crack stage; CPR = crack propagation rate; HCF = high cycle fatigue; FFR = fretting fatigue resistance; HZ = heating zone; FCP = fatigue crack propagation. According to [47].

2.2.7 Challenges of LSP process optimization

Over the last three decades, a great deal of research has been accomplished regarding the LSP optimization [85–87]. The generation of desired residual stress fields by controlling the laser

parameters has always been a main focus of scientific work. The LSP process can be described in four stages: (i) delivery of the laser beam with the certain energy; (ii) plasma generation on the surface of the material under the confining medium; (iii) propagation of the high-pressure waves in the material; (iv) generation of the residual stresses. Regarding the first stage, the current market offers different pulsed laser systems with a pulse duration of nanoseconds and energy of 10 joules, which meet the LSP objectives.

As for the second stage, the measurement of plasma parameters is very challenging due to the extremely short process duration (nanoseconds) and high energies [3, 88]. Spectroscopic techniques for the determination of plasma temperature and density cannot be used because the water layer is not transparent for the emitted radiation [3].

At the next stage, the shock waves propagating in the material also have a duration in the order of nanoseconds; and they attenuate during the propagation. The “locked-in” nature of these shock waves of a high pressure makes them very challenging to measure. There are no measurement techniques that would determine the precise shock waves movement over the time. What follows is that the generation of residual stresses cannot be accurately predicted without information about the original cause.

Because of the measurement difficulties described above, the focus of research has shifted into the direction of modeling. Many studies in this field have been accomplished with the aim of creating an FEM model for the simulation of shock waves propagation and the generation of resulting residual stresses [89, 90]. In some works, the boundary conditions of the FEM model are obtained by the measuring the surface waves or rigid specimen movement due to the plasma explosion [91]. In these cases, the validation of FE simulation is provided by the comparison of the resultant simulated and LSP-induced residual stress profiles.

Development of the FEM model has greatly advanced the LSP technique. However, a high computational cost of the precise simulation and uncertainties in measurement techniques restrict the model accuracy. In that case, only a qualitative assessment of the induced residual stresses is provided by the LSP companies.

In the light of described challenges, researches have utilized statistical DOE techniques for LSP optimization [92–96]. The main advantage of DOE is that it does not require a knowledge about the plasma generation and shock-wave propagation, i.e. the intermediate stages of the LSP are considered as a “black box,” represented by the experiments in which LSP process parameters and resultant residual stresses and material properties are handled. Trdan et al. investigated the influence of laser pulse density on the surface roughness, subsurface residual stress in depth of 0.03 mm, microhardness and corrosion resistance of two alloys AlMgSiPb and AlSiMgMg with different rolling directions [96]. The DOE revealed strong relationship between the laser pulse

density and the intensity of pitting corrosion attack as well as the subsurface stress. The optimum laser energy was achieved for enhancement of surface modification process in terms of surface roughness, corrosion resistance and microhardness of the treated material.

Most recently, Ebrahimi et al investigated the effects of the laser intensity and overlapping amount of shot spacing on corrosion and hardness properties of ANSI 316 stainless steel [94]. DOE was utilized to learn these effects and to predict the data for unallowable inputs combinations due to the facility limitations. The results relieve that both corrosion resistance and surface hardness are improved by maximum of 100% and 35%, respectively, by increasing of the laser spot size and laser intensity. With the help of DOE it was found that hardness is more strongly related to the laser intensity while the corrosion resistance is mostly depended on the amount of shot overlapping.

Cellard et al undertook an investigation of the influence of laser shock peening parameters on the material parameters of titanium alloy Ti-5Al-2Sn-2Zr-4Cr-4Mo (Ti-17) [92]. The specimen thickness, laser pulse energy and duration, number of impacts were controlled variables while the measured variables were the residual stress averaged at 4 μ m under the surface, Vickers microhardness, the specimen curvature and the width of the diffraction peaks. The achieved results demonstrate that all parameters influence the sample curvature, while the integral width is only affected by the pulse duration. The roughness of titanium alloy is maintained constant in all experiments. The thickness affects the residual stress profile — the tensile stresses occurred at the surface of specimens with the thickness of 5mm, but in case of 45 mm thickness the compressive stresses were found at the surface. DOE analysis revealed interaction effects of thickness/pulse density and pulse duration/pulse density on microhardness that is not possible to determine by running of one-factor-at-a-time experiments.

The effect of high repetition LSP, working at 10 KHz and 3.52 W, on magnesium based biodegradable alloys was recently investigated by Kamkarrad et al. with the help of DOE techniques [95]. In this work the laser intensity, number of shots and percentage of overlap were considered as controllable parameters and the maximum peening depth, surface roughness and microhardness were considered as measured parameters. DOE analysis provided the threshold values of controllable LSP parameters, which refer to 2 GW/cm², leading to the significant increase in surface roughness and microhardness. It is also found out that, at this intensity value, no trace of machining or solidified material appears.

In the present work, DOE analysis is employed for the LSP process optimization in regard to generated residual stress profiles over the depth of AA2024 specimens; because the fatigue and fatigue crack propagation behavior is strongly affected by the shape of the stress profile. For this purpose, the experiments at the specific levels of laser parameters are conducted and the resultant residual stress profiles are measured. The design of experiment is applied to determine the

complex relationship between LSP parameters and the generated stress profiles from a limited number of runs corresponding to all combinations of treatment parameters.

2.3 Residual stress measurement techniques

2.3.1 Challenges of measuring residual stresses

Generally, the measurement of stresses caused by the external loads follows an indirect manner: the resulting strain or displacement is determined, after which the existing stress is calculated from the collected data based on elasticity theory. To this end, the measurements are conducted on the structure with — and then without — external load and subsequently, the stresses are determined based on the measured difference. But in case of the residual stresses that exist without the external loads, the measuring procedure becomes more challenging due to the “locked-in” nature [4]. Removal and subsequent application of the residual stresses are technically very difficult to implement. Therefore, the measurement approach of all relaxation methods often applied involves cutting away the piece of material where residual stresses are to be determined and measuring the resulting displacement of the adjacent remaining material. This separation of measurement location and stress location originates in the main computational challenge. This problem is solved by employing specialized stress evaluation methods [97, 98]. Other methods for stress determination—the so-called non-destructive measurement techniques such as synchrotron or X-ray — do not cause material damages, but they require the reference stress-free state for the evaluation of collected data. Practically, it can be quite challenging to reliably achieve the reference measurements [4]. These challenges lead to lower accuracy and reliability of the measured residual stresses in comparison with measured applied stresses.

2.3.2 Relaxation measurement methods

The removal of material leads to a residual stress redistribution, which in turn causes structural deformations. These deformations — often called “relaxation” — have an elastic manner, meaning that a linear relationship exists between the amount of deformation and the released residual stresses [45, 99, 100]. This statement represents the main idea of all “destructive” stress measurement methods, which try to determine residual stresses from the measured material deformations. Almost all methods require finite element calibration, due to the characteristic that the measurement takes place in the regions containing only partial stress of interest. The size and geometry of the measurement equipment vary among the destructive techniques, but they all measure surface relaxation, resulting from the cutting of the stressed material.

2.3.2.1 Slitting method

The slitting method measures the in-plane residual stress component, which acts normal to the planar slit, over the workpiece thickness [101, 102]. The residual stresses are determined in the practical laboratory very quickly and with high reliability. The slitting procedure is shown in

Figure 2.6. The stressed material is incrementally cut away using a wire electric discharge machine. A planar slit causes residual stress redistribution, leading to a surface deformation in the area around the slit. This deformation is measured by the strain gages after each depth increment and is then used for the calculation of residual stresses normal to the slit surface originally existing in the material. In case of relatively thin specimens, as shown in Figure 2.6, the strain is measured on the front and back surfaces. The applicability of the slitting method covers metals, glass, crystal, as well as different structure varieties such as plates, tubes, rings, rods, beams, and blocks. The computation of the residual stresses from the strain gage data is performed using a linear system expressed as “relaxation matrix,” which is built using finite element modelling. The stress determination — as a solution to an inverse problem — is achieved by the series expansion for the residual stress. The best set of unknown coefficients of the polynomial series provides the residual stresses over the depth based on the measured strains. Tikhonov regularization provides the robust stress calculation in cases where the collected data includes measurement noise, making the stress profile smooth over the depth.

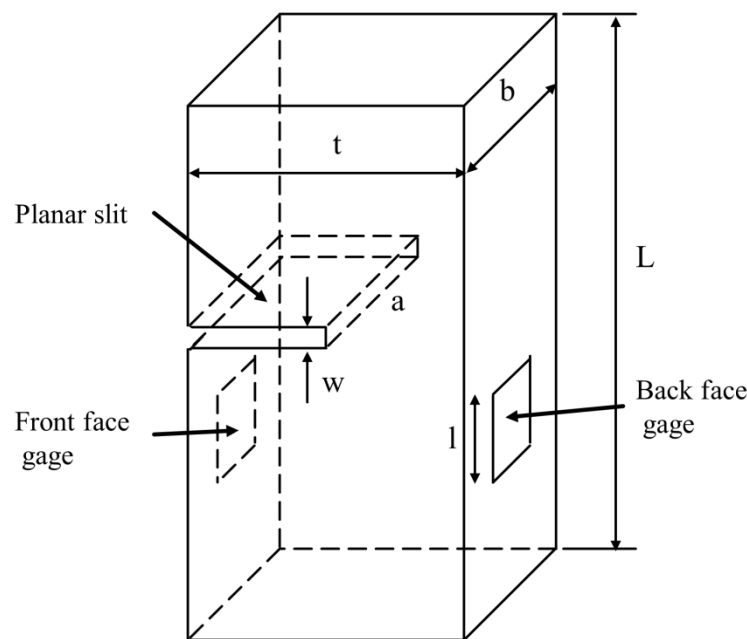


Figure 2.6 Slitting process: t , b , L are workpiece thickness, depth and length, respectively; a and w are slit depth and width, respectively; l is the strain gage length. Depicted and adopted according to [4].

2.3.2.2 Contour method

The contour method is a residual stress determination technique that involves cutting a workpiece into two parts and measuring the deformation of the cut surface [103, 104]. The measured deformation, caused by the stress redistribution, is used for calculating the originally existing residual stresses. The stress calculation procedure involves finite element analysis and

the analytical application of Bueckner’s superposition principle. In the FE model, the displacement boundary conditions are defined by the measured displacement. The contour method determines the longitudinal stress component which acts normally to the cut surface. The most attractive feature of the contour method is the ability to measure the two-dimensional stress map over the cut surface, which is very useful for non-uniform residual stresses that are spatially distributed in the material. Therefore, the contour method is widely used in different industrial applications such as laser welding, laser peening, shot peening, etc. Since the finite element analysis accounts for the complex specimen geometry, the shape of the part is not restricted.

The superposition principle of the contour method for single and double cuts is presented in Figure 2.7 [105, 106]. Step **A** shows a specimen with the residual stress profile that has to be measured. Subsequently, in Step **B**, the specimen is cut into two pieces on the flat $x = 0$, which leads to elastic deformation due to residual stress redistribution. The stresses are relieved on the cutting surface. Step **C** demonstrates the virtual application of the external stress field $F^C(y)$, which brings the surface to the original state as it existed before cutting. The composition of stress states **B** and **C** uniquely determines the original residual stress distribution on the plane of the cut $x = 0$ in Step **A**.

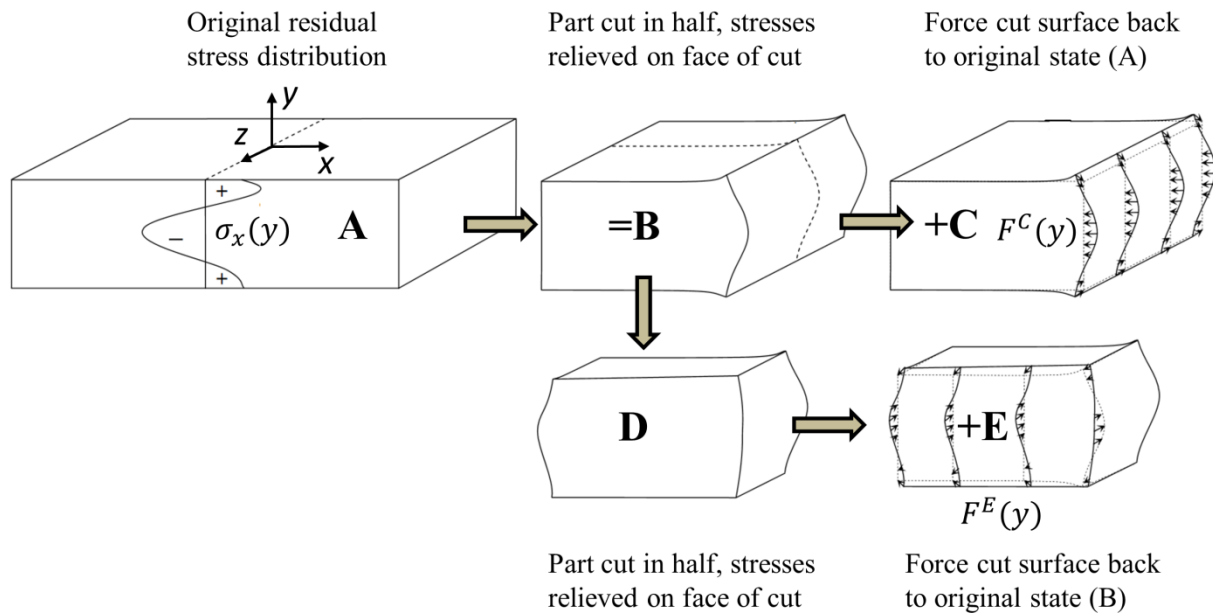


Figure 2.7 Superposition principle for the contour method. (**A–C**) single cut plane defines $x = 0$; (**D–E**) double cut plane defines $z = 0$. According to [106].

According to the superposition principle, the residual stress acting normally to the cut surface can be determined experimentally. In Step **B**, the contour surface deformation — the so-called surface height map — is measured after relieving residual stresses. The surface height map contains only the displacement data normal to the surface. Therefore, the virtual analytical

approximation (Step C) forces the surface back to its initial stage, which causes the transverse displacement component to be unconstrained. For this reason, the contour method is not able to determine shear stresses on the free surface. The contours measured on two halves of the part are averaged in order to minimize the measurement error.

Analogous to the single cut, the second cut of the plate is presented in Steps D and E. This relatively new approach allows the determination of the residual stress field in z direction. It should be noted that the stress redistribution in the first step is assumed to not affect the stress redistribution in the second step.

The contour method assumes linear elastic material behavior; therefore, when the residual stresses approach the material yield strength, plastic deformation occurs, leading to an error. This plasticity effect is very difficult to simulate, because it requires not only definition of the incremental cut but also precise modeling of the reverse yielding behavior of the material, which would cover different stress distributions. The approach for the correction of plasticity effect was introduced very recently; it involves controlling the contour cutting configuration [37, 38].

The evaluation of the plasticity effect is often deceptive, because it is difficult to compare residual stress with the material yield strength. Additional material hardening or softening — induced by the manufacturing or repair processes — change the yield strength. Moreover, a von Mises effective stress, which must be compared to the yield strength, may be much lower than the measured single stress component. All stress components of the multiaxial stress state should be taken into account to determine the correct equivalent stress. In addition, the integrated effect of the whole relaxed stress profile influences the cut tip yielding.

2.3.2.3 Hole drilling and ring core methods.

Hole drilling [107] is the most famous semi-destructive technique for residual stress determination in thin metallic structures [108, 109]. The method has attracted a lot of attention in different industrial applications due to its high reliability, relatively low cost, high accuracy, and — at the same time — tolerable damage to the workpiece. After drilling a blind hole in the place where residual stress is to be measured, the material surrounding the hole immediately returns to the new stress equilibrium, leading to surface relaxation around the hole. The surface displacements are captured by the strain gage or optical techniques and are then used for determining the originally existing residual stresses.

The ring core method is similar to the hole drilling, but the surface deformations are measured inside the slotted annular groove [110, 111]. Both methods, as illustrated in Figure 2.8a) and b), determine the residual stress fields from the measured strain data by solving an inverse problem. However, due to the different geometries of the methods, the FE relaxation matrices are not identical. Hole drilling is easy to implement with the minimal specimen damage. In contrast, the

ring core can measure the high residual stresses approaching the material yield strength because of the larger relieved strains. Furthermore, the ring core method allows measurement of stresses at greater depths [4].

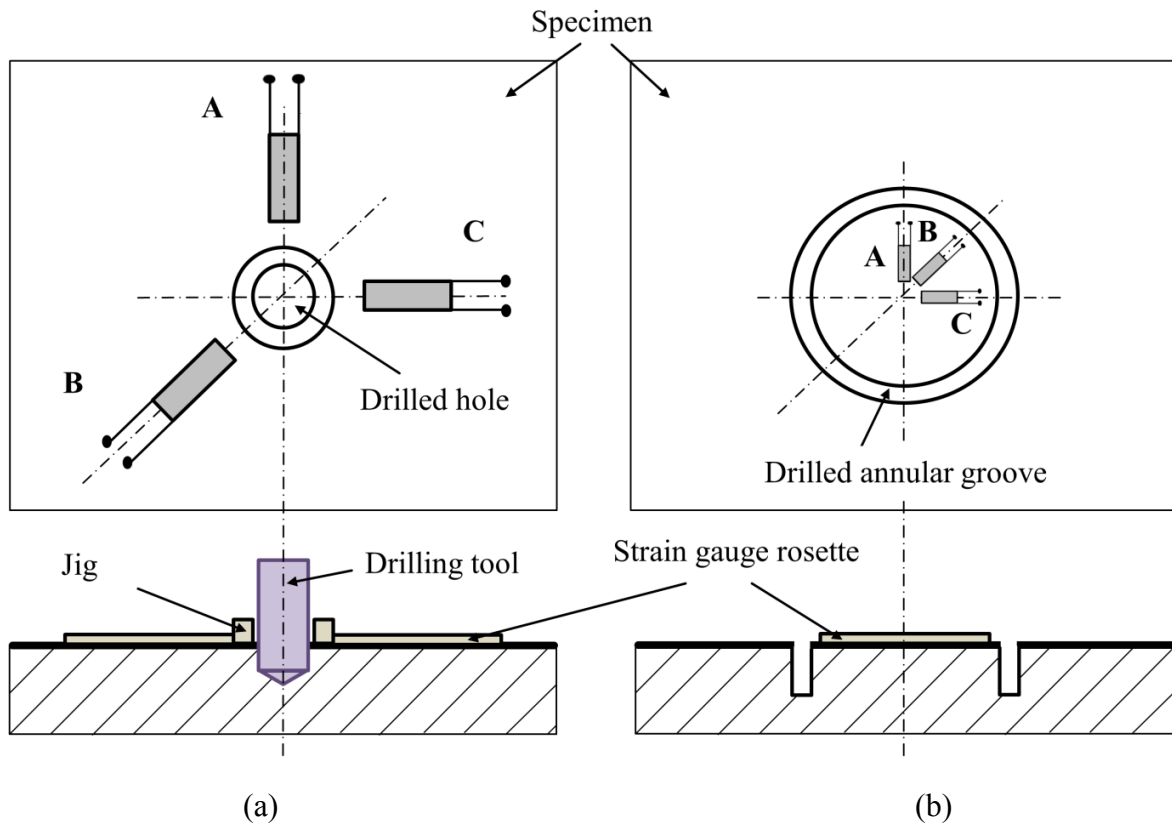


Figure 2.8 Semi-destructive methods: a) hole drilling; b) the ring core method. Depicted and adopted according to [112].

Deep hole drilling has inherited some mechanical features from the hole drilling and ring core methods [101, 102]. It determines the residual stresses, which are much deeper in the thick specimen, by drilling a deep hole and then measuring the diameter variation caused by the residual stress redistribution. The method has a high sensitivity to the stresses in the deep interior, while the conventional hole drilling and ring core methods are aimed at the identifying subsurface stresses.

As shown in Figure 2.8, the strain gauges are traditionally used for the measurement of the surface relaxation. Over the last four decades, strain gauges have demonstrated high robustness and reliability [113]. The rosette connects the strain gauges and keeps the space orientation between them identical, which significantly mitigates alignment error and enhances the measured data quality. The modern strain gauges are equipped with an electronic instrumentation, which allows the capture of very low strains, typically occurring during the drilling of the hole or ring core. The standardizing rosette geometry of the hole drilling is well-established in regard to the

calibration constants that reflect the relationship between the measured strains and residual stresses.

For the last 20 years, optical techniques have been successfully used for the measurement of surface relaxations [28]. The optical techniques capture the full-field displacement data from the specimen surface, while the strain gages measure only the strain in three discrete directions. This main feature of the camera-based techniques supports data averaging and error checking. Moire Interferometry, ESPI, and Digital Image Correlation are the most well-known optical measurement techniques, which have similar working principle; the diffraction patterns, imaged by a video camera, are used for determination of the surface displacements [29, 30]. The ability to provide full-field data leads to an improvement in the accuracy and reliability by averaging the data, and helps to detect the errors and outliers. However, the optic systems are not always portable and require certain working conditions, while the strain gages are mobile and are used in different industrial fields. Also, the optical equipment has a high cost but a moderate per-measurement cost; in contrast, the cost of strain gages is much lower, but every measurement requires more effort and time.

Assumptions and limitations of the ring core method [4, 112] are:

- Out-of-plane residual stress is neglected.
- Material is linear elastic and homogeneous.
- The specimen surface is flat.
- There is no plastic deformation due to the milling process.
- The core is perpendicular and cylindrical relative to the flat material surface.
- The thickness of the specimen allows the generation of a blind groove.
- The ring groove is sufficiently far from other geometrical features.

Assumptions and limitations of the hole drilling method [4, 112] are:

- The material elastic properties are homogeneous and isotropic.
- The material relaxation is linear elastic.
- The specimen is significantly thick — the hole diameter is smaller than the thickness, at least by a factor of 2.
- The hole diameter is at least two times bigger than the hole depth.
- The drilling procedure does not cause essential plastic deformation.
- The residual stresses are uniformly distributed in the plane of the material surface.
- The specimen surface is flat.
- The distance between the neighboring holes is at least three hole diameters.

The drilled hole produces a stress concentration in the material. When residual stresses approach the yield strength, the local plastic flow occurs near the hole boundary, which causes significant deviation from the material linearity [27]. The Integral method used for the realization of the inverse problem is based on the behavior of the elastic material. Therefore, the measurement error of residual stresses arises as soon as local plastic deformation occurs. On the other hand, the ring core geometry does not generate high stress concentrations in the material body and also causes a higher strain relief; thus, the ring core method is able to measure residual stresses up to the material yield strength.

2.4 Fatigue life extension via the residual stresses generated by the LSP

The fatigue life of the structure is defined by the number of stress cycles until the failure. This number depends on the stress level and state, fatigue environment, cyclic wave form, and the material. The fatigue behavior of the structures is investigated by conducting laboratory tests at different scales. The laboratory fatigue tests are divided into crack initiation and crack propagation tests [114]. The crack initiation test — also called high-cycle fatigue, involves application of the cycle loading to the specimen until the crack nucleation and subsequent crack propagation until the failure of the specimen. On the other hand, in the crack propagation test, the cycle loading is applied to the specimen with preexisting cracks, and the fracture mechanics methods are employed for the calculation of preexisting crack growth rates. The residual stress state in the material heavily influence the fatigue crack initiation and crack propagation.

2.4.1 High-cycle fatigue

In the high-cycle fatigue test, the specimen is subjected to a large number of load cycles until the failure, normally more than 10^5 cycles. Test machines can apply different modes of loading such as reversed bending, rotation, axial tension and compression. These test machines are modern test frames; they are servohydraulically controlled and support desired fatigue spectrum. Typically, the stress is cyclically varying between the maximum and minimum tensile stresses. The applied stress consists of two components — mean stress σ_m and variable stress σ_a [115] — as shown in Figure 2.9. The stress range σ_r is defined by the difference between maximum and minimum stress $\sigma_{max} - \sigma_{min}$. The mean stress σ_m is calculated as the algebraic average of the minimum and maximum stresses. The quantity defining the ratio of minimum to maximum applied stress is the stress ratio R .

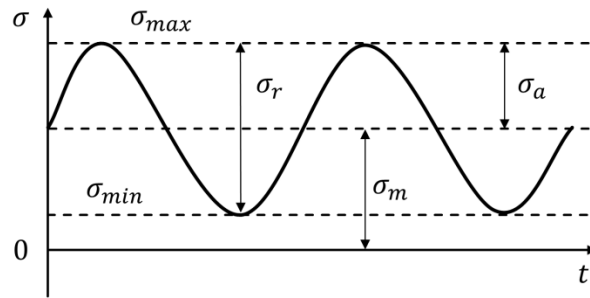


Figure 2.9 Tension-tension fatigue loading cycles.

Almost all applied stress cycles are spent on the crack initiation and only few additional cycles are required for subsequent failure of the specimen. The crack nucleation is originated at locations with maximum local stress and minimum local strength. Surface imperfections such as dents, burrs, scratches etc. may lead to the start of the crack. Except for the internal material defects or case hardening, all fatigue cracks initiate at the surface. The most influential factors are surface roughness and surface stress raisers, properties changes of surface metal, and residual stress condition of the surface. Therefore, in order to enhance the fatigue life, the surface crack initiation has to be prolonged or completely prevented. According to the last affecting factor, this can be achieved by the generation of compressive residual stresses in the material, with a high magnitude of the subsurface stress.

The influence of residual stresses generated by the LSP on the fatigue life was investigated by Correa et al. [116] and Bhamare et al. [85]. The ‘dog-bone’ specimen geometry and the sequence of laser peening pulses are presented in Figure 2.10.

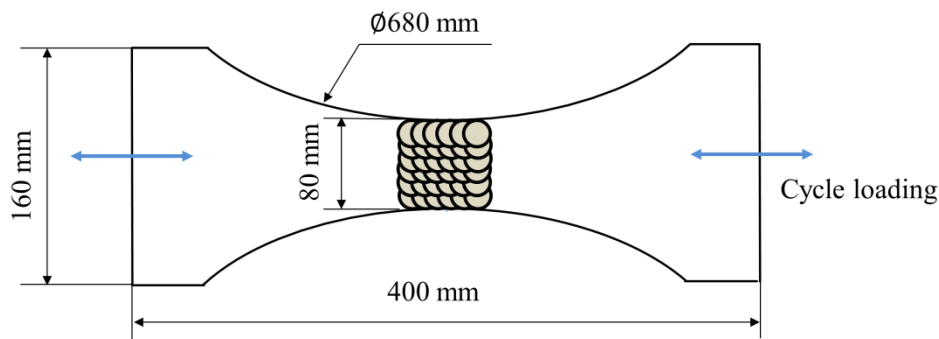


Figure 2.10 Fatigue test of LSP-treated specimen according to [116].

After the specimen’s failure, the fracture surface was examined with optical and scanning electron microscopes in order to track the crack initiation and propagation. Correa et al. [116] have demonstrated fatigue life extension due to the LSP treatment up to 243%, depending on a sequence of the LSP pulses on the specimen surface. It was shown that the crack is always

initiated at the specimen surface and then propagates through the thickness of the specimen, following a thumbnail-shaped pattern that matches the residual stress profile. The compressive residual stress acting opposite to the externally applied load suppresses the crack propagation, while the tensile stresses speed it up. Fatigue life extension was mainly achieved due to the prevention of the crack nucleation, which is attributed to the subsurface compressive stresses. On the other hand, the specimens with the subsurface tensile stresses do not demonstrate life extension, even if high compressive stresses are present in the body of the specimen. The tensile stresses promote crack propagation at higher rates, following the thumbnail pattern. Therefore, a magnitude of the subsurface stress is considered to be more important than the integral stresses through the thickness.

The effect of LSP processing on the fatigue life in the high cycle fatigue test is shown in Figure 2.11 [66]. Two treatment strategies were investigated: 1) the advancing peening direction is parallel to the fatigue load; 2) the advancing peening direction is perpendicular to the fatigue load. At the stress amplitude of 200 MPa, the strategy 1 produces fatigue life improvement by 166%, while the strategy 2 produces 471% fatigue life extension. The difference in the fatigue life improvement is due to the anisotropy effect in cartesian coordinates generated by the laser pulse sequence with the overlapping.

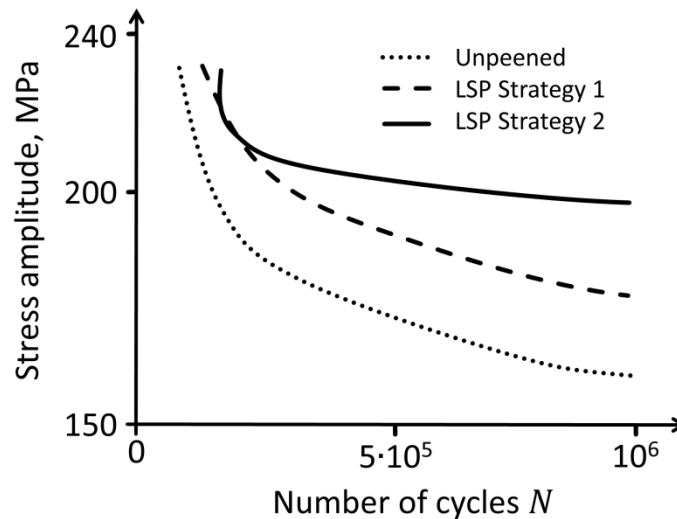


Figure 2.11 High cycle fatigue test of stainless steel 316L. Strategy 1: LSP advancing direction is parallel to the fatigue load; strategy 2: LSP advancing direction is perpendicular to the fatigue load. Depicted and adopted according to [66].

2.4.2 Fatigue crack propagation

The fatigue crack propagation test involves the application of cycle loading to the specimen with the preexisting crack length a_0 , until the crack reaches the critical length a_c , which corresponds to failure. The crack length a — as a function of the number of cycles N — determines the

fatigue growth life. Similar to the high-cycle fatigue, the tension-tension cycle loading is applied perpendicular to the crack propagation. The crack growth rate da/dN , or the amount of crack extension per loading cycle — as a function of crack length a — reflects the mitigation or acceleration of the crack growth. The crack growth rate increases with higher applied load and increasing crack length.

Fatigue failure or fracture of real structure components with the existing cracks can be predicted based on the experiments performed on coupon specimens, which is the objective of fracture mechanics. The local loading conditions at the crack tip are evaluated by the linear elastic stress intensity factor K , which is defined as follows [117]:

$$K = \sigma\sqrt{\pi a} f(a) \quad (2.1)$$

where a is the crack length, σ is the applied stress and $f(a)$ is the form function.

Such definition allows to link K to the crack length a and the applied stress σ , while separate form function $f(a)$, which also depends on the crack length, provides the effect of the specimen geometry. Hence, the stress intensity factor K relates the fatigue crack growth directly to the loading conditions at the crack tip and enables comparing the cases with different geometries, crack lengths and stresses.

The stress intensity factor K can be calculated using different approaches through either the energy balance or elastic stress field. Concerning the specimens containing the residual stress fields the energy balance based approach demonstrates very suitable results for the calculation of stress intensity factors [118]. The Griffith energy balance approach relates K to the energy release rate G , which defines influence of an incremental crack extension da on the elastically stored energy:

$$K = \sqrt{GE} \quad (2.2)$$

where G is the energy release rate, E is the Young's modulus and K is the stress intensity factor. Crack tip conditions under the cycle loading are described using stress intensity approach as follows:

$$\Delta K = K_{max} - K_{min} \quad (2.3)$$

$$R = K_{min}/K_{max} \quad (2.4)$$

where K_{min}, K_{max} are the minimum and maximum applied stress intensity factors of the load cycle, respectively; ΔK is the stress intensity factor range and R is the ratio of stress intensity factor. The correlation between fatigue crack growth rate da/dN and the $\Delta K, R$ can be found based on the experimental data [117]:

$$da/dN = f(\Delta K, R) \quad (2.5)$$

In Figure 2.12 this experimentally obtained correlation is presented. The fatigue crack growth rate can be divided into three regions. The threshold stress intensity factor range ΔK_{th} defines the lower limit in the region I where the crack does not propagate. While the fracture toughness K_c defines the upper limit in region III. A linear relationship between $\log da/dN$ and ΔK , so called Paris region, is seen in region II. The Paris law describing this region when the R is kept can be written as follows [117]:

$$da/dN = C \Delta K^l \quad (2.6)$$

where C, l are material constants. By increasing R the curve is shifting towards the lower ΔK values and higher da/dN . The Walker equation defines the crack growth law by including ΔK and R [117]:

$$da/dN = C [\Delta K [1 - R]^{m-1}]^l \quad (2.7)$$

where da/dN is the fatigue crack growth rate, C, l, m are the material constants, ΔK is the stress intensity factor range and R is the stress intensity factor ratio. In order to obtain the number of cycles N for a given crack length a , the inverse of the predicted crack growth rate can be integrated as follows:

$$\int_0^N dN = \int_{a_0}^a (C [\Delta K [1 - R]^{m-1}]^l)^{-1} da \quad (2.8)$$

The integration of Equation (2.8) yields the function $N(a)$, where the ΔK and R are correspondingly calculated. In what follows, the desired crack length can be determined as a function of the number of cycles $a(N) = N^{-1}(a)$, when assumed, that the crack growth rates are always positive.

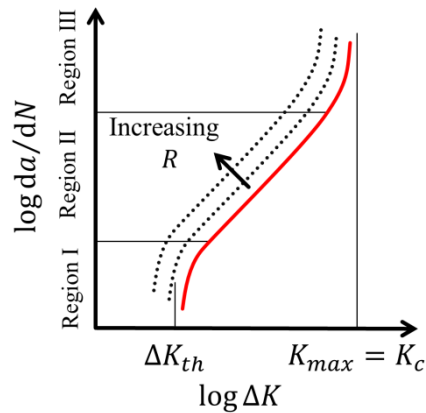


Figure 2.12 Fatigue crack propagation curve da/dN (ΔK) [117].

The residual stress state in the material affects the crack growth rate and therefore changes the fatigue life. A fatigue crack propagation test using a C(T)50 specimen with residual stresses generated by LSP is schematically illustrated in Figure 2.13. The LSP induces compressive residual stress fields in the material depth. For thin specimens up to 2-3 mm, the compressive stresses lie across the material thickness.

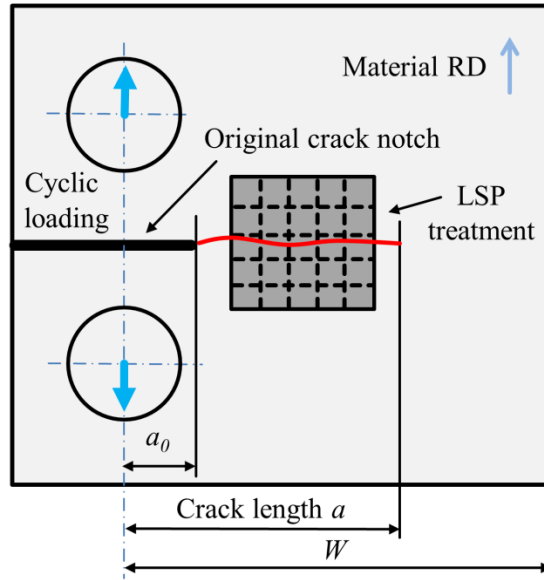


Figure 2.13 C(T)50 specimen ($a_0=10\text{mm}$, $W=50\text{mm}$) with LSP-treated area for the fatigue crack propagation test.

According to linear elastic fracture mechanics, the principle of superposition $K_R = K_{app} + K_{res}$ is used for characterization of the fatigue crack propagation in a residual stress field [119, 120]. K_{app} is the applied stress intensity factor, K_{res} is the stress intensity factor corresponding to residual stress and K_R is the resultant stress intensity factor. Substituting K_R into Equations (2.3) and (2.4) leads to:

$$\Delta K_R = ((K_{app})_{max} + K_{res}) - ((K_{app})_{min} + K_{res}) = (K_{app})_{max} - (K_{app})_{min} \quad (2.9)$$

$$R_R = \frac{(K_{app})_{min} + K_{res}}{(K_{app})_{max} + K_{res}} \quad (2.10)$$

where $(K_{app})_{max}$ is the maximum applied stress intensity factor and $(K_{app})_{min}$ is minimum applied stress intensity factor. As can be seen in Equations (2.9) and (2.10), the residual stress field influences only the load ratio R_R when the principle of superposition is used. Taking the residual stresses into account, Equation (2.5) can be expressed as follows:

$$da/dN = f(\Delta K_R, R_R) \quad (2.11)$$

However, the superposition method has two main disadvantages: (i) it does not account for the redistribution of the residual stresses during a crack growth [121]; (ii) it does not consider the crack closure effect which can be significant when compressive residual stresses exist in the material [120, 122, 123]. Regarding the last, an effective stress intensity factor range ΔK_{eff} is introduced through subtraction of the ineffective part of the stress intensity factor K_{op} , corresponding to the totally opened crack, from the nominal stress intensity factor K_{max} . As a result, fatigue crack growth rate can be defined as follows:

$$da/dN = C (\Delta K_{eff})^l \quad (2.12)$$

Much research has been carried out regarding the mitigation of fatigue crack growth via the residual stresses generated by laser peening [16, 17, 124–126]. Depending on the laser peening process parameters, the fatigue life of treated specimens can be increased by a factor of 10 relative to untreated specimens. The effect is attributed to the compressive stress component, acting perpendicular to the crack growth direction. Observations of the fatigue fracture surface reveal the grain size refinement in the LSP-treated area leading to crack growth retardation due to the counteraction with the longer grain boundaries [127]. The fatigue striation spacing decreases, thus emphasizing the crack growth deceleration. Moreover, in the treated area, the occurrence of the micro-fatigue-steps and secondary cracks contribute to the retardation of the crack growth. The through-thickness striations on the fracture surface of the thin specimen are formed parallel to the crack growth direction indicating the retardation regions. The crack arrest is attributed to the entering in the region with higher compressive residual stresses [124]. The secondary cracks appear between the fatigue striations at any depth of material. It was demonstrated that the magnitude of compressive residual stresses has a strong effect on the crack retardation. Higher compressive stresses are achieved by increasing the laser pulse energy or the number of treatment layers [124]. Furthermore, a through thickness compressive stress profile demonstrates higher fatigue performance in comparison with only a subsurface compressive stress layer such as the case of shot peening. This phenomenon is attributed to the fatigue crack closure due to the presence of compressive residual stresses; as well as the generation of secondary cracks and the local stress redistribution, causing a misorientation during the crack propagation.

The effect of LSP on microstructure and fatigue crack growth rate of AZ31B Mg alloy was recently investigated by Mao-Zhong Ge et al. [128]. The C(T)50 specimens with a thickness of 7 mm, shown in Figure 2.13, were processed using Q-switched Nd:YAG laser with a pulse energy of 10 J, laser spot size of 3 mm, overlapping rate of 50% and the pulse duration of 15 ns. The surface of the specimen was covered by the Al foil with a thickness of 0.1 mm. The fatigue crack growth rate $\log da/dN$ vs. the stress intensity factor range $\log \Delta K$ was obtained using Paris law Equation (2.6) from 12 specimens, and the results are presented in Figure 2.14 a). The crack

growth rate da/dN of treated and originally received samples continuously grows with the increasing ΔK , wherein the samples with LSP always demonstrate lower crack growth rate. The mitigation of fatigue crack growth is attributed to the following reasons: (i) presence of compressive residual stresses which causes the crack closure effect during the testing, (ii) grain refinement and the decreased amount of movable dislocations which makes the dislocation slip more difficult, (iii) the surface nanocrystalline layer restricts dislocation slip and impeding the formation of subsurface slip bands. In Figure 2.14 b) the crack length a is plotted over the number of cycles N for two specimens — LSP treated and untreated. As seen in the plot, the crack does not grow in the treated specimen until approximately 13000 cycles, which is clearly attributed to the compressive residual stresses. LSP processing leads to the extension of fatigue crack growth life by a factor of 2.5.

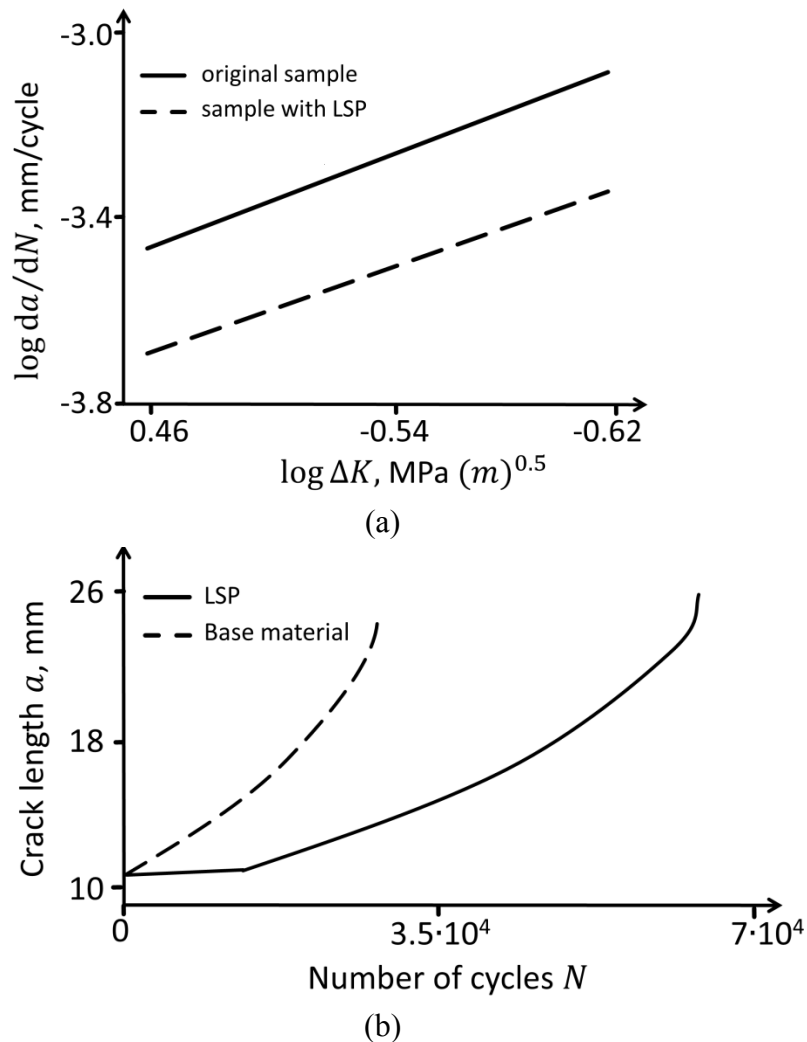


Figure 2.14 Fatigue crack growth test of AZ31B Mg alloy with and without LSP treatment: a) $\log da/dN$ vs. $\log \Delta K$, b) a vs. N . Depicted and adopted according to [128].

3. Methods

3.1 Experimental techniques

3.1.1 Material: AA2024-T3

AA2024-T3 is an advanced aluminum alloy mostly used in the aerospace industry, possessing excellent fatigue resistance, high fracture toughness, and high formability [129]. Due to its high strength-to-weight ratio, AA2024-T3 highly improves the damage tolerance of aircraft structures, and is especially used for wing and fuselage structures, which are loaded in tension, and also for gears, shafts, bolts, and hydraulic valve bodies. The composition of AA2024-T3 roughly includes 3.8–4.9% copper, 0.3–0.9% manganese, 1.2–1.8% magnesium, and less than a half a percent of silicon, zinc, chromium, lead, and bismuth [129]. It is a high-strength material of adequate workability and has also excellent ductility, which decreases not significantly under the strengthening heat treatment [130–132]. Moreover, it has good machinability and surface finish capabilities. It has a density of 2.78 g/cm^3 and melting temperature of about $500 \text{ }^\circ\text{C}$. A T351 temper of AA2024 was performed at a temperature of $413 \text{ }^\circ\text{C}$, leading to an ultimate tensile strength of 490 MPa , a yield strength of 370 MPa , a Young's modulus of 73.1 GPa , and elongation at break of 16% [133]. The Vickers hardness value is roughly $140\text{HV } 0.2$ [133].

3.1.2 Laser shock peening

The illustrations of the LSP process and LSP facility are presented in Figure 3.1 and Figure 3.2, respectively.

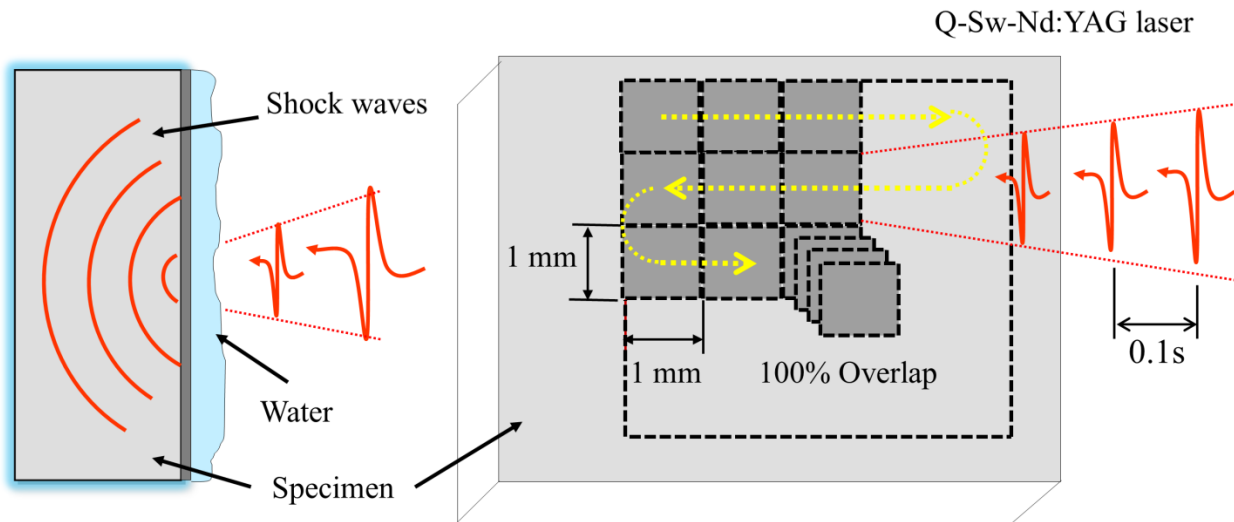


Figure 3.1 Schematic illustration of the LSP process.

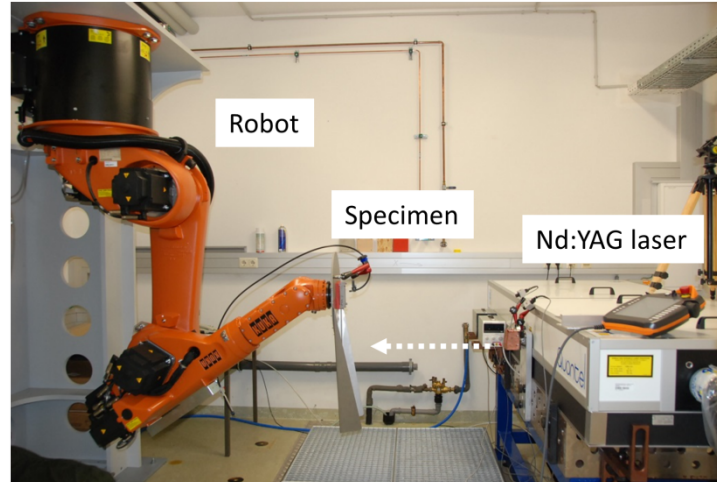


Figure 3.2 LSP facility consisting of Nd:YAG laser (right) and robot for specimen positioning (left).

The Q-switched Nd:YAG laser used in this work is capable of working at a maximum of 10 Hz frequency. The pulse duration can be switched between 10 ns and 20 ns. The material surface is covered with a laminar water layer, used as confining medium for the plasma. Specimens produced from AA2024-T3 sheets of 2mm thickness are treated with laser pulses sequentially along the path as shown in Figure 3.1. The laser beam is focused on the surface as a square spot using an optical system. Two different optics of 1×1 and 3×3 mm² are used in the experiments. For generating very deep compressive stresses an up to five times 100% overlap of the laser spot is applied.

3.1.3 Hole drilling system “Prism”

Residual stresses are measured using the hole drilling system “Prism,” presented in Figure 3.3. Prism is equipped with an optical electronic speckle pattern interferometer (ESPI), which provides high-quality full-field data for accurate residual stress determination [134].

After drilling a blind hole in the place where residual stress is to be measured, the material surrounding the hole immediately returns to the new stress equilibrium, leading to surface displacements around the hole. The laser beam of the ESPI lights the specimen surface. Natural roughness leads to the diffused light scattering, being captured by the camera from different directions. In consequence, the camera shows the image consisting of bright and dark spots — called speckle pattern — which is a defined feature of surface topology. The speckle patterns move when the sample surface shifts through relaxation.

Full-field optical data can be compared to continuously distributed infinitesimal strain gauges at the surface, measuring the surface displacements. Those surface displacements — projected along the sensitivity vector — have an explicit relationship with deviations in the phase angles at

the image pixels. Consequently, the Integral method—as a means for determining non-uniform residual stress fields from surface relaxations — is implemented for solving the inverse task by processing the measured full-field data [19, 20, 26] at incrementally increasing hole depth (for more details on the Integral method see Chapter 3.2.1). The Integral method calculates the residual stresses as a function of hole depth, based on the (simulation) reference, expressed as a triangular matrix of calibration coefficients. This matrix consists of hundreds of elements, each of which requires a separate finite element simulation. Essentially, the Integral method solves a system of equations using the least square technique, where the solution is a vector of residual stresses at a particular depth.

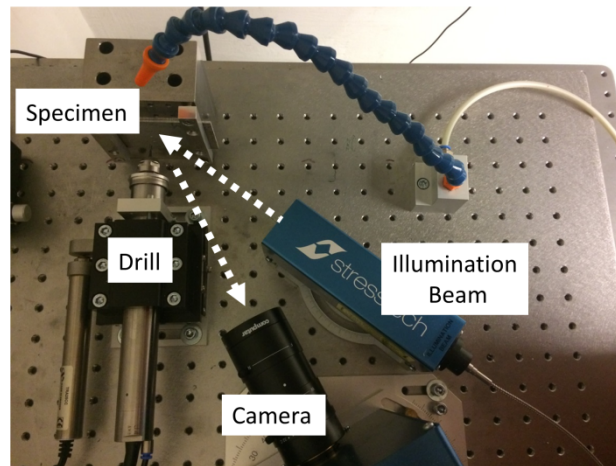


Figure 3.3 The hole drilling system “Prism,” equipped with ESPI.

3.1.4 Three-point bending

The three-point bending setup, as illustrated in Figure 3.4a), was used for generating through-thickness bending stress fields, which were then measured using the hole drilling system “Prism” [134]. The main advantages of the three-point bending are the simplicity of specimen preparation and the ease of experimental procedure for introducing a linear stress profile. Figure 3.4b) shows a schematic of the linear stress gradient through the thickness induced by bending within elastic limits.

A rectangular bar was subjected to the bend test. A sample — 100 mm long, 10 mm wide, and $h = 4$ mm thick — was placed on two supports with a span of $L = 80$ mm. A loading nose applied a force in the middle of the supports at an approximate rate of 0.1 mm/s. Inside the bend, the concave edge experienced the maximum compressive stress; outside the bend, the convex face was under the maximum tensile stress. These inner and outer edges of the bar are known as the extreme-loaded fibers. The bending deflection at the center of the sample is measured by two mechanical strain gauges mounted between the sample and the loading actuator, and the results are averaged. The hole drilling system was placed in front of the sample, as shown in Figure

3.4a), such that the drill was perpendicular to the convex surface of the specimen. This setup enabled the generation and measurement of linearly decreasing tensile stresses in y-direction, along the depth of the material. The flexural modulus was used as an indication of the material's stiffness when bent.

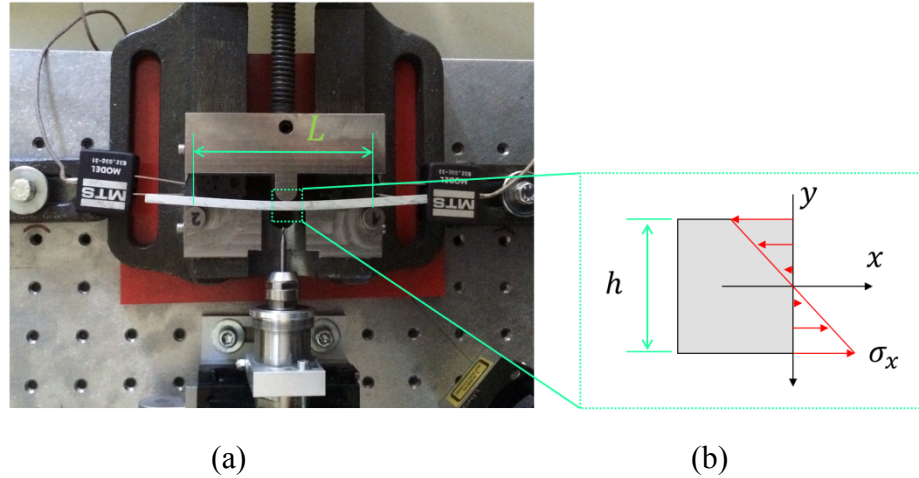


Figure 3.4 a) Experimental setup of the three-point bending, b) bending stress profile generated in the specimen.

The elastic bending stress distribution is calculated using a widely known mathematical expression:

$$\sigma_x = 6 \delta E h / L^2 \quad (3.1)$$

where σ_x is the maximum stress, δ denotes the deflection (displacement in y-direction at the center of the specimen), E is the Young's modulus, and h and L are overall dimensions. Knowing this stress value, the profile over the depth was obtained from the linear variation through the sample thickness, Figure 3.4b). The experimental curves were determined by averaging the data from five separate measurements on the same specimen loaded by the flexural system, with a fixed bending deflection. All measurements were taken at the center of the specimen.

3.1.5 Fatigue crack propagation test

The set-up for the fatigue crack propagation measurements is shown in Figure 3.5. A servo-hydraulic testing machine with a capacity of 25 kN is used for the application of cyclic loading to the specimen, with a stress ratio R of 0.1 and a frequency of 10 Hz at the room temperature. The C(T)50 compact tension specimens according to the ASTM E647-11 standard [135] with a width $W = 50$ mm are used. The C(T)50 specimens are machined such that the loading is axis parallel to the rolling direction of the sheet material. An initial crack of $a_0 = 10$ mm is introduced by an electro discharge machining. All specimens are polished in the area where the crack is expected to grow to observe the experiment by using an optical microscope. The fatigue crack

length is monitored on the observable surface using the optical microscope. The applied load vs. crack opening displacement (COD) is measured by the clip gage mounted on the notch of C(T)50 specimen. The incremental polynomial method is used for the calculation of the crack growth rate.

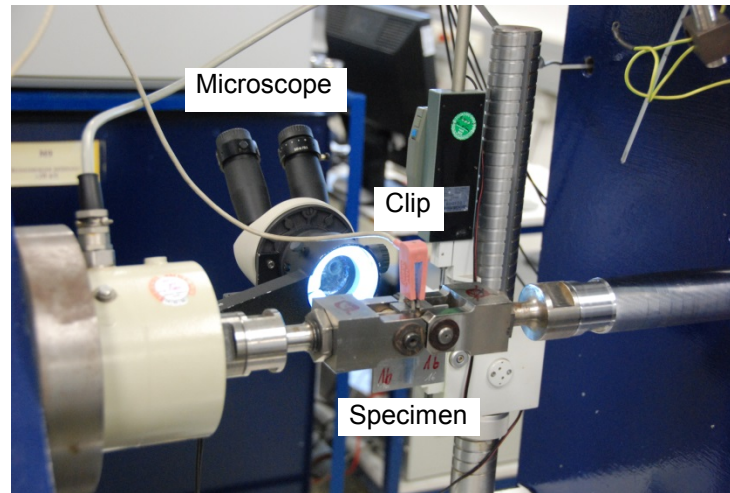


Figure 3.5 Fatigue crack propagation test.

3.1.6 Design of experiments

The exploration of a process property relationship can be achieved by conducting experiments in a systematic manner. The development of an experimentation strategy that minimizes resource use and yields the maximum knowledge requires tools involving statistical methods such as Design of Experiments (DOE) [136–139]. Especially for such processes that cannot be described by simulations, the experimental design techniques are very important.

The design and analysis of experiments investigate the effects of process variables on others; i.e. they find the relationship between independent (factors) and dependent (responses) variables. The factor values in the experiment are referred to as levels. The combination of investigated factor levels is called a treatment. The experiment is considered to be balanced if the number of response observations is the same for every treatment. Replicates are the repeated observations of a treatment. The number of factor levels to be investigated determines the number of treatments. For instance, an experiment including three factors with k , l and n levels respectively can have a maximum of $k \cdot l \cdot n$ treatment combinations [137]. In cases when all $k \cdot l \cdot n$ combinations are conducted, the experiment is referred to as a full factorial. Such an experiment design investigates all factors and their interactions — the relationship wherein the effect of the factor on the response is altered because of the presence of other factors.

The one-factor-at-a-time method does not provide full information about the factor effect on the responses when other factors exist, as is often the case in industrial applications. Moreover, the

effect of individual factors is often less important than interaction effects. In this context, DOE provides powerful statistical methods, ensuring systematic investigation of all vital factors and their interactions. DOE consists of four stages — planning of experiments, factor screening, factors optimization, and model verification [140].

Factor screening involves establishing the regression model, which defines the complex relationship between the factors and responses. Afterwards, at the optimization stage, the best setting of the factors for achieving the desired range of the responses is determined. Finally, these factor settings are verified by performing follow-up experiments for the confirmation of the established model.

According to the state of the art presented in Chapter 2.4, subsurface residual stresses in the material have a strong effect on the fatigue behavior of thin-walled structures, while the fatigue crack propagation behavior is significantly influenced by the through-thickness residual stress profile. The LSP parameters should be optimized, thereby providing the desired residual stresses, which simultaneously enhance fatigue and fatigue crack growth life. At the planning stage of the DOE, the responses attributed to the LSP-generated residual stress profiles were defined as follows: *stress at 0.01 mm* ($S_{0.01}$) depth, *stress at 0.5 mm* ($S_{0.5}$) depth, and the integral *stress area* (S_A) under the stress curve. The responses are schematically presented in Figure 3.6.

Another aspect is that the performance of the LSP process should be kept at the lowest cost rate. The cost of the treatment is regulated by the density of the laser pulse energy, laser pulse frequency, and a number of treatment layers. The energy density is defined by the *optics* system, which focuses a laser beam into a square spot, and the pulse energy. From this, it follows that the cost of laser peening performance is uniquely defined by the laser pulse energy, layer overlapping, and the focusing optics.

In this regard, the factors are defined as follows: the *energy* of the laser pulse, the number of *overlap* of LSP spots, and the focusing *optics*. They are schematically illustrated in Figure 3.7. The laser energy levels are defined as 1.3, 3, and 5 J in order to cover the range of pulse energy of the LSP facility. A total of 1 and 3 mm of square optics with areas of 1 mm² and 9 mm² respectively, are used. The number of overlap varies up to three times, which is typically used in industrial applications with energies of up to 5 J and a frequency of 10 Hz.

The general full factorial design is employed for the systematic investigation of all main and interaction-based factor effects. The structure of the general full factorial design is shown in Figure 3.8. The combinations of factor levels, consisting of 18 unique runs, are replicated three times in order to enhance the ability of the DOE to determine the factor effects. In all, 54 experiments were designed. The DOE study was performed using the software ReliaSoft DOE++ [141].

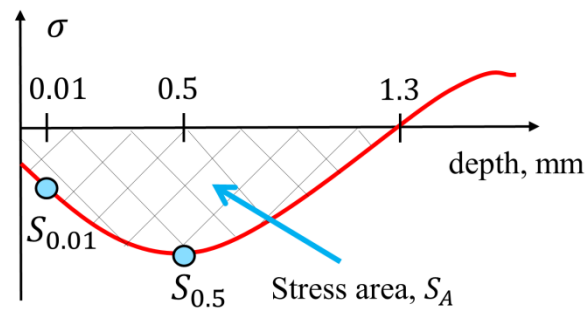


Figure 3.6 Response variables related to the LSP-induced residual stress profile.

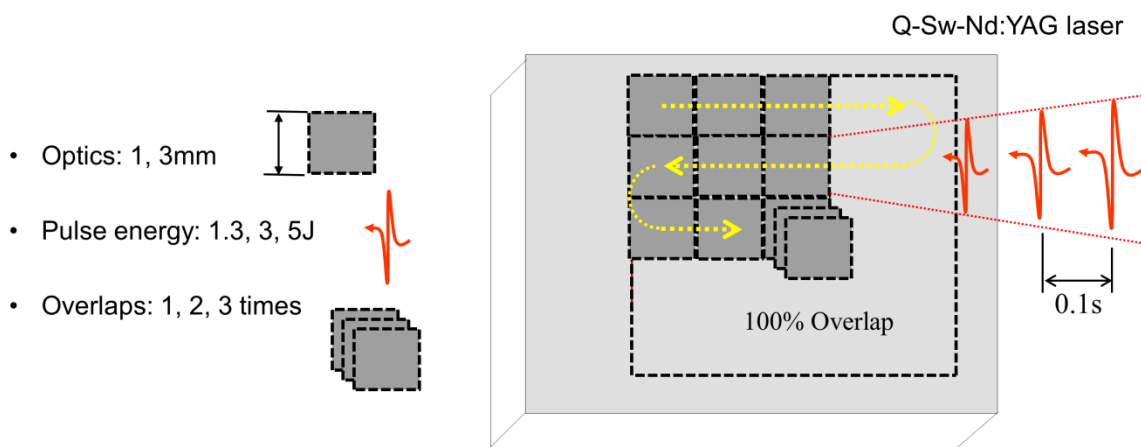


Figure 3.7 Factor variables related to the LSP process.

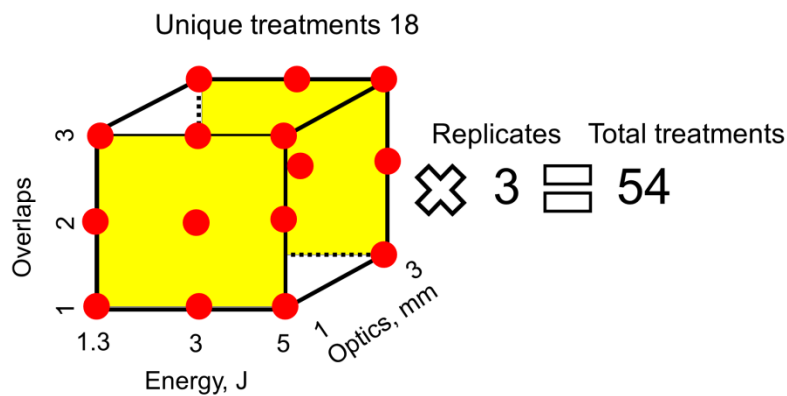


Figure 3.8 The structure of the general full factorial design.

The design evaluation of the planned experiments is defined by the power quantity, i.e. the probability of determining an effect of the factor or factor combinations on the responses, if any [140, 142]. The power study allows the definition of a sufficient number of replicates, which determines the best size of the sample with the probability specified in the objectives [140, 142].

Thereby, one can determine the amount of resources needed for achieving the goals. The statistical variance increases with the conducting of more replication runs, which also improves an accuracy of the regression model for prediction. However, the measurement variability increases with increasing number of experiments, which is attributed to the experimental systematic and random errors [137, 140]. Therefore, particular attention is paid to model accuracy when defining the size of the model. All factor combinations investigated in the general full factorial design provide the factor effects and interactions free of aliasing, which means that the design distinguishes the effects with defined probability.

An indicator of the acceptance of the regression model for the data-fitting is T-value [137, 140, 142]. The T-value is defined by the statistical hypothesis test and stands for an amount of effect of a factor or factor interaction on a response; i.e. how significantly the term influences a response in the presence of other terms. T-value is used for screening factors according to their importance. A factor is considered to be significant when its T-value exceeds the critical value of the test statistics, which is determined by the significance level. In statistics, the significance level provides the probability of statement rejection (here, factor significance) and is defined by the critical region area as a fraction of the whole area under the Student's distribution. In this work, the significance level is 0.1 or 10%.

When the T-value of the factor is lower than the critical value, the factor is considered unimportant; however, this inference does not reflect how far the test statistic reaches into the critical region. The P-value [137, 140, 142] is used for clarifying this statement. It is the probability of obtaining the test statistic (T-value) equal to or more unfavorable than the observed result. When the test statistic is defined, the P-value means the lowest level of significance that would yield the rejection of factor significance. The factor is important when the P-value does not exceed the significance level, which is determined to be 10% in this work.

The appropriateness of the regression model is examined by an amount of variability before making relevant inferences. Model variability — i.e. how well the regression model fits the experimental data — is determined by the R^2 factor [137, 140, 142, 143].

For further model verification, the analysis of residuals is required [143]. Residual is the difference between experimental data and model data fit. The model is adequate when residuals follow the normal distribution with zero mean and do not build any patterns over the fitted values of the response on the graph.

3.2 Numerical methods

3.2.1 Integral method

According to [32], Figure 3.9 shows a schematic of the area where hole drilling is applied. Residual stresses are assumed to be uniform through the depth, and shear stresses at the hole surfaces are neglected. The cross-sectional view, as presented in Figure 3.9a), illustrates the loading applied externally to the hole surface, which is needed to replace the initially existing stress before the hole is drilled; thus, the stress distribution and deformation are maintained.

The main assumption of the method is the fully linear elasticity of the material during the drilling of the hole. By considering the material to be linearly elastic, the principle of superposition can be applied to the model, as shown in Figure 3.9. In the “summand” case in Figure 3.9b), the loading is applied to the hole surface with the opposite sign but equal value to the force in Figure 3.9a), whereas the boundaries are unstressed. The result of the superposition shown in Figure 3.9c) expresses the residual stress distribution after the hole has been drilled. In conclusion, the loading case in Figure 3.9b) represents the residual stress redistribution, which in turn causes strain relaxations at the top surface. These relaxations are measured by strain gages and then used for the calculation of residual stresses. It is worth noting that the measured strain relaxations are caused only by residual stresses initially existing at the hole surface [32] and are assumed not to be affected by the drilling process.

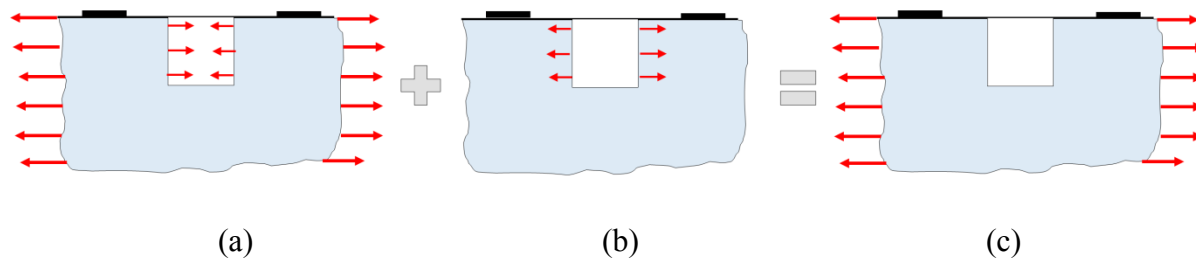


Figure 3.9 Superposition of loadings for hole drilling simulation; a) original stress state, b) stress redistribution, c) final stress state. Depicted and adopted from [32].

All destructive methods for residual stress measurements have a main feature, which involves the elimination of the material in the place where residual stresses are to be determined and the measurement of deformations in the area surrounding the removal. The different locations of stresses varying over the depth and measured deformations at the top surface make the inverse procedure computationally challenging. ESPI provides a large amount of data about displacements from certain points within the optical image, thereby substantially enhancing the measurement accuracy and reliability. However, the computational challenge is to use all the data properly and efficiently to save time and computational resources.

For the calculation of the stress profiles [144], the measured deformations depend on the contributions of the various stresses originally existing in the removed layers of material. The integral relationship between the deformation at the top surface point and the depth-dependent stress is as follows:

$$d(h) = \int_0^h G(H, h)\sigma(H)dH \quad (3.2)$$

Here, $G(H, h)$ is the main function providing the information about deformation caused by a unit stress at depth H within a hole of depth h , and $d(h)$ is the measured deformation parallel to the specimen surface, as a projection on the sensitivity vector, while the out-of-plane displacement component is neglected. $\sigma(H)$ is the in-plane equivalent uniform stress. In case of equal biaxial stress profiles induced by LSP, the equivalent uniform stress equals each of the biaxial components. The stress profile enclosed within the integral can be determined by an inverse approach. A widely accepted way to solve this inverse problem is by the expansion of the stress as a series [144]:

$$\sigma(H) = \sum_{j=1}^n c_j u_j(H) \quad (3.3)$$

Here, $u_j(H)$ are the pulse functions and c_j are the numerical coefficients to be calculated. Both Equations (3.2) and (3.3) compose the final matrix equation:

$$\vec{G} \cdot \vec{c} = \vec{d} \quad (3.4)$$

where

$$G_{ij} = \int_0^{h_j} G(H, h_i)u_i(H)dH \quad (3.5)$$

The pulse function G_{ij} is illustrated schematically in Figure 3.10, where coefficient G_{32} reflects the deformation caused by a unit stress within Step 2 of a hole that is three increments deep. More details about the pulse function G_{ij} can be found in the work of Schajer [21]. For a given geometry and loading situation, the corresponding relaxation matrix is obtained through FE simulations. Every component in the displacement vector \vec{d} is the projection of surface displacement on the sensitivity vector, which in this study is defined to be lying on the specimen surface and passing through the center of the hole. Given that the surface deformation d can be measured, the inverse solution can be implemented by solving the system of Equation (3.6) or Matrix Notation (3.7):

$$\sum_{j=1}^{j=i} G_{ij} \sigma_j = \frac{E}{1 + \vartheta} d_i \quad 1 \leq j \leq i \leq n \quad (3.6)$$

$$\bar{G} \vec{\sigma} = \frac{E \vec{d}}{1 + \vartheta} \quad (3.7)$$

Here, E is the modulus of elasticity, ϑ is the Poisson ratio, the term $E/(1 + \vartheta)$ describes the dependence of the material relaxations on material properties, n is total number of hole depth increments, and $\vec{\sigma}$ is the equivalent uniform stress. The shapes of \bar{G} , $\vec{\sigma}$, \vec{d} are as follows:

$$\bar{G} = \begin{pmatrix} G_{11} & \cdots & 0 \\ \vdots & G_{ij} & \vdots \\ G_{n1} & \cdots & G_{nn} \end{pmatrix} \quad \vec{\sigma} = \begin{pmatrix} \sigma_1 \\ \vdots \\ \sigma_j \\ \vdots \\ \sigma_n \end{pmatrix} \quad \vec{d} = \begin{pmatrix} d_1 \\ \vdots \\ d_j \\ \vdots \\ \sigma_n \end{pmatrix} \quad (3.8)$$

The size of the lower triangular matrix \bar{G} depends on the level of discretization. The more elements are contained in the matrix, the more accurate is the solution provided by Integral method. In this study, the relaxation matrix is 20×20 . This allows the determination of the stress profiles with an uncertainty less than 2% in the elastic case. This source of error can be neglected compared to the effect of plastic deformation.

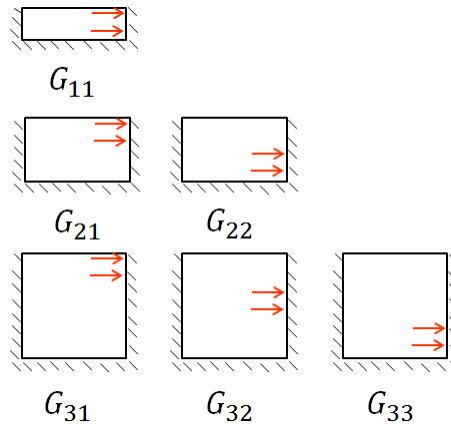


Figure 3.10 Physical interpretation of matrix coefficients G_{ij} , according to [21].

One of the applicable computational methods for solving matrix equations is the least-squares fit. Because of the full-field measurement, the number of unknowns greatly exceeds the number of stress quantities to be determined. A least-squares solution provides the “best fit” to the measured data in this overdetermined calculation. The data corresponding to the resulting solution differs from the measured data, wherein the difference is called “misfit.” Typically, the misfit has a random character and is associated with the measurement noise.

3.2.2 Finite element method

Finite element modelling can be reliably used to simulate strain relaxations at the specimen top surface, as they are caused by applying the loading to the curved surface of the hole externally with the opposite sign, according to Figure 3.9b) [19]. By following the assumption that residual out-of-plane normal and shear stresses are neglected and all free surfaces are unstressed, two different models are used in this study to simulate equibiaxial and uniaxial stress distributions corresponding to the LSP-induced stress fields and flexural bend stress fields respectively. MSC Patran 2012.2 [145] and ABAQUS 6.13-1 [146] were employed as pre-processor and solver respectively. The Integral method was implemented in Python [147].

In the case of an equibiaxial stress field, the FE model and loading are axisymmetric; therefore, axisymmetric bilinear quadrilateral elements CAX4 are used. The FE mesh of this model, as shown in Figure 3.11, consists of 5,985 elements and was created in the Patran FE package and exported to ABAQUS. The mesh discretization on the top surface was adjusted according to the resolution of the full-field surface displacement data of the camera of the hole drilling system “Prism.”

The mesh had to be modified for introducing the hole. This was realized by removing elements within the given hole boundaries for each depth increment of the drilling process using Python. Each depth increment is therefore represented by a separate FE mesh, where all elements within the hole are removed for the given depth before the stress is applied to the hole’s surface in a static simulation. Rate effects or temperature effects from the drilling process are not considered. A fine mesh size of 0.025 mm (square elements) was applied in the area surrounding the hole, and a mesh size of 0.1 mm was used near the far boundaries. The mesh size was gradually decreased from the hole towards the boundaries, using the Patran transition triangular option. Simulations were performed for each increment of a given hole depth. In total, 10 equally spaced increments were used along the depth. The hole diameter is 2 mm, the height of the model is 2.5 mm, and the far boundary diameter is 6 mm.

To apply the stress profile according to Figure 3.9b), element edges on the vertical hole surface were loaded using a *DLoad* subroutine. The stress given over the depth was applied normally to the curved surface according to Equation (4.1).

The nodes at the bottom of the model are restricted to moving downward in the vertical direction due to the frictionless ground, while those at the symmetry axis are fixed in the horizontal direction. Moreover, the bottom-left node is restricted vertically to prevent the body movement. The relationship between the residual stresses and the strain relaxations was obtained through separate simulations and stored as a relaxation matrix.

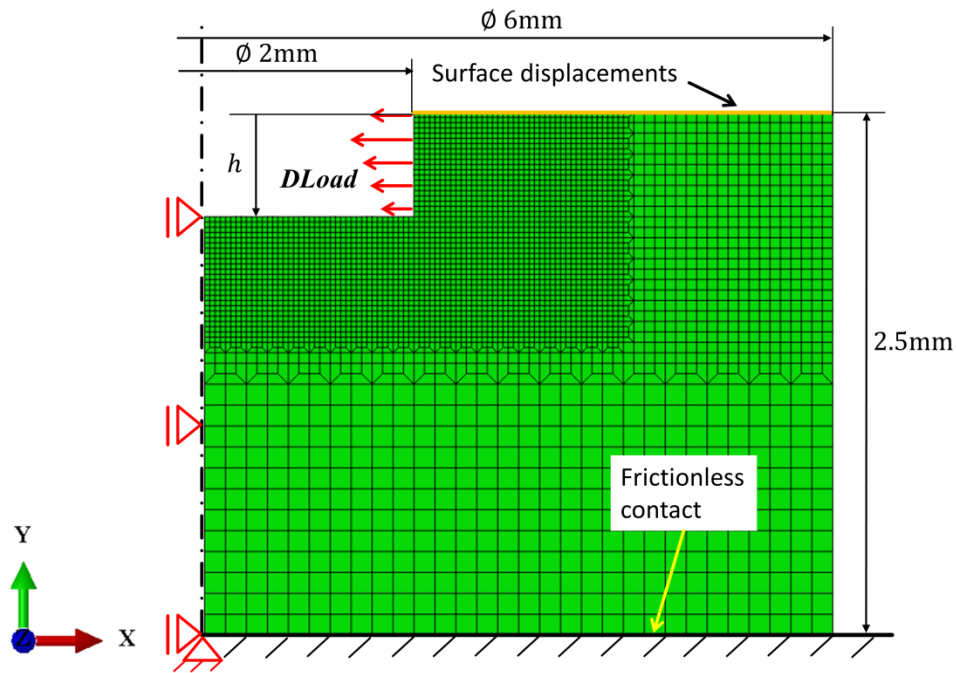


Figure 3.11 Axisymmetric finite element mesh used for the simulation of the equibiaxial stress field.

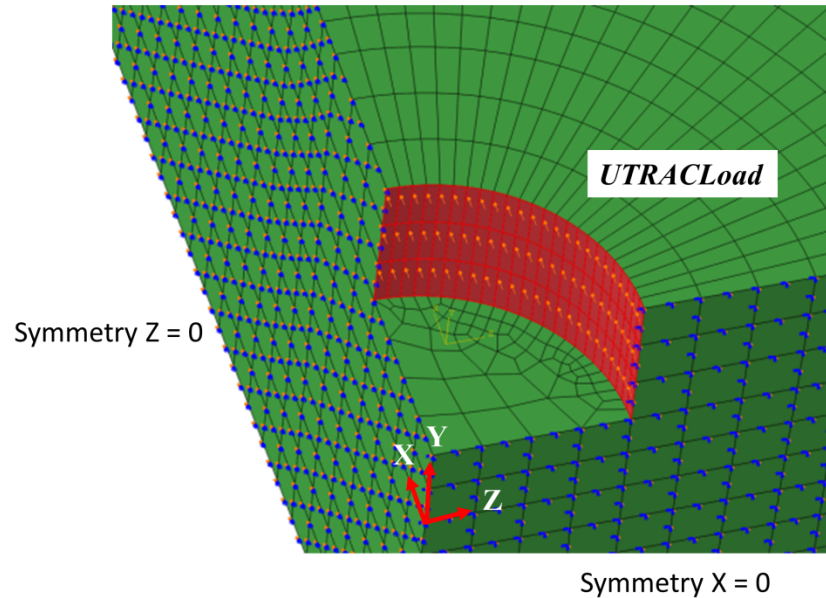


Figure 3.12 3D finite element mesh used for the simulation of the uniaxial stress field.

For the simulation of flexural bend stresses σ_x according to Equation (3.1), 3D model was created to capture the specimen geometry and allow the application of a uniaxial stress distribution. Because of the symmetry, only a quarter of the whole specimen was meshed, as

shown in Figure 3.12. The model was 10 mm long and 2 mm thick, consisting of 7,886 solid 3D20R elements with reduced integration points. Symmetry boundary conditions $X = 0$ and $Z = 0$ we applied as shown in Figure 3.12. Similar to the 2D model, the nodes at the bottom of the model are restricted to move downward in the vertical direction due to the frictionless ground (not shown in Figure 3.12) and the node $X = 0, Z = 0$ on the bottom surface (not shown in Figure 3.12) is restricted vertically to prevent the body movement. Hole elements were removed according to the depth increment. The hole diameter was 1.2 mm.

The subroutine *UTRACLOAD* was used to apply the uniaxial stress loading normally to the bending deflection on the curved hole surface, where the stress linearly decreased through the depth according to the following equation:

$$\sigma(y) = \sigma_0(my + n) \quad (3.9)$$

In Equation (3.9), σ_0 denotes the maximum stress at the specimen surface, while m and n are coefficients that specify the stress gradient. The relaxation matrix for such a stress distribution is determined numerically and is limited to the determination of flexural bending stresses for the given geometry parameters.

Figure 3.13 represents the true stress-plastic strain curve of AA2024, obtained from experimental tensile test data [133]. An isotropic strain-hardening plasticity model was used in all simulations; hence, Young’s modulus E of 73.1 GPa, Poisson’s ratio ν of 0.33, yield stress σ_{yield} of 370 MPa, and the hardening curve define the material properties.

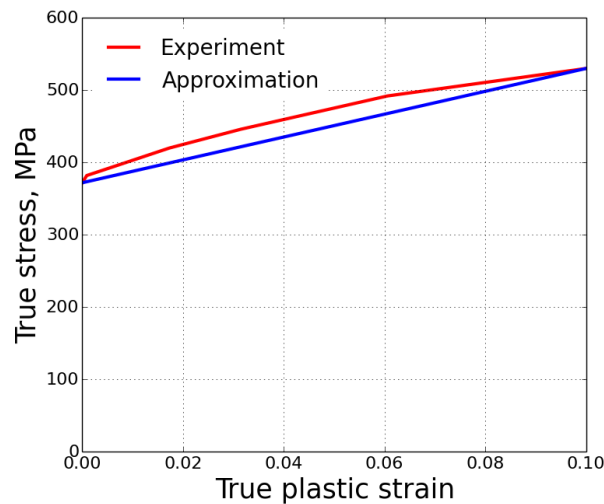


Figure 3.13 True stress-plastic strain curve for material hardening of AA2024-T3.

The von Mises yield criterion with isotropic hardening was used. Isotropic hardening implies that the yield surface changes size uniformly in all directions such that the yield stress increases in all

stress directions as the plastic straining occurs. According to the von Mises yield surface, isotropic hardening is defined by providing the values of uniaxial yield stress as a tabular function of uniaxial equivalent plastic strain.

3.2.3 Artificial neural network

Artificial neural networks (ANNs) are computational tools modeled on the interconnection of the neuron in the nervous system of the human brain; they represent a type of non-linear processing that is ideally suited for tasks where the solution does not exist as a closed form relationship [148]. The ANN can be trained to approximate any kind of nonlinear relationship using a training algorithm and sample data consisting of so-called patterns. In the past two decades, ANN have been successfully applied for solving complex direct problems aimed at predicting or analysis [149] as well as inverse problems, typically dealing with the identification of mechanical properties [150–157]. In the following section, only a brief description is given. More details can be found in the given references.

In Figure 3.14, a sketch of a hierarchical neural network is shown. It consists of neurons connected with links to a highly parallel structure. Each neuron possesses a local memory and can carry out localized information processing operations. Furthermore, each neuron is a multiple-input, multiple-output system that receives signals from the inputs, produces a resultant signal, and forwards that signal to all neurons of the next layer. The first and last layers serve as input and output layers respectively. Layers between the input and the output layer do not interact with the environment and are denoted as hidden layers. The number of input and output neurons is defined by the problem under consideration. By increasing the number of neurons in the hidden layers, the complexity of an ANN can be increased. In this way, the neural network can be adapted to the degree of nonlinearity and complexity of the problem at hand.

The inputs are operated and transformed into the output by the state transition rule

$$v_j = \sum w_{ij}y_i + \theta_j \quad (3.10)$$

$$y_j = f(v_j) \quad (3.11)$$

where y_i in Equation (3.10) and y_j in Equation (3.11) denote the output from a neuron i acting as an input on neuron j and the output of neuron j respectively. w_{ij} is the synaptic weight, θ_j is the offset, and v_i is the state variable of the synaptic weights, which implies the connection strength between the neurons. The weighted signals are summed up in v_j and transformed into the output signal through an activation function. In this paper, the activation function is given by the smooth sigmoidal function

$$f(v_j) = 1/(1 + e^{-v_j}) \quad (3.12)$$

which takes values between 0 and 1. The derivative of Equation (3.12) is easy to calculate. This is needed for calculating the weight updates in the training algorithm using a gradient approach as optimization algorithm. The derivative is given by

$$\frac{df(v_i)}{dv_i} = f(v_i)[1 - f(v_i)] \quad (3.13)$$

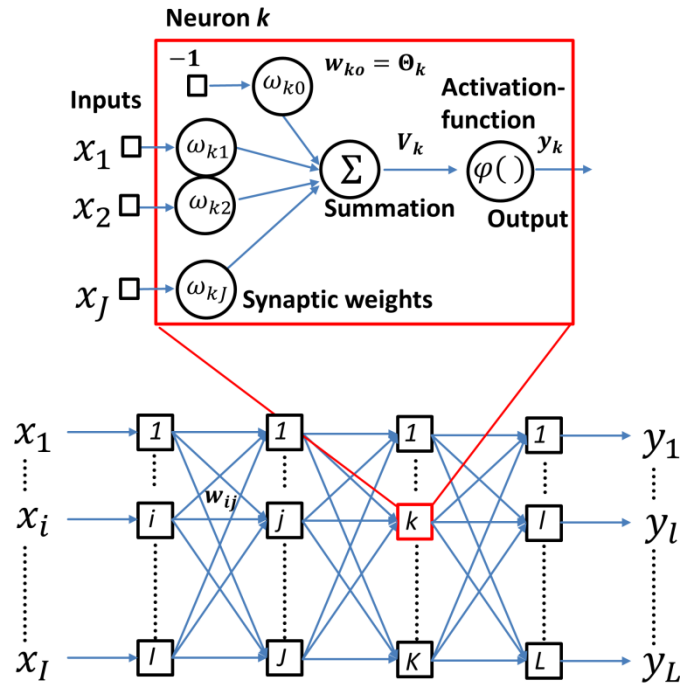


Figure 3.14 Sketch of a multilayer feedforward neural network according to [148].

The main features of hierarchical neural networks as are used in this work can be summarized as described by Yagawa and Okuda [149]:

- One can automatically construct a nonlinear mapping from multiple input data to multiple output data in the network through a learning process of some or many sample input vs. output relations.
- The network has a capability of so-called “generalization,” i.e. a kind of interpolation, such that the trained network estimates appropriate output data even for unlearned data.
- The trained network operates quickly in an application phase. The CPU power required to operate it may be equivalent only to that of a personal computer.

The training is in general performed by minimizing the value of an error function

$$E = \hat{E}(d_l(n), y_l(n), w_{ij}) \quad (3.14)$$

here, d_l is the desired output and y_l is the calculated output at output neuron l for a certain pattern n . Training is carried out using a backpropagation algorithm — one of the most popular and robust tools in the training of ANNs — where the weights w_{ij} are adjusted by a steepest descent method.

The code for simulation and training of the neural network has been written in the Python object-oriented programming language and makes use of the “Rprop” algorithm [158]. Rprop stands for “Resilient backpropagation” and is a local adaptive learning scheme, performing supervised batch learning in multilayer neural networks. The error function is defined by

$$E = \sum_{n=1}^N \sum_{l=1}^L (d_l(n) - y_l(n))^2 + 10^{-\alpha} \sum w_{ij}^2 \quad (3.15)$$

where the left part represents the error of the L outputs and all N patterns, while the right part is the norm of the weight vector. In minimizing E , both the output error as well as the values of the synaptic weights are adjusted as small as possible, having the effect of improving the generalization of the network. The size of the weight change is exclusively determined by a weight-specific update value $\Delta w_{ij}^{(t)}$

$$\Delta w_{ij}^{(t)} = \begin{cases} -\Delta_{ij}^{(t)} & \text{if } \left(\frac{\partial E}{\partial w_{ij}} \right)^{(t)} > 0 \\ +\Delta_{ij}^{(t)} & \text{if } \left(\frac{\partial E}{\partial w_{ij}} \right)^{(t)} < 0 \\ 0 & \text{else,} \end{cases} \quad (3.16)$$

where (t) denotes the number of epochs. The determination of the new update-values $\Delta_{ij}^{(t)}$ is based on a sign-dependent process:

$$\Delta_{ij}^{(t)} = \begin{cases} \eta^+ \Delta_{ij}^{(t-1)} & \text{if } \left(\frac{\partial E}{\partial w_{ij}} \right)^{(t-1)} \left(\frac{\partial E}{\partial w_{ij}} \right)^{(t)} > 0 \\ \eta^- \Delta_{ij}^{(t-1)} & \text{if } \left(\frac{\partial E}{\partial w_{ij}} \right)^{(t-1)} \left(\frac{\partial E}{\partial w_{ij}} \right)^{(t)} < 0 \\ \Delta_{ij}^{(t-1)} & \text{else,} \end{cases} \quad (3.17)$$

where $0 < \eta^- < 1 < \eta^+$. Rprop tries to adapt its process to the topology of the error function, by operating accordingly to the principle of “batch learning.” This means that the weight-update is performed after the gradient of the whole pattern set (one epoch) is computed.

The training code provides an error measure denoted by MSE in order to compare the quality of different neural networks during training, which can also be used for visualizing training and generalization properties:

$$MSE = (10^3/NL) \cdot \sum_{n=1}^N \sum_{l=1}^L (d_l(n) - y_l(n))^2 \quad (3.18)$$

The number of patterns N depends on the complexity of the problem and type of pattern set (training or validation). MSE values for training and validation patterns are comparable, i.e. $MSE_T \sim MSE_V$, when the neural network provides good generalization.

The absolute value of the relative error

$$err_l = |e_l/d_l| = |(d_l - y_l^N)/d_l| \quad (3.19)$$

has been introduced in order to analyze the error distribution of the identified values for all patterns, where l denotes the output unit. Also for an output quantity y_l , we denote the confidence interval by err_l 90%, which is defined as the err_l containing 90% of all training patterns.

4. Methodology for correction of measured residual stresses

The hole drilling method is based on elasticity assumption; therefore, it yields an error when plasticity effect occurs by measuring residual stresses approaching the material yield strength. In this regard, the Integral method — the procedure of residual stress determination from measured strain data (see Chapter 3.2.1) — becomes highly nonlinear, which makes correction of measured residual stresses very challenging. Therefore, before solving the direct problem of stress correction the inverse problem needs to be solved.

The Integral method is realized using the finite element model introduced in Chapter 3.2.2, involving elasto-plastic material behavior with given material properties and given (predefined) residual stress profile. The resulting (simulated) stress profile is obtained by application of the back-calculation procedure. Afterwards, by comparing the simulated and predefined stress profiles, the stress determination error is calculated. In order to validate the finite element model involving plasticity, the known residual stress profile (identical to the predefined stress profile in simulation) is generated by the three-point bending system and is then measured by hole drilling. The measured stress profile is then compared to simulated stress profile for the validation of simulation results. When the finite element model is validated, it can be used for the simulation of different residual stress profiles and material behaviors.

4.1 FE model validation

Figure 4.1a) illustrates sets of stress profiles varying over the depth with a linear gradient, as introduced by the three-point bending test at different loads. The maximal hole depth was 0.5 mm. Each set of curves consists of an empirically calculated profile using Equation (3.1), a stress profile measured by the hole drilling experiment, and a stress distribution determined from simulations by applying the Integral method. For convenience, a dimensionless parameter called the stress factor (SF) is introduced as the ratio of the peak stress value to the yield strength. The stress factor is defined only for profiles with a maximum value close to the top surface. Figure 4.1a) represents several stress profiles with increasing stress factors, which emphasizes the ability of the hole drilling method to determine non-uniform stresses, even when plastic deformations are expected. Experimental data were averaged from five separate measurements for each stress profile to minimize errors from the ESPI and human factor. As mentioned before, hole drilling results must be considered with caution, owing to the certain theoretical assumptions that affect the accuracy of the measurements. Simulation results may also provide uncertainties, such as from the meshing, choice of elements, and the quality of the inverse solution.

The curves in Figure 4.1a), corresponding to the stress distribution with the stress factor 0.35, appear to be in very good agreement with each other. The mean absolute errors are 9.8 MPa and

4.5 MPa for the experiment and inverse approaches respectively; the corresponding standard deviations are 11.8 MPa and 5.1 MPa respectively. The agreement validates the approaches for both the experimental setup (including the hole drilling technique) and the FE model and its application for simulating a hole drilling procedure according to the Integral method. Furthermore, the uncertainties for both approaches are determined, which is important for the following discussion on the effects of plasticity.

A second stress profile was performed for the stress factor = 0.5, which is still within the application limit for the hole drilling method. In this case, the FE model provides quite a precise stress distribution up to moderate depths up to 0.25 mm and then tends to deviate to higher stress values. The mean absolute errors are 8.5 MPa and 9.5 MPa, while the standard deviations are 10.3 MPa and 11.7 MPa, for the experiment and inverse approaches respectively.

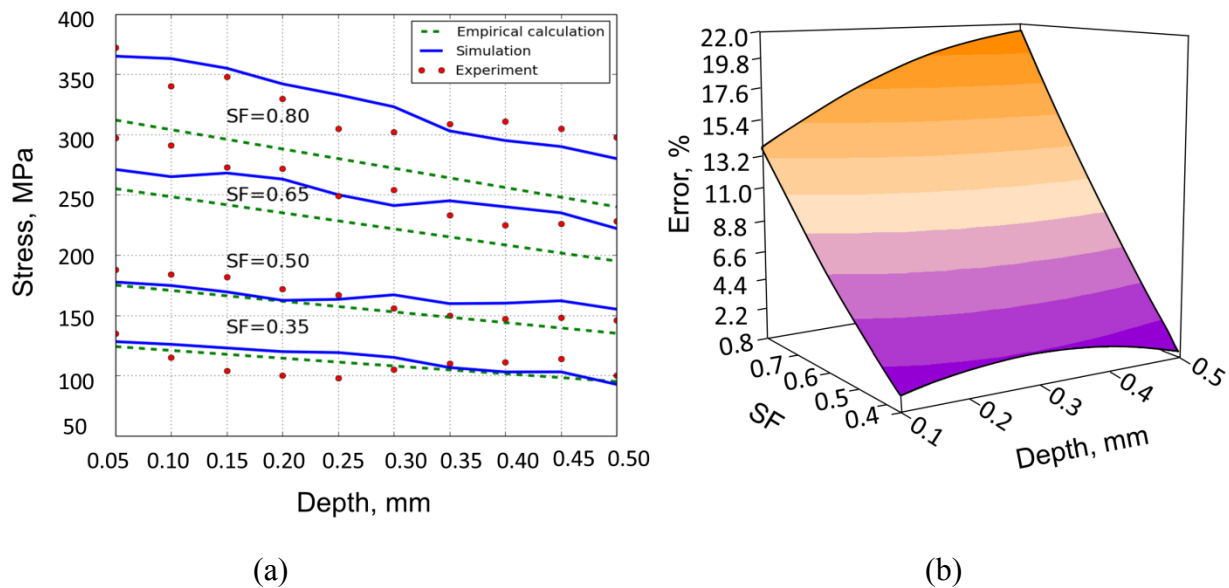


Figure 4.1 a) Stress profiles with linear gradient corresponding to different stress factors (SF), b) relative error in stress measurement as a function of stress factor and depth.

The third stress profile in Figure 4.1a) corresponds to the stress factor 0.65 and represents a stress level that violates the assumption of linearity. The mean absolute errors are 30.1 MPa and 26.4 MPa, while the standard deviations are 31.8 MPa and 27.1 MPa, for the experiment and inverse approaches respectively. It can be clearly seen that the measured and simulated profiles are similarly overestimated due to additional plastic deformation, which increases the top surface deformation during hole drilling compared to a pure elastic relaxation. Although no plastic deformation occurs in the initial undrilled state, higher stresses appear around the hole near the surface, which can cause local plastic deformation. Since the inverse approach for both curves is based on linear elasticity, the resulting increased surface relaxation is likewise interpreted as overestimated stress.

Finally, the fourth stress profile is shown in Figure 4.1a) at the top of the plot, which corresponds to the stress factor 0.80. In this case, the mean absolute errors are 44.2 MPa and 47.4 MPa for experiment and inverse approaches respectively, and the standard deviations are 45.9 MPa and 48.1 MPa. Here, measured and simulated curves are still similar but have become even more overestimated owing to the extended plastic yielding.

In the overview of the simulation results for all stress levels (blue curves in Figure 4.1a)) it can be observed that for lower stress factors up to 0.35, the method works well within experimental uncertainties and is characterized by elasticity. At a stress factor of 0.5, the first effects of plasticity occur for a hole depth exceeding 0.25 mm. This becomes visible from the increasing overestimation of the determined stress compared to the empirically calculated profile with increasing depth. For higher stress factors, the overestimation is present throughout the whole depth range. This means that there is a transition from fully elastic to elastic-plastic deformation. Within this transition, the point where plastic deformation becomes relevant depends on the hole depth. In conclusion, it is not only the stress factor but also the combination of stress factor and hole depth that is responsible for the degree of plastic deformation.

In Figure 4.1b), the relative measurement error is presented as a function of the stress factor and specimen depth. It can be seen that the error is initially almost constant over the whole depth range and constantly grows as the stress factor increases. In addition, there is some degree of experimental scatter which is also known to be influenced by the measurement principle, which has an increasing error sensitivity with increasing depth [20]. However, in our investigation, the comparison of the experimental data points and the predicted stress values in Figure 4.1a) do not indicate systematic deviations for larger depths. When the stress factor approaches its maximum of 0.80, the measurement error reaches 21% near the surface. For this case, Figure 4.2a) and b) show the equivalent plastic strain distribution in the FEM model and the contour plot of σ_x stress component, respectively. The deformation scale factor on the plot is exaggerated by a factor of 30. The plastic deformation results from the presence of the hole and the high stresses initially existing in the sample. The material surrounding the hole is locally plasticized, causing nonlinear deformations at the top surface of the specimen. Plasticity occurs in the area around the hole where the stress is parallel to the hole surface, indicating that the hole produces a notch effect, which increases the stress beyond the yield stress. Although the data processing of the surface displacements attenuates the effect of the local plastic deformation, the errors are still considerable.

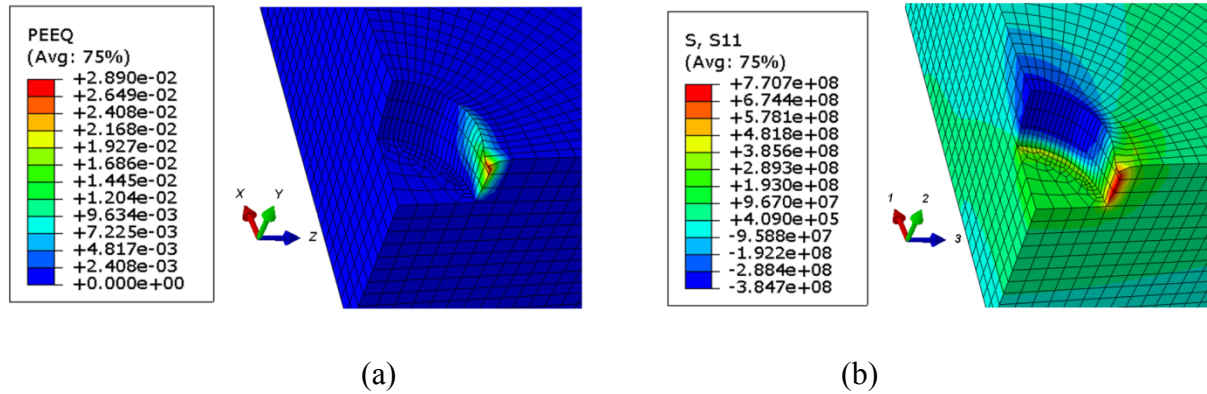


Figure 4.2 a) Abaqus contour plot of equivalent plastic strain distribution for the 3D solid FEM model, b) Abaqus contour plot of σ_x stress component.

4.2 Application of the methodology to LSP-shaped stress profiles

After the experimental validation of the finite element model on the three-point bending test, the LSP-shaped stress profiles with different gradients were simulated. According to the LSP-induced equibiaxial residual stress state, the axisymmetric model presented in Figure 3.11 was used for the simulation of the hole drilling method with elastic-plastic material behavior and the re-identification of the residual stress profile. The maximal hole depth was 0.5 mm

Similar to the curves presented in Figure 4.1a), the predefined stress profiles (dashed lines) along with their returned stress curves from the Integral method (solid lines) are plotted in Figure 4.3a) for the chosen LSP-shaped profiles [159, 160]. The SF range in the mentioned literature is between 0.2 and 1.0. In the current study, the SF value lies in the range of 0.25–0.9, which is comparable to what is given in the literature.

It can be concluded from the results presented in Figure 4.3a) that returned stress profiles are significantly overestimated when residual stress values approach the yield strength of the material. Blue curves correspond to a stress profile with a low stress factor of approximately 0.25. As expected, such a low stress level does not cause any plastic deformations in the material; thus, the material behaves in a fully elastic manner and both curves match very well.

The red curves present a higher LSP stress with a stress factor of approximately 0.7. Inspection of the plot reveals a discrepancy between the curves up to 50% for depths than larger 0.3 mm. As mentioned before, these deviations can be partially caused by the enhanced sensitivity of the Integral method when the hole depth is increased. In addition to the overestimated peak stress, the profiles appear to be shifted towards a larger depth. Concerning the peak value, the shift is from 0.15 mm to 0.23 mm for SF = 0.9.

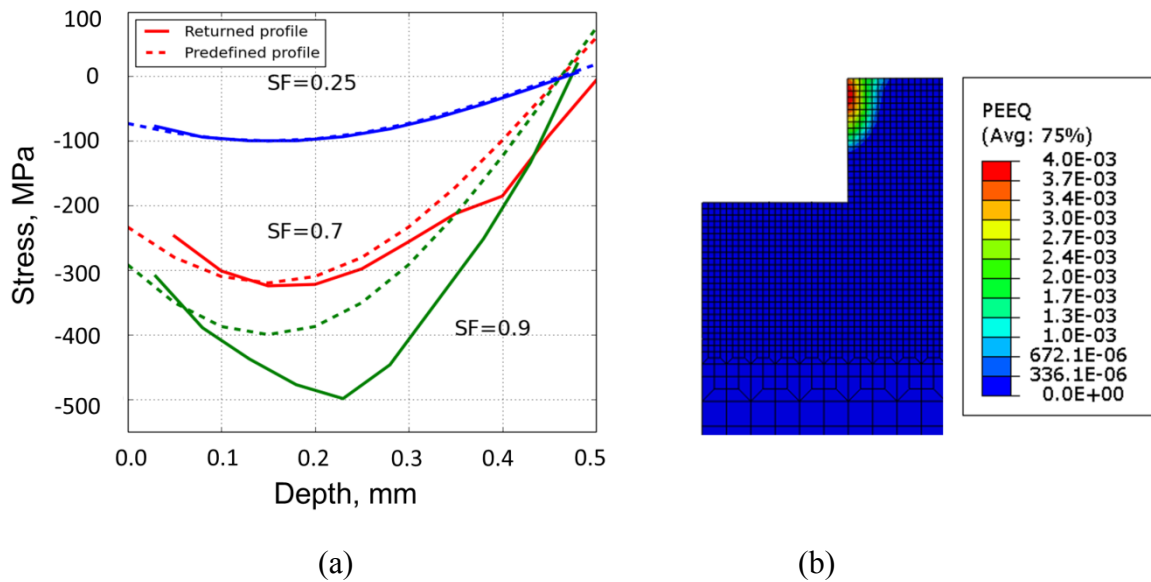


Figure 4.3 Re-identification of residual stress profiles and local plastic deformation typical for LSP-treated samples, a) simulated LSP-shape residual stress profiles, b) ABAQUS contour plot of equivalent plastic strain distribution.

Finally, the green lines demonstrate the identification error resulting in high stress, with a stress factor of approximately 0.9, causing significant plastic transformation in the material. At a depth of 0.2–0.3 mm, the relative error goes up to 32%, which is approximately 120 MPa in absolute value. The returned stress distributions become progressively overestimated when approaching the yield strength.

The contour plot of the equivalent plastic strain distribution is shown in Figure 4.3b), corresponding to the highest stress factor of 0.9. Similar to the previously described case of the three-point bending, plastic deformation affects the region around the hole, leading to nonlinear deformations at the top surface of the sample. As a result, the elastic-plastic material behavior causes an increased in-plane surface deformation, which is wrongly interpreted by the Integral method as an effect of elastic deformations, hence leading to an overestimated sub-surface residual stress. Because the effect is present for all angular positions around the hole in the same magnitude, it cannot be reduced through data processing; thus, the observed error is even larger compared to the uniaxial stress case.

4.3 Solution of inverse problem of stress correction using artificial neural networks

When the direct problem of stress error determination for given material properties and given stress profiles is solved, the inverse problem of the measured stress profile correction can be challenged. As the first step, the wide range of material behaviors and shapes of predefined stress

profiles are simulated and for each simulation (pattern), the stress error is calculated. Afterwards, the ANN (see Chapter 3.2.3) is employed in order to learn the complex relationship between predefined stresses and the given material parameters on the one hand and stress error on the other hand. The learning process is referred to as the training of neural network on simulation patterns. After the neural network is trained, it can be applied inversely for the determination of correct stress profiles from measured stress profiles. In this chapter the stress correction procedure is described in details. The performance of the neural network is tested in regard to the LSP-shaped stress profiles. Moreover, the capability of neural network is tested on “noise” stress profiles which are typically uncounted by measuring with the hole drilling. The chapter ends with the correction of LSP generated stresses measured by hole drilling.

4.3.1 Identification of residual stress profile

4.3.1.1 Neural network generation

The identification of the correct residual stress profile from measured data requires the solution of a complex inverse problem by including prior knowledge about the elastic-plastic material behavior. The flowchart for the approach of this work is illustrated in Figure 4.4. In the first step, patterns are generated by solving the direct problem using the FE method and Integral method, by simulating the hole drilling experiment and residual stress measurement for varying materials and residual stress profiles. The resulting patterns — consisting of pairs of “measured” residual stress profiles from the Integral method and predefined residual stress profiles — form the training basis for the ANN. The known material behavior serves as additional input which is needed for determining the amount of correction. Once the ANN has been trained in the second step for approximation of the general relationship between the presented patterns, it can be applied for the correction of residual stress profiles that were not used for training, such as data from experiments.

For the generation of training patterns, the axisymmetric FE model for the simulation of equibiaxial stress profiles was used. For each new pattern, material parameters and residual stress profiles were randomly chosen within the predefined intervals to produce a sufficient number of independent training patterns, covering mainly the relevant region where the effects of plastic deformation are expected to become important.

The maximal hole depth was 1 mm. A compressive non-linear residual stress profile was expressed as a trigonometric function that sufficiently describes the typical shapes introduced by LSP [3]. The subroutine *DLoad* was used in ABAQUS for applying such residual stresses using the equation

$$\sigma_{PD}(h) = \sigma_0(k_0 - \sin(k_1\pi(h - h_0))) \quad (4.1)$$

4.3 Solution of inverse problem of stress correction using artificial neural networks

where $\sigma_{PD}(h)$ is the predefined compressive stress at the depth of h in the material, while k_0 and h_0 shift the stress profile on the stress axis and depth, respectively. The parameters σ_0 and k_1 are used for scaling the stress profile along the stress axis and the depth respectively. Limiting values of profile coefficients included in Equation (4.1) and material properties are listed in Table 4.1, where σ_{yield} is the yield strength, E is the Young's modulus, and $\sigma_{10\%}$ is the true stress at a true plastic strain of 10%. The condition $\sigma_{10\%} > \sigma_{yield}$ is met for all materials. With these limits, a wide range of materials and residual stress profiles is covered, which may occur in technical applications such as the life extension of aircraft components.

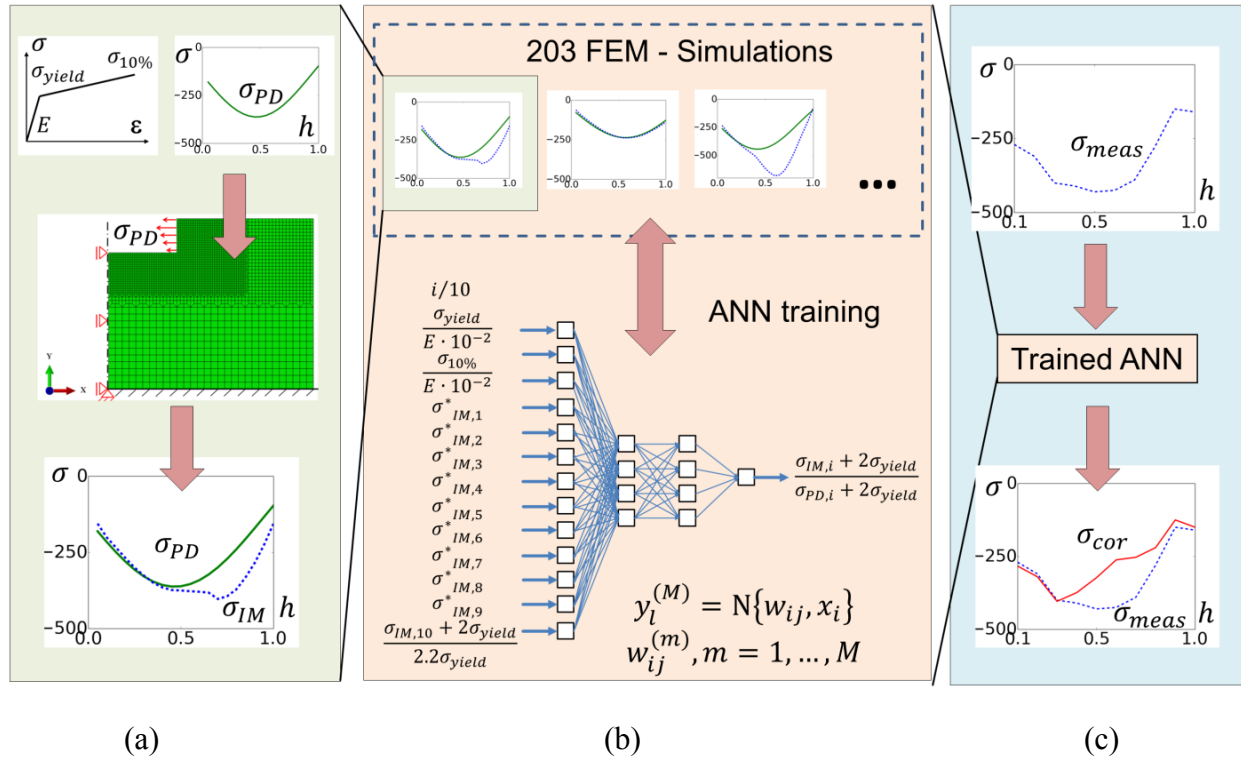


Figure 4.4 Flowchart of ANN application a) pattern generation using FE simulations; b) training of the ANN; c) application of the ANN to experimental data.

A consistent presentation of the patterns for training and eventual application of the ANN requires the introduction of definitions that serve to translate the relevant data into the input vector \vec{X} and output vector \vec{Y} (see Figure 4.4). An appropriate choice of input and output definitions supports the capability of the ANN for improved generalization and higher accuracy. For details about the application of dimensional analysis and the incorporation of prior knowledge, see the cited literature [151–157]. Generally, there are many possibilities of combining the different independent and dependent quantities in linear independent dimensionless quantities, which are again included in the input and output definitions. The number of them needed depends on the complexity of the problem and the robustness of the

inverse solution with respect to scatter. Generally, a lower number of inputs reduces the complexity of the ANN and enhances the generalization, while a higher number of inputs can help to improve the robustness. The latter results from the circumstance, that adding inputs of the same type (e.g. a larger number of stress values over depth) helps the ANN to identify the general trend, independent of the individual scatter of the data points. The final input and output definitions of a properly working ANN are typically the result of an extensive study that compares different possibilities in view of the desired performance.

Table 4.1 Minimum and maximum values for profile coefficients and material properties used for generation of training and validation patterns.

	σ_0 , MPa	k_0	k_1 , mm^{-1}	h_0 , mm	σ_{yield} , MPa	$\sigma_{10\%}$, MPa	E , GPa
Min	150	-0.3	0.7	-0.2	300	400	70
Max	360	-0.9	1.3	0.2	500	600	210

Note. σ_{yield} is the yield strength, E is the Young's modulus, $\sigma_{10\%}$ is the true stress at a true plastic strain of 10%. Poisson' ratio of $\nu = 0.33$ is assumed.

In the following section, a discretization of the depth of the form $h(i)/h_{ref} = i/10$ is applied, where the reference depth is the maximum depth applied for the hole drilling simulation, $h_{ref} = 1$ mm. The residual stress profile is represented by the respective values obtained at depths $h(1)$ to $h(10)$. The residual stress at the depth of h_{ref} is chosen as the reference and is used for normalization of the residual stress profile up to this depth.

In general, the residual stress profile can include a transition from compression to tensile stress. It is convenient to shift the stress profile by adding twice the value of the yield stress. This ensures that all stress values are sufficiently positive and avoids division by zero or by very small stress values during normalization. As the resulting dimensionless quantity, the shifted and normalized residual stresses are defined as

$$\sigma_{IM,i}^* = \frac{\sigma_{IM,i} + 2\sigma_{yield}}{\sigma_{IM,10} + 2\sigma_{yield}} \quad (4.2)$$

$$\sigma_{PD,i}^* = \frac{\sigma_{PD,i} + 2\sigma_{yield}}{\sigma_{PD,10} + 2\sigma_{yield}} \quad (4.3)$$

where $\sigma_{IM,i}$ is the residual stress obtained by applying the Integral method (IM) to simulation data, i.e. without the correction of the effects of plastic deformation, at a depth of $h(i)$. The

predefined (PD) residual stress profile, which was used as the input to the FEM simulation, is translated to the dimensionless quantity $\sigma_{PD,i}^*$ in the same way as $\sigma_{IM,i}^*$, according to Equation (4.3). The values $\sigma_{PD,i}^*$ represent the desired stress profile, to which the values $\sigma_{IM,i}^*$ shall be corrected by the ANN.

For the creation of input and output definitions, elastic and plastic material properties (Young's modulus, E , yield stress, σ_{yield} , and stress at plastic strain of 10%, $\sigma_{10\%}$) and the residual stress profiles $\sigma_{PD,i}^*$ and $\sigma_{IM,i}^*$ are combined in dimensionless quantities. In addition to the information about the residual stress profile $\sigma_{IM,i}^*$, one more dimensionless quantity is required, which relates the reference value of the residual stress profile, $\sigma_{IM,10}$, to the mechanical properties represented by the yield stress, e.g. in the form $(\sigma_{IM,10} + 2\sigma_{yield})/(2.2\sigma_{yield})$. The factor of 2.2 in the denominator is derived from the range of the patterns and scales this input to the order of 1.

The material parameters — Young's modulus E , yield stress σ_{yield} , and stress at plastic strain of 10% $\sigma_{10\%}$ — are combined into two further dimensionless quantities. For better comparison of the different inputs, here the division of the Young's modulus by a factor of 100 also brings the order of the input quantities to a similar level. Such scaling has no further effect on the performance of the ANN but can help to visually check the large number of patterns in regard to correct data processing. As a final input, the depth at which the correction factor for the residual stress shall be determined is given. Based on these considerations, the following input (\vec{X}) and output (\vec{Y}) definitions are defined:

$$\vec{X} := \left\{ \sigma_{IM,1}^*, \sigma_{IM,2}^*, \dots, \sigma_{IM,9}^*, \frac{\sigma_{IM,10} + 2\sigma_{yield}}{2.2\sigma_{yield}}, \frac{\sigma_{yield}}{E \cdot 10^{-2}}, \frac{\sigma_{10\%}}{E \cdot 10^{-2}}, \frac{i}{10} \right\} \quad (4.4)$$

$$\vec{Y} := \left\{ \frac{\sigma_{IM,i} + 2\sigma_{yield}}{\sigma_{PD,i} + 2\sigma_{yield}} \right\} \quad (4.5)$$

The scaling of the output using the results of the Integral method in the form of Equation (4.5) reduces the range of the output \mathbf{Y} to an interval $[0.8, 1.02]$ for all patterns, i.e. independent of material properties and residual stress magnitude (see Figure 4.6). In other words, the prior knowledge of the Integral method is fully incorporated in the neural network by this form of scaling and the task of the neural network is limited to correct possible deviations caused by the effects of plasticity. As a result, this significantly improves the accuracy of the neural network compared to the case where the neural network is trained to directly determine the predefined residual stress $\sigma_{PD,i}$ as an absolute value.

After the training of the ANN to patterns consisting of pairs (\vec{X}, \vec{Y}) , the neural network finally approximates the function

$$\left(\frac{\sigma_{IM,i} + 2\sigma_{yield}}{\sigma_{PD,i} + 2\sigma_{yield}} \right) = f \left(\sigma_{IM,1}^*, \dots, \sigma_{IM,9}^*, \frac{\sigma_{IM,10} + 2\sigma_{yield}}{2.2\sigma_{yield}}, \frac{\sigma_{yield}}{E \cdot 10^{-2}}, \frac{\sigma_{10\%}}{E \cdot 10^{-2}}, \frac{i}{10} \right) \quad (4.6)$$

For obtaining the corrected residual stress, the ratio $\frac{\sigma_{IM,i} + 2\sigma_{yield}}{\sigma_{PD,i} + 2\sigma_{yield}}$ obtained from the ANN is solved with respect to the absolute values $\sigma_{PD,i}$, which represent the predefined — but in the application unknown — residual stress profile in the specimen. Because the trained ANN is able to interpolate between presented patterns, the output definition in the application of the ANN is not restricted to the depth increments used for training. This means that the last input parameter in Equation (4.4), which is $i/10$, can be generalized to a variable h/h_{max} , continuously scanning the depth range between 0.1 mm and 1 mm.

The structure of ANN is defined by 13 input neurons and two hidden layers — each consisting of four neurons — and one output neuron. It has been trained with 2,030 patterns for 5,000 epochs without any sign of overlearning. The training patterns were built from 203 FEM simulations, in which every set of 10 patterns had 12 identical input neurons and only the 13th input, which represents the depth h , varied within these 10 patterns from 0.1 to 1.0. The structure of the neural network is shown in Figure 4.5.

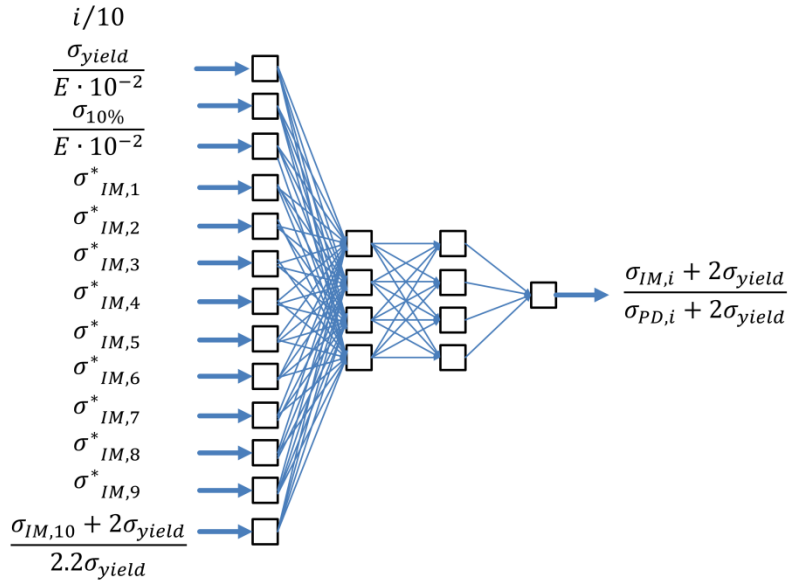


Figure 4.5 Structure of the neural network for correcting the plasticity effect in the inverse determination of residual stress profiles.

4.3.1.2 Identification quality of the neural network

The best generalization was achieved by training with $\kappa = 6.0$, balancing the absolute value of the synaptic weights in relation to the training error and thus avoiding overlearning (see Equation (3.15)). Out of 2,030 patterns, 1,827 were used as training patterns and 203 were randomly

selected for validation from within the training range, i.e. none of the validation patterns belonged to the boundary enclosing the patterns. Corresponding to Equations (3.16) and (3.17), comparable mean error values of $MSE_T = 2.2 \cdot 10^{-5}$ and $MSE_V = 2.5 \cdot 10^{-5}$ were from training and validation, respectively. Very low relative errors within a 90% confidence interval of $err_Y^T = 1.57\%$ and $err_Y^V = 1.58\%$ were achieved for training and validation patterns, respectively. The resulting quality after training of the ANN with over 5,000 epochs is presented in Figure 4.6. In addition to the given error measures, it illustrates that the ANN can predict the data for untrained patterns with the same quality as the training patterns, indicating a high level of generalization.

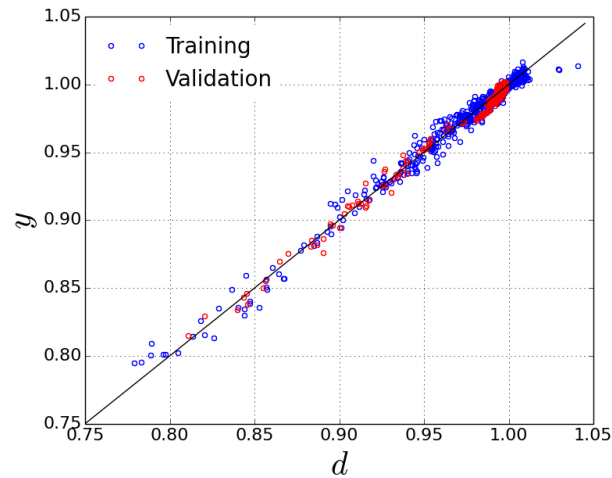


Figure 4.6 Identification quality of the neural network, presented by calculated output y vs. desired output d according to the definition in Equation (3.15).

4.3.1.3 Verification of the correction method for AA2024-T3

For further inspection of the performance of the neural network, four randomly chosen residual stress profiles have been simulated with the material parameters for AA2024. The parameters serve to test the trained neural network by using patterns that were not involved in the training process. This additional verification basically implements a procedure similar to the validation patterns during learning. However, now its capability is tested in regard to the absolute values obtained for the corrected residual stress profile. The nonlinear work hardening of AA2024 is approximated with a linear segment, as shown in Figure 3.13, in accordance to the definition in training patterns. In order to check for a possible sensitivity of the ANN in regard to this simplification, both the nonlinear stress-plastic strain curve and its linear approximation were tested. The excellent agreement between the two corrected profiles confirmed that the proposed linear approximation sufficiently describes the elastic plastic material behavior.

The validation examples for an increasing ratio of residual stress to yield strength $\sigma_{PD,max}/\sigma_{yield}$ are shown in Figure 4.7a)-e). The predefined residual stress profiles applied in the hole drilling

simulations (green solid curve), the data obtained from the Integral method (blue dashed curve), and the corrected profiles obtained through the neural network (red circles) are displayed. In Table 2.1, the maximum ($\Delta\sigma_{max}$) and mean absolute errors ($\Delta\sigma_{avg}$) are summarized for simulated (Integral method) and ANN-corrected residual stress profiles in relation to the predefined ones. The coefficients of the predefined residual stress profiles according to Equation (4.1) are listed in Table 4.2 as well.

The compressive stress profile shown in Figure 4.7a) with a maximum of 60% of the yield strength (here approximately at a depth of 0.6 mm) does not require a correction, confirming the conventional validity limit of the Integral method also for the LSP profile. The mean absolute errors for both simulated and corrected profiles are within the deviation range of the Integral method, but even in this case, the ANN further reduces the error by more than half. In the case of negligible effect of plastic deformation, the neural network is trained to deliver a correction factor of 1.0; i.e. the neural network can be applied to any measurement data, even if a correction is not required.

The simulated stress curves in Figure 4.7b) – e) demonstrate the growing deviations between the predefined and simulated profiles with an increasing ratio of residual stresses versus yield strength. It can be concluded that the effect of plasticity is strongly dependent on the combination of the shape of the predefined stresses and the depth where the peak values occur. The simple assumption about the applicability of the hole drilling for the measurement of residual stresses not exceeding 60% of the yield strength — as found in literature [21, 27] — should be improved by considering the shape of the stress profile as well.

The correction by the neural network leads to a strong reduction of the error resulting from the Integral method. In all cases, the mean absolute errors do not exceed 10 MPa, showing the ability of the neural network for also correcting “unseen” patterns with the same accuracy as achieved for the training patterns. The corrected stress values are close to the predefined stresses along the whole depth and without any specific bias. The remaining deviations are due to the approximate nature of the neural network.

The stress profile shown in Figure 4.7e) is doubtfully achievable by means of LSP for AA2024, but can give an impression about the possible deviation in stress determination; it demonstrates the inapplicability of hole drilling without correction in such cases. In this case, the neural network reduces the maximum deviation from 306 MPa to 21 MPa, thereby making the maximum deviation comparable to an error practically accumulated from the other sources of inaccuracy of the hole drilling measurement.

4.3 Solution of inverse problem of stress correction using artificial neural networks

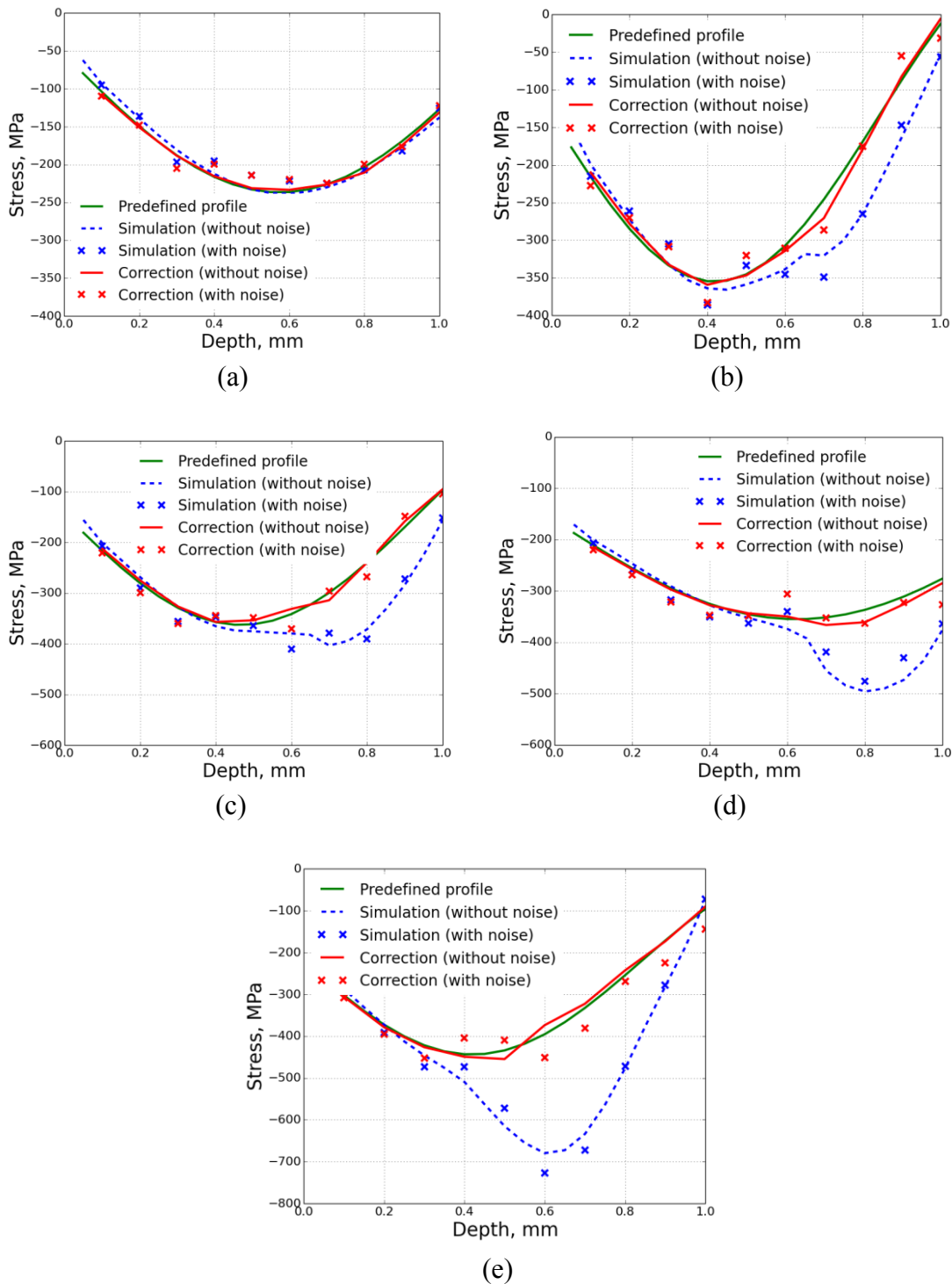


Figure 4.7 Validation samples for prediction of predefined stress profiles by neural network for increasing ratio of maximum residual stress to the yield strength a) $\sigma_{PD,max}/\sigma_{yield} = 60\%$, b) $\sigma_{PD,max}/\sigma_{yield} = 92\%$, c) $\sigma_{PD,max}/\sigma_{yield} = 95\%$, d) $\sigma_{PD,max}/\sigma_{yield} = 95\%$ e) $\sigma_{PD,max}/\sigma_{yield} = 116\%$.

Table 4.2 Predefined stress profiles and errors of simulated (Integral method) and ANN corrected stress profiles in relation to the predefined stress profiles.

	Predefined profile					Simulation (Integral method)	Correction (ANN)		
	σ_0 , MPa	k_0	k_1 , mm^{-1}	h_0 , mm	$\frac{\sigma_{PD,max}}{\sigma_{yield}}$, %	$\Delta\sigma_{max}$, MPa	$\Delta\sigma_{avg}$, MPa	$\Delta\sigma_{max}$, MPa	$\Delta\sigma_{avg}$, MPa
(a)	182.2	-0.30	0.87	-0.08	60	17.2	6.6	7.3	2.9
(b)	219.2	-0.62	1.19	0.06	92	96.0	37.0	25.0	7.4
(c)	218.4	-0.66	1.07	0.03	95	131.5	49.2	14.7	5.8
(d)	192.0	-0.85	0.82	0.02	95	164.8	55.4	21.5	10.0
(e)	223.1	-0.88	1.19	-0.03	116	306.0	123.2	20.8	8.0

In conclusion, it can be stated that the proposed choice of the dimensionless quantities for inputs and outputs satisfactorily fulfils the given objectives. Since the neural network is trained by patterns covering a large range of materials and residual stress distributions, it is designed to be applicable to a large range of experimental data. For the application of the neural network, only a few material properties $\sigma_{yield}, \sigma_{10\%}, E$ have to be known. Based on these properties, the measured stress profiles can be effectively corrected, as demonstrated in Figure 4.7a)–e). In case of pure elastic deformations, the neural network keeps the measured profile within the accuracy of the Integral method. Therefore, the method is applicable even without prior knowledge of plasticity occurrence.

4.3.2 Sensitivity of the neural networks to noise

The previous section leads to the conclusion that the ANN can be used for the correction of measured residual stress profiles with an accuracy that is comparable to the Integral method, when the input data are provided by simulations and can be considered to be exact. However, every experiment includes measurement uncertainties and scatter; finite element simulations have uncertainties relating to the capturing of all relevant effects of the experiment, such as the boundary conditions or large displacement formulation.

4.3 Solution of inverse problem of stress correction using artificial neural networks

Generally — and particularly when solving inverse problems — ANNs that are trained by accurate model data can be very sensitive to scatter, as they potentially have successfully learned to interpret highly accurate signals from the different inputs. Such ANNs can predict meaningless results for experimental data, where scatter is interpreted as a real effect and is translated with the corresponding magnification to the output.

For this reason, all finite element simulations from the previous section were used to generate new patterns, where random noise $\Delta\sigma_{IM}$ — varying between -10% and 10% of the original data with equal probability — was artificially added to the simulated stress values σ_{IM} . An ANN with the same structure as well as the same input and output definitions as described in the previous section has been trained by these patterns. The achieved accuracy after training with 5,000 epochs is as follows: the mean error values for training and validation are $MSE_T = 1.1 \cdot 10^{-4}$ and $MSE_V = 1.6 \cdot 10^{-4}$; the absolute relative error values within 90% confidence intervals are $err_Y^T = 3.48\%$ and $err_Y^V = 3.90\%$. The presence of 10% artificial noise in the predefined patterns has increased training and validation errors approximately by a factor of 3. This means that the performance of the neural network is reduced by uncertainties, but it is still capable of fulfilling its task with an accuracy better than 5% for more than 90% of the patterns.

4.3.2.1 Verification of the correction method for AA2024-T3 and “noisy” residual stress profiles

In order to demonstrate the robustness of the network, the same validation cases were chosen as described in Table 4.2, but now an artificial scatter was added to the values $\sigma_{IM,i}$, as described for the training patterns. The residual stress values $\sigma_{IM,i} + \Delta\sigma_{IM}$ used for the ANN input are included in Figure 4.7 as markers (blue cross), scattering around the blue dashed curve. The results of the ANN correction are added in Figure 4.7a)–e) (red cross markers). They demonstrate an overall good correction of the “noisy” stress profiles, implying that the ANN is able to extract the relevant information from the redundant input data providing the information about the residual stress profile. However, the applied noise is transferred to the corrected profile through the normalization of the neural network output, according to Equation (4.5). Thus, the corrected stress values also scatter around the predefined stresses, but without any bias, so one can apply an interpolation technique to obtain the smooth corrected curve.

The errors of simulated and corrected stress profiles are presented in Table 4.3, together with the errors from the previous section (without artificial scatter). By applying the ANN to the “noisy” residual stress profiles, both maximum ($\Delta\sigma_{max}$) and mean absolute errors ($\Delta\sigma_{avg}$) of the corrected profiles are increased by the factor of 1.5–4.0, which is of same magnitude as the absolute errors err_Y^T and err_Y^V growth for training and validation patterns, respectively. The increase in the correction errors mimics the measurement uncertainties typically encountered by hole drilling. In case of negligible plastic deformations, the ANN still keeps the stress curve unchanged, even though the correction errors remain almost the same due to the introduced

noise, which means that the artificial scatter with the factor of 1.0 is translated into the corrected data (Figure 4.7a)). Also with added scatter, the effect of plasticity is mitigated with an accuracy comparable to the accuracy of the hole drilling method described in the experimental techniques part. From experimental observations [40], this accuracy is approximately 30 MPa.

Table 4.3 Errors of simulated (Integral method) and corrected stress profiles (ANN) with and without additional noise for different predefined residual stress profiles.

	Simulation (IM) without measurement uncertainties		Simulation (IM) with measurement uncertainties		Correction (ANN) without measurement uncertainties		Correction (ANN) with measurement uncertainties	
	$\Delta\sigma_{max}$, MPa	$\Delta\sigma_{avg}$, MPa	$\Delta\sigma_{max}$, MPa	$\Delta\sigma_{avg}$, MPa	$\Delta\sigma_{max}$, MPa	$\Delta\sigma_{avg}$, MPa	$\Delta\sigma_{max}$, MPa	$\Delta\sigma_{avg}$, MPa
(a)	17.2	6.6	21.0	10.5	7.3	2.9	18.9	9.4
(b)	96.0	37.0	103.5	43.7	25.0	7.4	40.8	20.7
(c)	131.5	49.2	150.0	51.4	14.7	5.8	31.1	16.8
(d)	164.8	55.4	139.3	50.2	21.5	10.0	50.9	21.1
(e)	306.0	123.2	339.2	126.5	20.8	8.0	56.1	34.3

4.3.3 Application to measured LSP residual stress fields

In order to observe how the ANNs presented in the previous sections react to real experimental data, both solutions are applied to correct the measured residual stress profiles. LSP has been applied to AA2024-T3 2 mm thin specimens with the material parameters given in the material's section. The residual stress profiles, shown in Figure 4.8a)–c), were achieved using the LSP parameter sets given in Table 4.4.

The laser pulse duration of 20 ns was used in all experiments. When the 3mm optics were used, the peened square area was 15 mm by 15 mm, which was covered by 25 laser pulses. For the 1mm optics, the treated area was 5 mm by 5 mm, covered by 25 laser pulses. As shown in Figure 4.8a)–c), deeper compressive residual stresses were induced by using 1mm optics and large amount of overlap and the maximum value of compressive stress is also increased. Every parameter set was replicated three times in order to increase the process reliability. The holes were incrementally drilled at the center of the treated area using a drill diameter of 2 mm up to a maximum depth of 1 mm, i.e. half the thickness of the specimens. The three obtained residual stress profiles for each LSP parameter set were averaged before correction.

Table 4.4 LSP parameters and the errors of measured stresses in relation to corrected stresses by ANN

	Measured (Integral method) without uncertainties		LSP parameters		
	$\Delta\sigma_{max}$, MPa	$\Delta\sigma_{avg}$, MPa	Pulse energy, J	Optic system	Overlap, number of shots
(a)	13.4	7.7	5	3 mm	2
(b)	85.2	30.1	5	1 mm	2
(c)	163.3	56.9	5	1 mm	5

The averaged stresses and the material properties were used to feed the trained neural network for the correction of potential plasticity effects. Two cases were investigated. In the first case, the stress profiles were assumed to be “ideally” measured and the neural network trained without additional noise was used. In the second case, the same stress profiles were assumed to be measured with uncertainties; therefore, the neural network trained with additional scatter was applied. For each residual stress profile, the dimensionless input quantities were calculated according to the input definition given in Equation (4.5). Afterwards, the neural networks were used to provide the correction factor for the residual stress as a function of depth h . The results are illustrated in Figure 4.8a)–c). From the comparison of the results for both ANNs, it can be seen that the ANN trained without artificial scatter is similarly robust when applied to experimental data, thanks to the redundant input of the residual stress profile in the form of nine $\sigma_{IM,i}^*$ values.

In Figure 4.8a), the measured stress values are lower than 60% of the yield strength. As expected, no corrections were needed in this case and the ANN with and without measured uncertainties reproduced the original profile. The mean absolute error of 7.7 MPa is within the tolerance of the Integral method.

In Figure 4.8b)–c), the stress profiles were corrected towards the lower compressive values, which indicates the presence of plastic deformation, causing the stresses to be overestimated. It should be noted that the subsurface values in the depth interval of 0.1–0.3 mm were not corrected by the neural network at all. This is analogous to the training patterns. It can be seen that as the measured stresses approach or even overcome the yield strength, the larger the corrections have to be, leading to an increase in the mean absolute errors. The maximum corrections of 85.2 MPa and 163.3 MPa — Illustrated in Figure 4.8b) and (c) respectively — are applied at the depth range 0.6–0.7 mm, where the maximum values of the measured stress profiles are located. Therefore, the correction is essential to the residual stresses of such a magnitude.

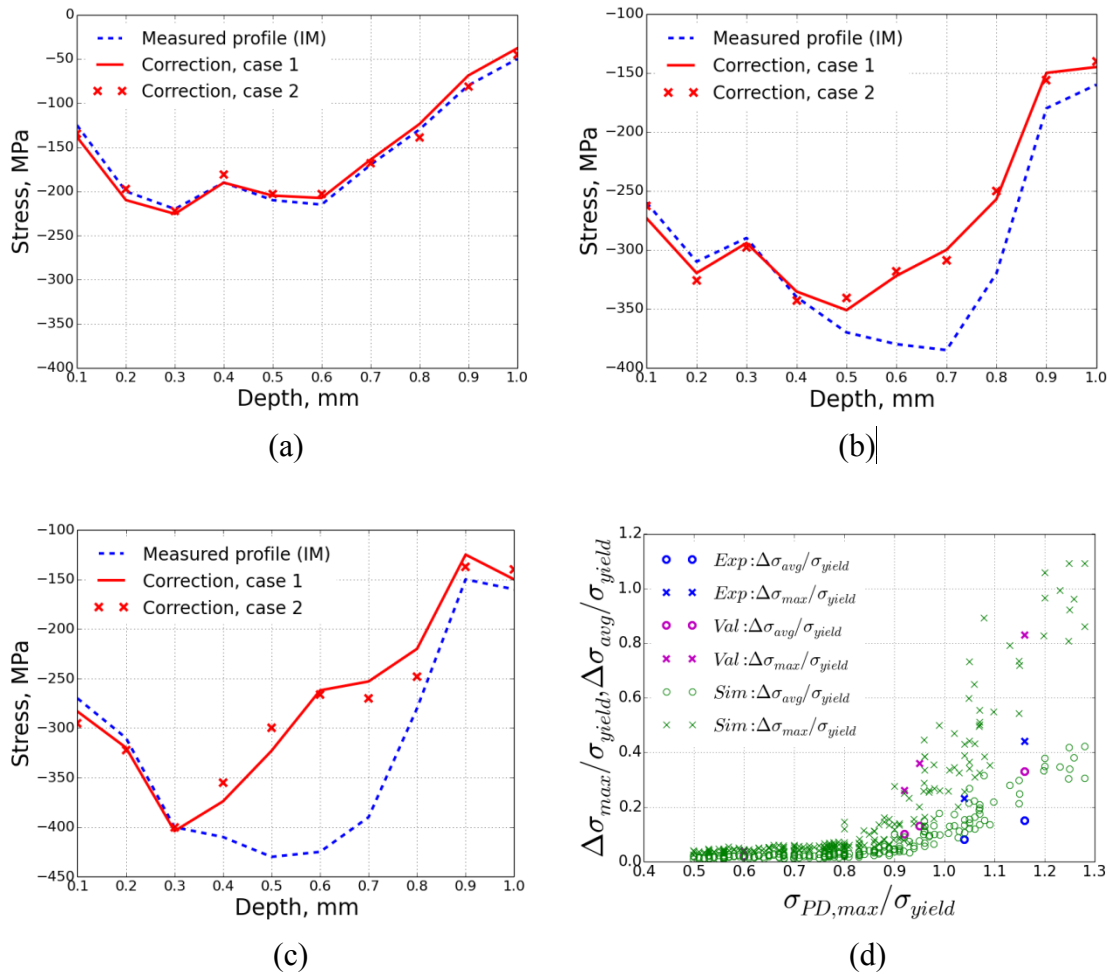


Figure 4.8 Correction of LSP-induced stress profiles by the neural network a) $\sigma_{cor,max}/\sigma_{yield} = 60\%$, b) $\sigma_{cor,max}/\sigma_{yield} = 104\%$, c) $\sigma_{cor,max}/\sigma_{yield} = 116\%$; d) normalized maximum error ($\Delta\sigma_{max}/\sigma_{yield}$) and mean absolute error ($\Delta\sigma_{avg}/\sigma_{yield}$) versus the stress factor ($\sigma_{PD,max}/\sigma_{yield}$) for all FE patterns (green, purple) and measured LSP residual stress profiles.

In Figure 4.8d), the normalized maximum errors ($\Delta\sigma_{max}/\sigma_{yield}$) and mean absolute errors ($\Delta\sigma_{avg}/\sigma_{yield}$) are plotted against the stress factor $\sigma_{PD,max}/\sigma_{yield}$ for all training and validation patterns as well as for the corrected LSP residual stress profiles. One can see that the normalized errors are less than 8% as long as the stress factor is $\sigma_{PD,max}/\sigma_{yield} \leq 0.8$. Therefore, our analysis reveals, that — in extension of the commonly assumed 60% limit — the hole drilling method can be reliably used for measuring the LSP-shaped residual stress profiles up to 80% of the yield strength. Beyond this value, the error grows progressively and reaches maximum values of 43% and 110% for $\Delta\sigma_{avg}/\sigma_{yield}$ and $\Delta\sigma_{max}/\sigma_{yield}$, respectively, at $\sigma_{PD,max}/\sigma_{yield}$ of approximately 1.3. The errors' scatter reflects the amount of correction that depends on the shape of the residual stress profile. The increasing width of the scatter band shows that the relevance of

the profile shape gains in importance with increasing stress level $\sigma_{PD,max}/\sigma_{yield}$. Concerning the experimental stress profiles, as presented in Figure 4.8b)–c), it can be seen that they are located at the lower boundary of the scatter bands in Figure 4.8d) (blue symbols). This confirms that the experimental LSP profiles analyzed in this work are well within the range of residual stress profiles covered by the ANN.

4.4 Conclusions

The Integral method has been enriched through an elastic-plastic finite element model of the given specimen geometry in order to solve the inverse problem of residual stress determination from surface relaxations. The parameter ranges in the simulation are selected to cover the relevant range of material behaviors and LSP-shaped residual stress profiles of typical experimental applications. An artificial neural network (ANN) was used to identify the relationship between predefined (“actual”) and simulated stress profiles (plastically affected data obtained from the Integral method), by training with more than 2,000 patterns built from the simulation data. The main advantage of usage of an ANN is its generalization capability — i.e. the ability of a trained network to predict appropriate output data for unlearned data. The trained neural network has shown a degree of accuracy comparable to the conventional Integral method in the valid application range, even when artificial noise is present.

For the validation of the finite element model, the stress profiles with a linear gradient were generated in a AA2024-T3 alloy using a three-point bending flexural testing system and were then measured by hole drilling. The determined stress profiles, with a stress factor below 60% of the yield strength, were similar to the applied stress distributions, supporting the assumption of linearity. When the stress exceeded this level, the error increased significantly up to 21% at 80% of the yield strength. It was found that the dependency on the depth of the hole has an effect on the transition from elastic to elastic-plastic deformation around the hole at a stress factor of 50%. The effect of plastic deformation results from the notch effect of the hole. Although the nominal stress is well below the yield strength of the material, the notch increases the near-surface stress above the yield strength. This causes plastic deformation in the direction of the hole center, which is interpreted by the Integral method as originating from the “nominal” residual stress profile. The result is a significant overestimation of the residual stress.

Afterwards, laser peening-induced residual stress profiles were corrected by the trained neural network to show the applicability of the method to experimental data. It is revealed that the shape of the residual stress profiles and the depth, where the maximum stress values occur, strongly affect the plastic deformations. Therefore, the common assumption of 60% of the yield strength [21, 27] should be improved by considering these two aspects.

The correction by the neural network significantly reduces the mean absolute errors to 10 MPa, which is comparable with the accuracy of hole drilling. The analysis reveals that for LSP-shaped stress fields the normalized errors are less than 8% as long as stress magnitude does not exceed, which extends the commonly assumed 60% limit. However, when 80% of the yield strength is exceeded, the normalized errors $\Delta\sigma_{avg}/\sigma_{yield}$ and $\Delta\sigma_{max}/\sigma_{yield}$ grow progressively up to 43% and 110%, respectively. The shape of residual stress profile contributes more to the plasticity effect as the maximum stress value grows beyond the 80% of the yield strength.

5. Optimization of laser shock peening process using design of experiments

After having established the stress correction methodology in Chapter 4, the LSP-induced residual stresses can be reliably measured even when approaching material yield strength. In this chapter, the LSP process itself is optimized in regard to the generated residual stresses, which are desired for enhancement of fatigue and fatigue crack growth behavior, using DOE. The four stages of DOE (planning of experiments, factor screening, factors optimization, and model verification) are discussed in details in the following sections. As a result of the process optimization, the feasible region of the process parameters variation is achieved. Finally, the significant retardation of the fatigue crack growth due to the LSP treatment is experimentally demonstrated on AA2024-T3 C(T)50 specimens.

5.1 DOE: planning stage

The designed 54 experiments of the LSP treatment were conducted randomly in order to exclude the bias in the response variables and a systematic error associated with the specific factor combinations [140, 142]. The generated residual stresses in the specimens were measured by the hole drilling and the responses at the design points were calculated from the measured data. The information about the factor and response variables as well as the run order of the experiments are listed in Table A1. Four out of the 54 treatments were measured inaccurately because of the poor surface reflectivity after LSP and they are marked with “-.” Therefore, the number of actually performed experiments that are considered in further analysis has become 50.

The power study for the factor effects and factor interaction effects for originally planned and performed experiments is presented in Table 5.1. In this work, an acceptable probability level of factor effect detection was defined as 80%. Table 5.1 shows that the experimental design has sufficient determination ability for the main effects and two-way interaction A•B and A•C, while the B•C as well as three-way interaction A•B•C are unlikely to be determined correctly from the planned experiments and should be considered with caution. This is the feature of the general full factorial design, and the low power for the B•C effect is attributed to two levels of the C factor (2mm *optics* is not investigated). Due to the incorrect measurement of 4 treatments, the power for factor effects has dropped slightly, but it still is considered acceptable within the framework.

Table 5.1 Design evaluation: power study

Factor and interaction	Power quantity, 54 planned experiments	Power quantity, 50 performed experiments
A: Optics	0.9754	0.9635
B: Overlap	0.8354	0.7928
C: Energy	0.9048	0.8843
A • B	0.8354	0.7928
A • C	0.9048	0.8843
B • C	0.1	0.1
A • B • C	0.1	0.1

5.2 DOE: factor screening analysis

5.2.1 Response stress at 0.01 mm

The factor screening for the response *stress at 0.01 mm* $S_{0.01}$ is presented in Figure 5.1a). The statistical test shows that all main factor effects A, B, and C and interactions B•C and A•B are significant. In general, three-way interactions rarely occur; as expected here, A•B•C is negligible. The T-value of the interactions A•C, B•C slightly exceeds the critical value, which means that these interactions are not strong; therefore, the main factor effects A, B, C can be considered separately according to their importance. Moreover, B•C may contain determination error due to the structure of design, as shown in the power study. *Optics* and *energy* have no interaction, that would allow a reliable generation of residual stress under the surface by varying these factors (A, C) when the number of *overlaps* is restricted by the process and cannot be changed.

P-values of the regression model are shown in Table 5.2. The low P-values of the significant terms show how strongly the factors affect the response; they are presented in red. The main factors A, B, and C have stronger effects than interactions on the response, as also shown in the statistical test.

Table 5.2 Response stress at 0.01 mm: P-values of the regression model.

Term	P Value
A: Optics	5.80E-12
B: Overlap	4.99E-05
C: Energy	5.12E-06
A • B	0.0346
A • C	0.5459
B • C	0.0225
A • B • C	0.7331

The interaction effects are presented in Figure 5.1b). Factor points are connected with the lines. The lines — which are not parallel — intersect. The intersecting angle indicates how significant an interaction effect between the factors. B•C and A•B interactions seem to have comparable significance, which is in agreement with the statistical test.

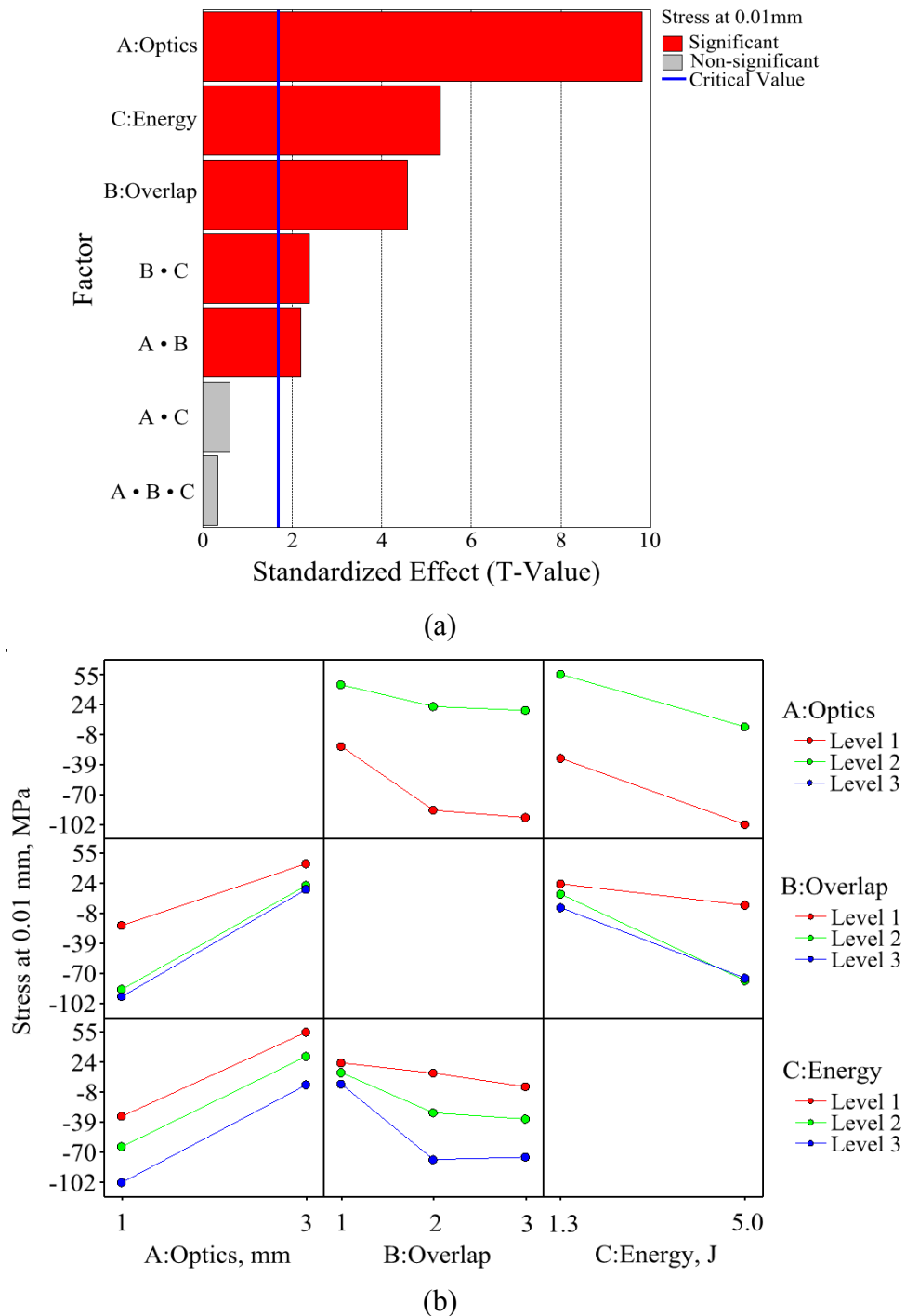


Figure 5.1 Stress at 0.01 mm response: (a) factor screening, (b) factor interaction effects.

The result for R^2 is 81.49% for the regression model of *stress at 0.01 mm* response, which exceeds the acceptance level of 80% defined in this work. The fitted response values versus actual experimental values are presented in Figure 5.2. Most of the data are spread around the diagonal line, demonstrating the acceptable level of model fitting which is in agreement with the R^2 of 81.49%.

The residuals of the regression model are presented in Figure 5.3a). No trend or pattern is seen on the graph. Four observations fall outside of the 10% critical region. They are the outliers and need to be checked for possible measurement errors. The residual stress profiles related to the outliers O_1 and O_2 and their replicates are shown in Figure 5.4a) and b), respectively. The residual stress profiles of the outliers are significantly different from the stress profiles of the replicates. The distinction between the stress profiles is caused by LSP instabilities or measurement error. The other two outliers in Figure 5.3a) are subjected to identical analysis and, after that, all four experimental runs are excluded from the subsequent analysis. The probability distribution of the residuals of the fitted regression model is illustrated in Figure 5.3b). The residuals show a normal distribution, providing good adequacy of the fitting model.

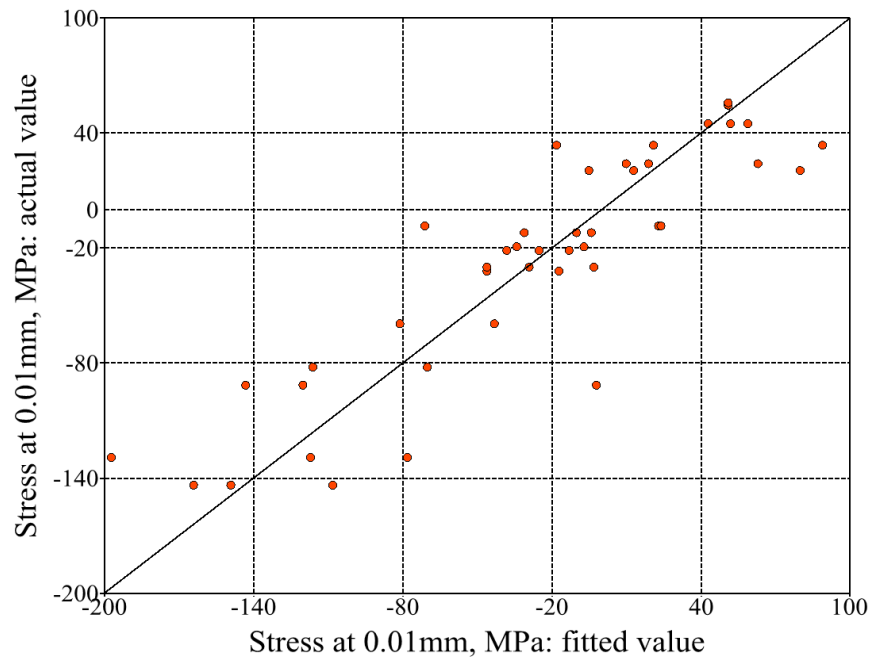
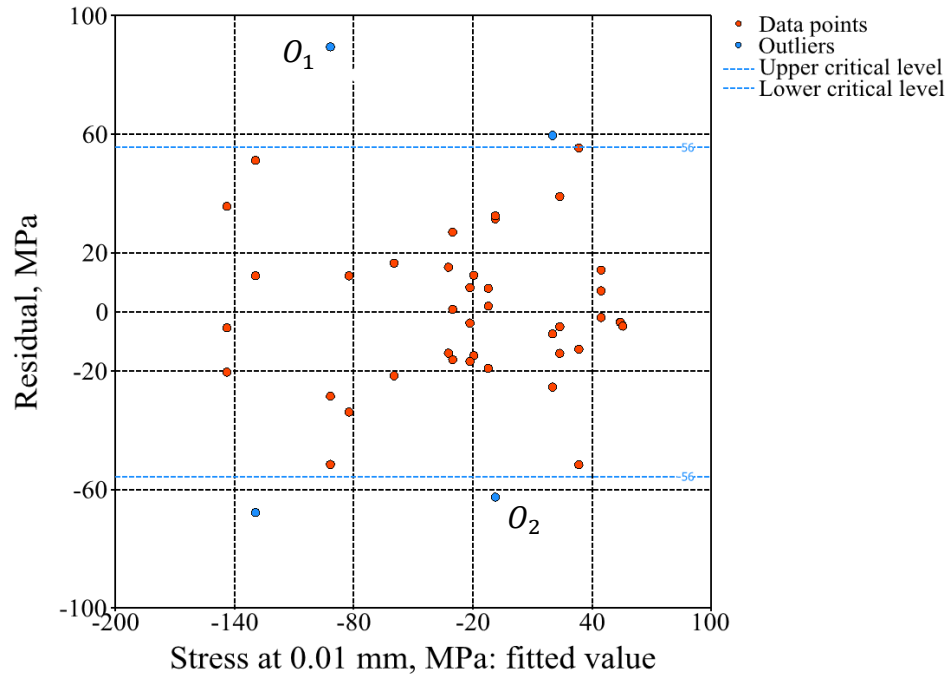
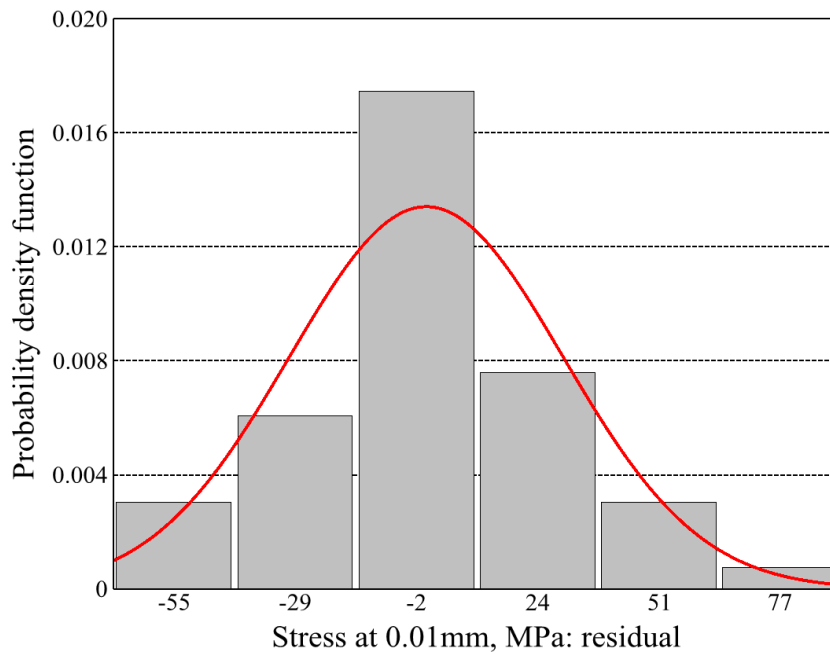


Figure 5.2 *Stress at 0.01 mm* response: identification quality of the fitted regression model.



(a)



(b)

Figure 5.3 *Stress at 0.01 mm* response: (a) analysis of residuals of the fitted regression model, (b) probability distribution of residuals of the fitted regression model.

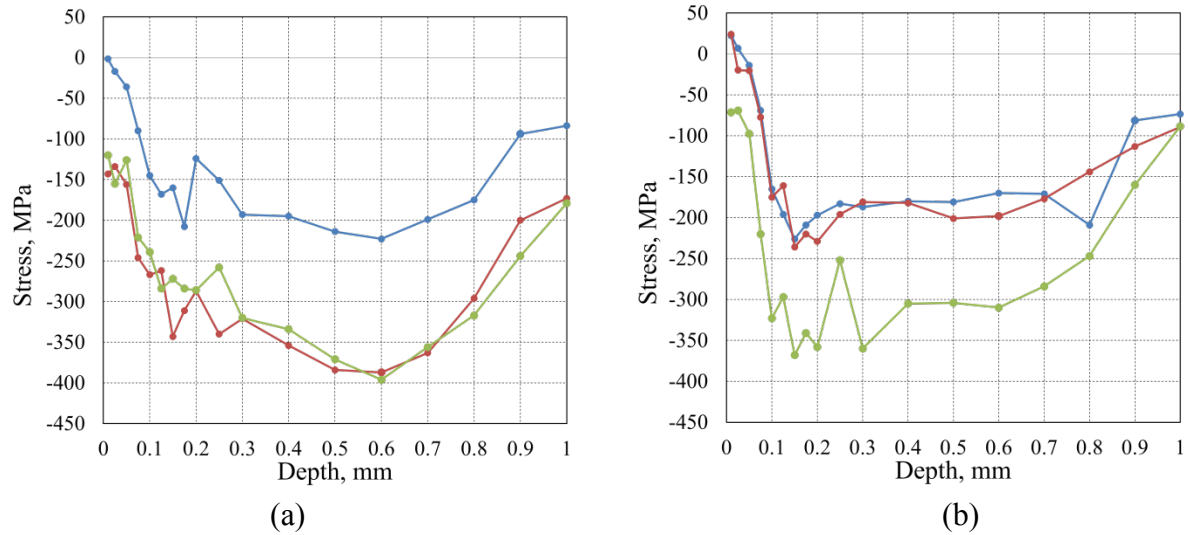


Figure 5.4 Residual stress profiles of three replicates generated using: (a) 1mm optics, 3.0 J energy, 3 overlap (the blue line is an outlier); (b) 1mm optics, 1.3 J energy, 1 overlap (the green line is an outlier).

For the examination of the influence of the *overlap* and *energy* variations on the *stress at 0.01 mm* while keeping the *optics* at 1 mm, the 3D plot is shown in Figure 5.5 [143]. The isolines show the factors variations which correspond to the desired *stress at 0.01 mm* value. So, one can set the factors levels according to the available laser pulse energy in order to achieve the desired *stress at 0.01 mm*. The response surface values are symmetric relatively to the vertical plane passing through the maximum and minimum response values on the graph. This means that both *overlap* and *energy* have almost equal significant effects and little interaction effect on *stress at 0.01 mm*, as also inferred in the statistical test. *Stress at 0.01 mm* decreases by increasing either *overlap* or *energy* and reaches its minimum when the factors are at their maximum values and vice versa. What follows is that the *Stress at 0.01 mm* can reach high compressive stress values by increasing the number of *overlap*, when operating with relatively low *energy*. Thereby, the laser price, which is defined by the laser power, can be decreased; however, the processing time is increased.

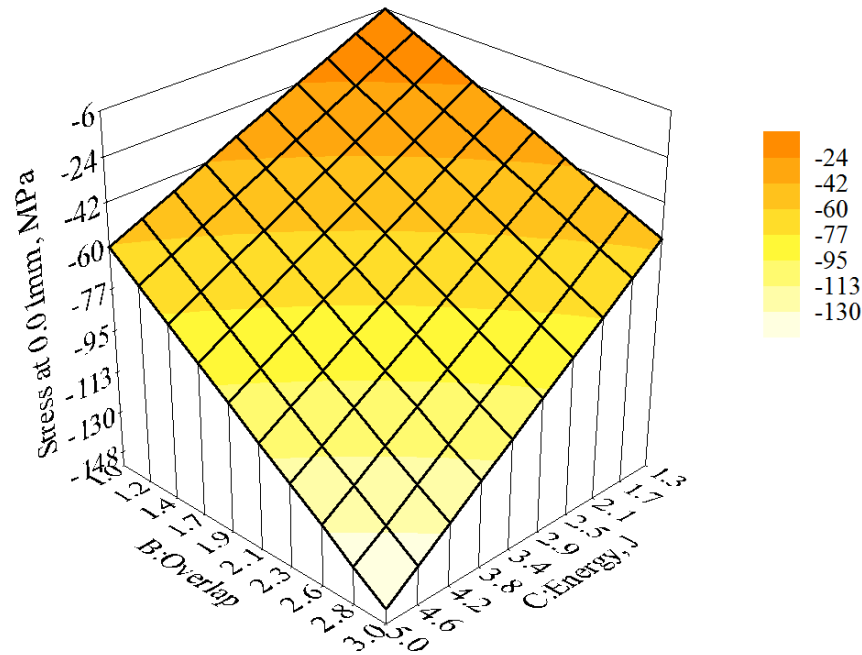


Figure 5.5 *Stress at 0.01 mm* response as a function of *overlap* and *energy* factors.

5.2.2 Response *stress area*

The factor screening and factor interactions for the response *stress area* S_A are presented in Figure 5.6a) and b), respectively. The main factor effects on the *stress area* show similar significance order as factor effects on the *stress at 0.01 mm*: A: *optics*, C: *energy*, B: *overlap*. However, the main effects cannot be considered separately because A•C and B•C interactions are significant. A•B and A•B•C demonstrate no interaction, which means that the *optics* and *overlap* influence the profile's *stress area* independently of each other when the *energy* is constant. This statement allows the control of the *stress area* by combining the desired *optics* and the given number of *overlaps* and by keeping the laser power at a certain level.

In Table 5.3, the P-values of the significance test for the *stress area* are listed. All significant terms have P-values much lower than the significance level of 0.1 defined in this work. This proves that the number of factor levels of unique experimental runs and the number of replicates are sufficient for determining the significance of factor effects. Moreover, this statement confirms that the power study made prior to the conduction of experiments is accurate. In cases when P-values are close to the defined significance level, more experiments must be carried out.

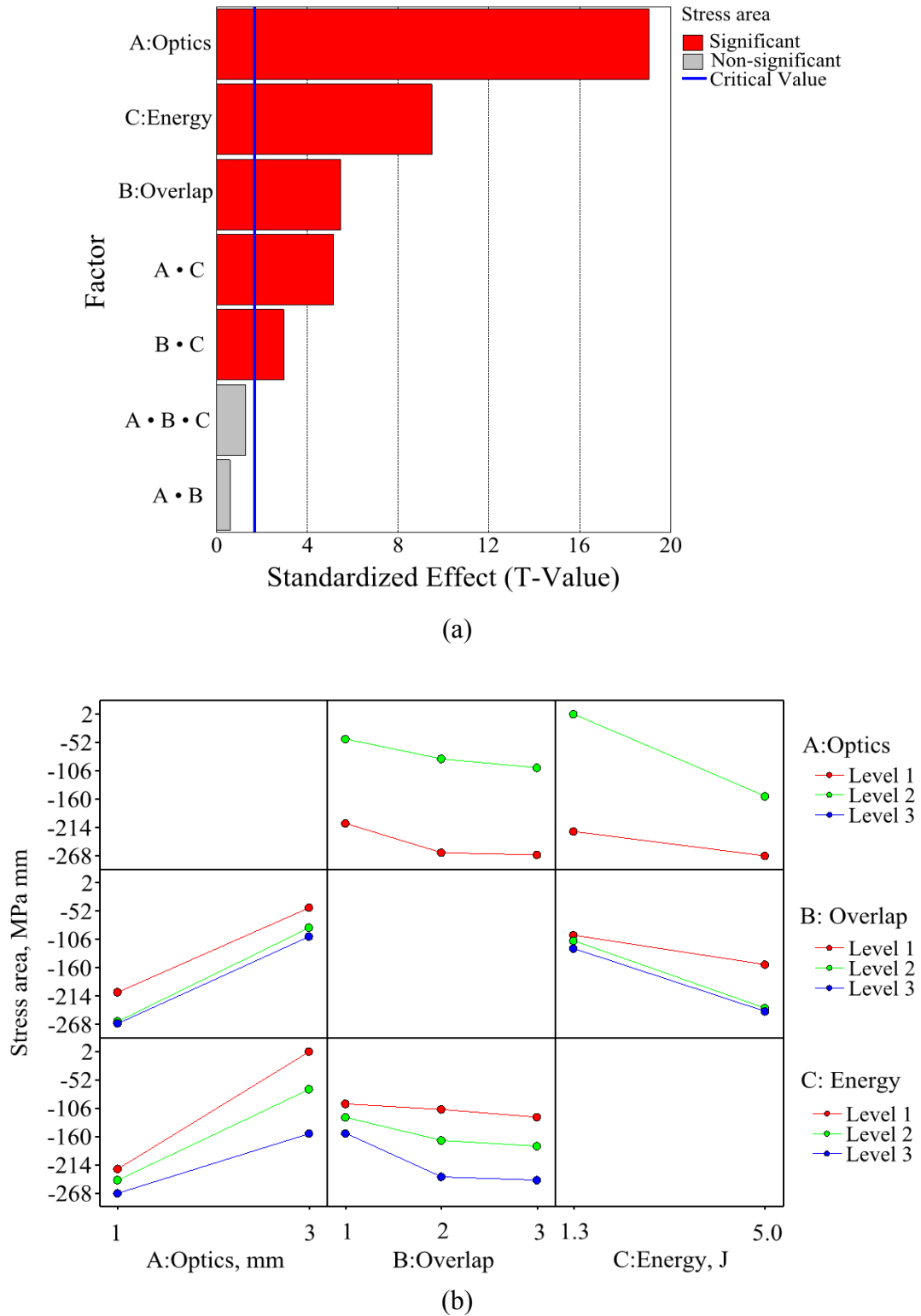
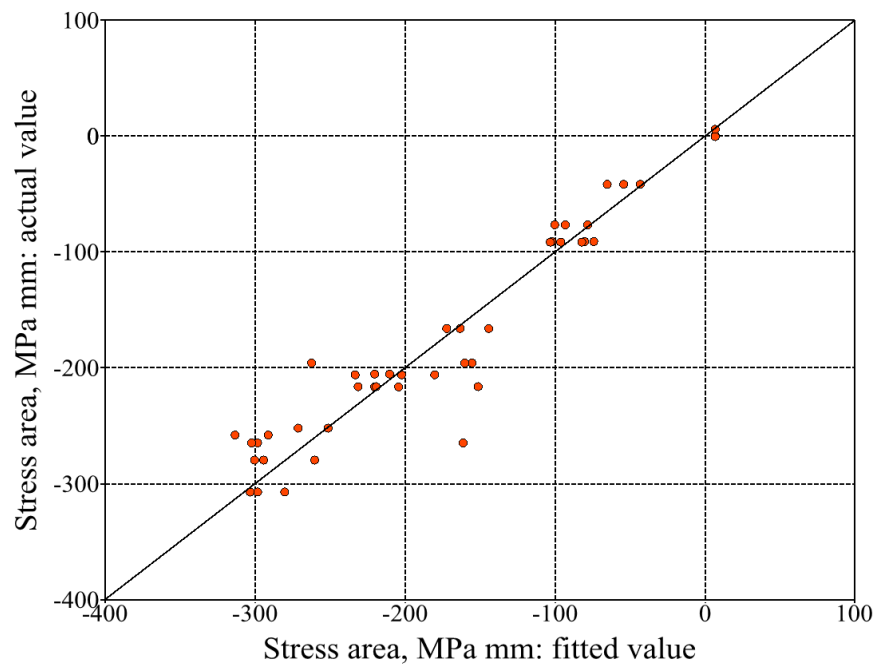


Figure 5.6 *Stress area* response: (a) factor screening, (b) factor interaction effects.

Table 5.3 Response *stress area*: P-values of the regression model.

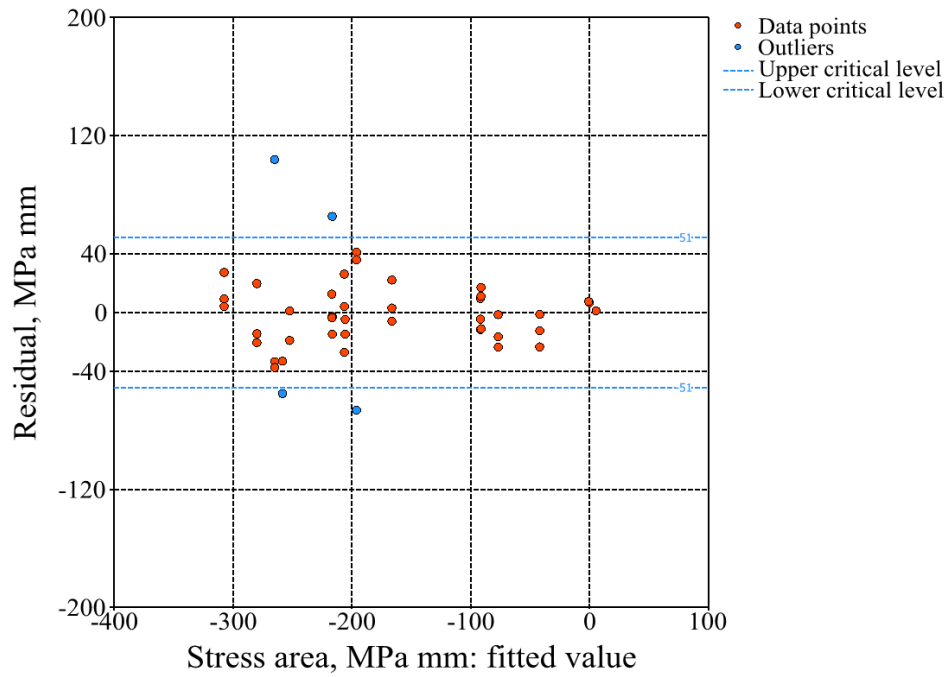
Term	P Value
A: Optics	0
B: Overlap	3.11E-06
C: Energy	1.48E-11
A • B	0.5564
A • C	8.58E-06
B • C	0.0052
A • B • C	0.2078

The achieved R^2 value of 93.61% indicates a high level of model fitness into the experimental data. The fitted response values versus the experimental values are presented in Figure 5.7. The quality of the regression model for the *stress area* is higher than that of the model for the *stress at 0.01 mm* within the same DOE. This means that the relationship between factors and *stress at 0.01 mm* is more complex and generally requires more observational runs to enhance the acceptable quality of the regression model.

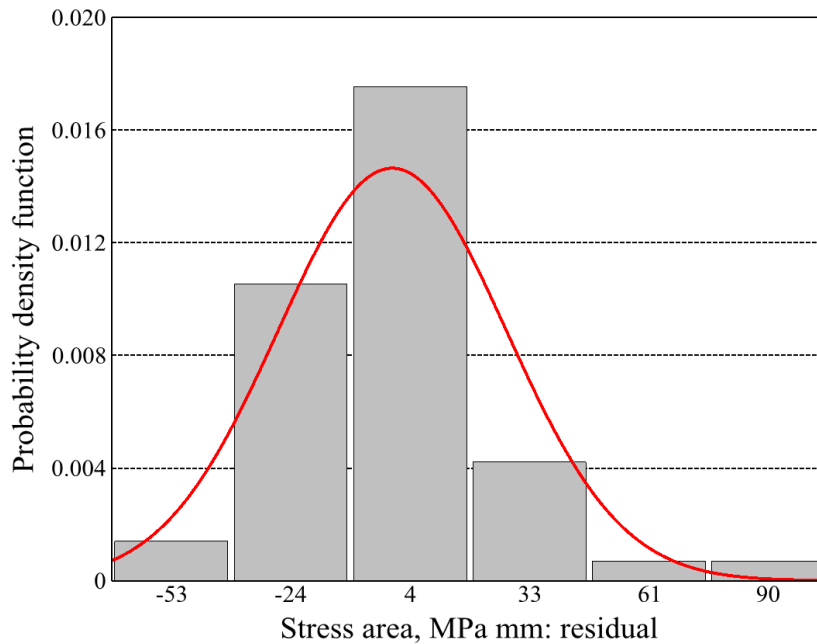
Figure 5.7 *Stress area* response: identification quality of the fitted regression model.

The verification of the model adequacy was done by conducting the analysis of residuals. The residuals of the regression model are shown in Figure 5.8a). No trends or patterns are seen on the graph. The same four observations that were identified as outliers in the residual analyses for the *stress at 0.01 mm* fall outside of the 10% critical region. All four experimental runs are

consequently excluded from the subsequent analysis. The probability distribution of residuals of fitted regression model is illustrated in Figure 5.8b). The residuals are normally distributed, which validates the high level of the regression model fitness.



(a)



(b)

Figure 5.8 *Stress area* response: (a) analysis of residuals of the fitted regression model, (b) probability distribution of residuals of the fitted regression model.

For examination of the influence of the *overlap* and *energy* variations on the *stress area* while keeping the *optics* at 1 mm, the 3D plot is drawn in Figure 5.9. The response surface is symmetric relative to the vertical plane passing through the maximum and minimum response values on the plot. The factors contribute in equal manner to the response variation: *stress area* decreases towards more negative values by increasing proportionally either *overlap* or *energy* and reaches its minimum when factors are at their maximum values and vice versa. The *overlap* and *energy* have a little interaction effect on the *stress area*, as also shown in the statistical test. Therefore, based on the available laser power and the cost of LSP processing, one can achieve desired *stress area* value by keeping the pulse *energy* and increasing the number of *overlap* or keeping the number of *overlap* and vary the pulse *energy*.

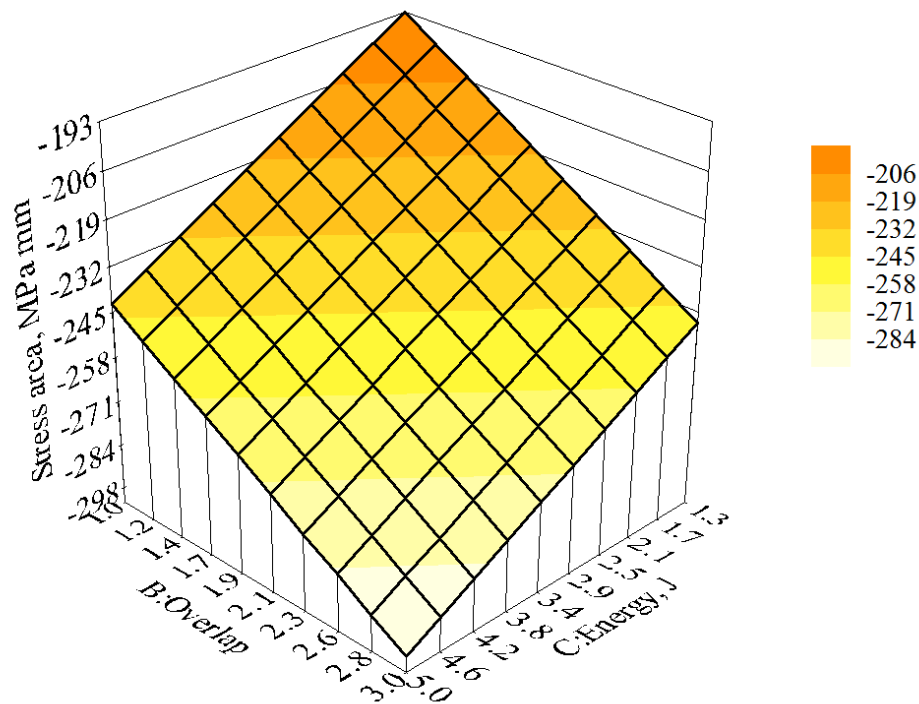


Figure 5.9 *Stress area* response as a function of *overlap* and *energy* factors.

5.2.3 Response stress at 0.5 mm

The factor screening and factor interactions for the response *stress at 0.5 mm* $S_{0.5}$ are presented in Figure 5.10a) and b), respectively. A significance order of the main factors remains similar as in the other responses: A: *optics*, C: *energy*, B: *overlap*. But in this case, the interaction A•C is revealed to be significant. This means that the energy level should be adjusted according to the optic system in use, when a desired *stress at 0.5 mm* should be achieved. B•C and A•B•C interactions have the least significance, which allows the consideration of *energy* and *overlap* effects on the *stress at 0.5 mm* independent of each other when keeping the *optics* constant.

In Table 5.4, the P-values of the significance test for the *stress at 0.5 mm* are listed. The effects of the main terms make the P-values much lower than the significance level of 0.1. B•C and A•B•C P-values exceed 0.04, i.e. the extreme case of the statistical test is 4%. This indicates that these interaction effects are revealed to be unimportant within the experimental data.

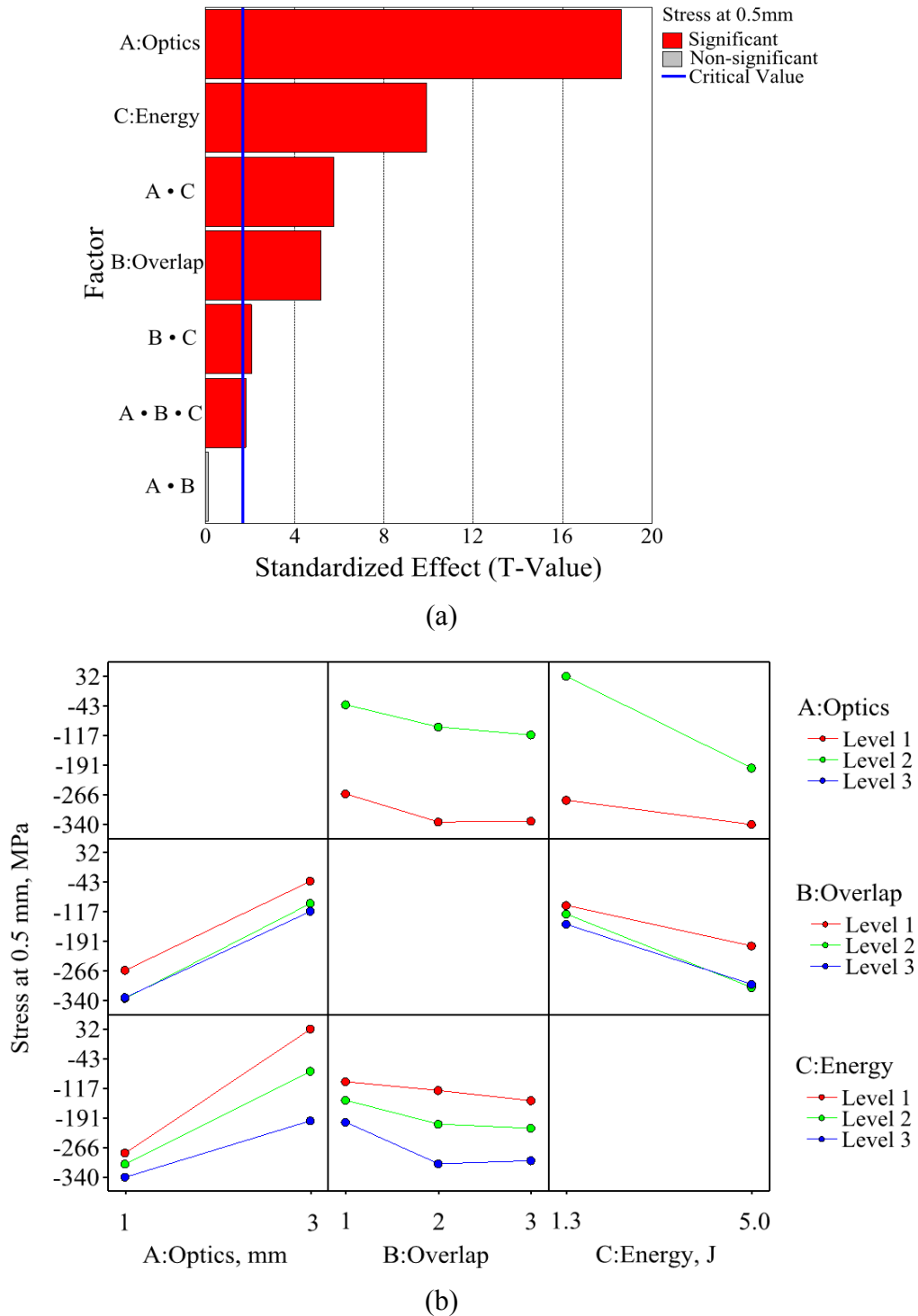
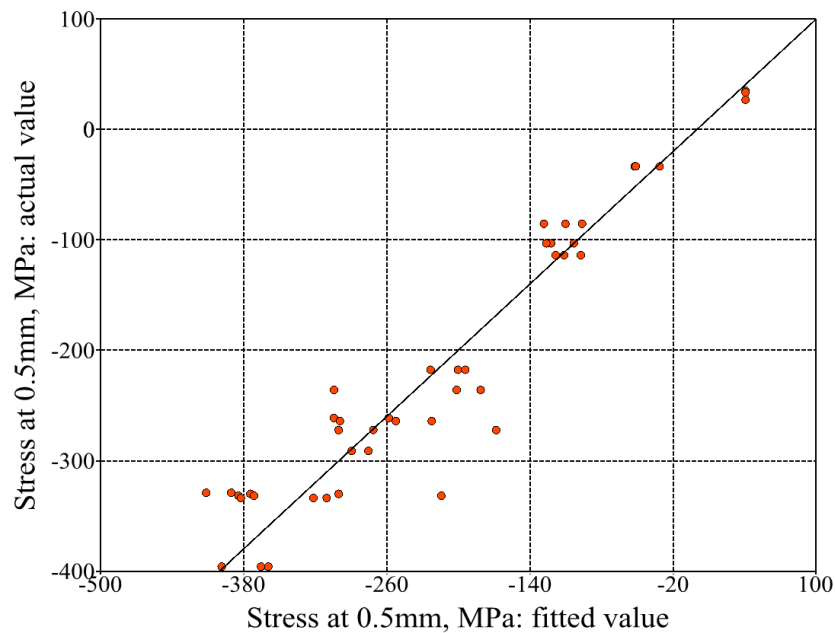


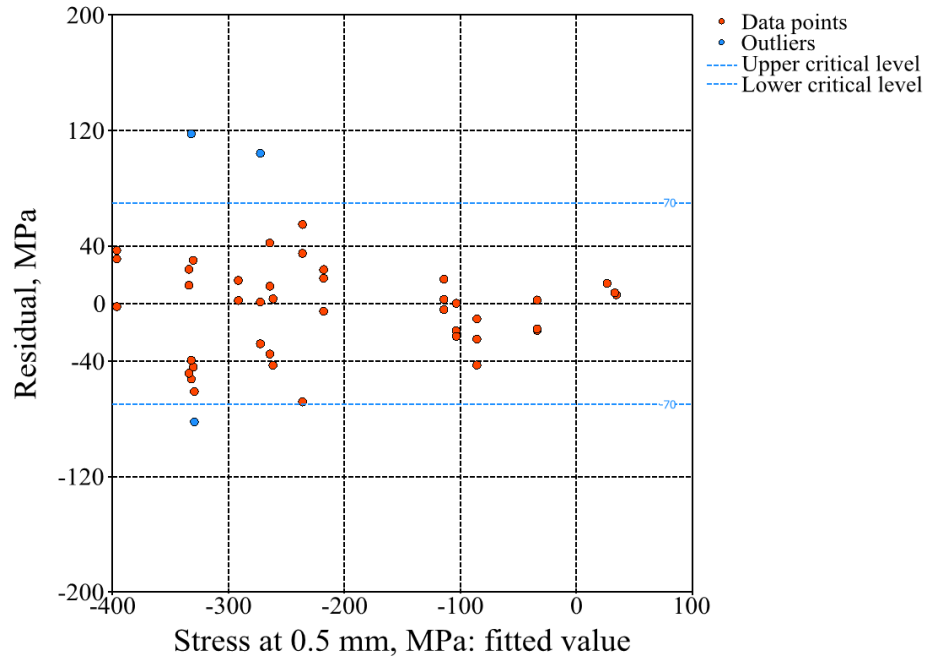
Figure 5.10 *Stress at 0.5 mm* response: (a) factor screening, (b) factor interaction effects.

Table 5.4 Response *stress at 0.5 mm*: P-values of the regression model.

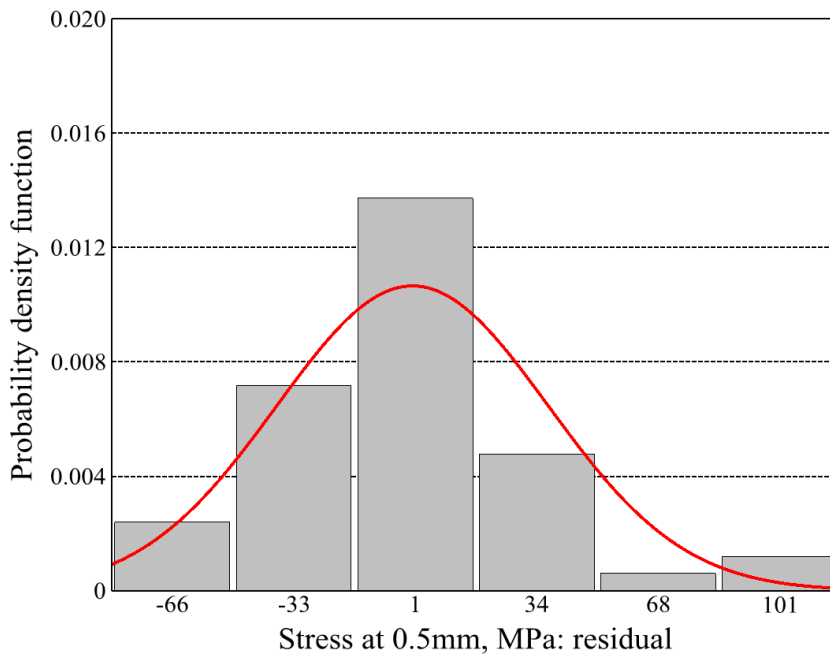
Term	P Value
A: Optics	0
B: Overlap	7.70E-06
C: Energy	435E-12
A • B	0.8898
A • C	1.20E-06
B • C	0.0447
A • B • C	0.0787

The regression model for *stress at 0.5 mm* fitted into the experimental data with the factor R^2 of 93.52%. The fitted response values versus the experimental values are shown in Figure 5.11. The quality of the regression model for the *stress at 0.5 mm* is comparable with the quality demonstrated by the response *stress area*. The observation runs are spread around a diagonal line, so that only some points happen to have a slightly higher offset. For further investigation of the outliers, the analysis of residuals is conducted. The residuals of the regression model are presented in Figure 5.12a). Three observations are out of the 10% critical region — they are the ones identified in the analysis of other responses. The data points present no pattern within the critical region. The probability distribution of residuals of the fitted regression model is illustrated in Figure 5.12b). The residuals are normally distributed, which validates a high level of fitness of the regression model.

Figure 5.11 Identification quality of the fitted regression model for *stress at 0.5 mm* response.



(a)



(b)

Figure 5.12 *Stress at 0.05 mm* response: (a) analysis of residuals of the fitted regression model, (b) probability distribution of residuals of the fitted regression model.

For examination of the effect of *overlap* and *energy* on the *stress at 0.5 mm* when the *optics* is kept at 1 mm, the response surface is presented in Figure 5.13. The response surface of the *stress*

area has a similar shape and symmetrical orientation as the ones of other responses investigated previously: *stress at 0.5 mm* decreases towards higher compression stresses by increasing either *overlap* or *energy* and reaches its minimum value when the factors are at their maximum values and vice versa. This means that both *overlap* and *energy* have almost equal significant effects and little interaction effect on *stress at 0.5 mm*, as also inferred in the statistical test. The factors levels should be adjust according to the desired *stress at 0.5 mm* value (isoline).

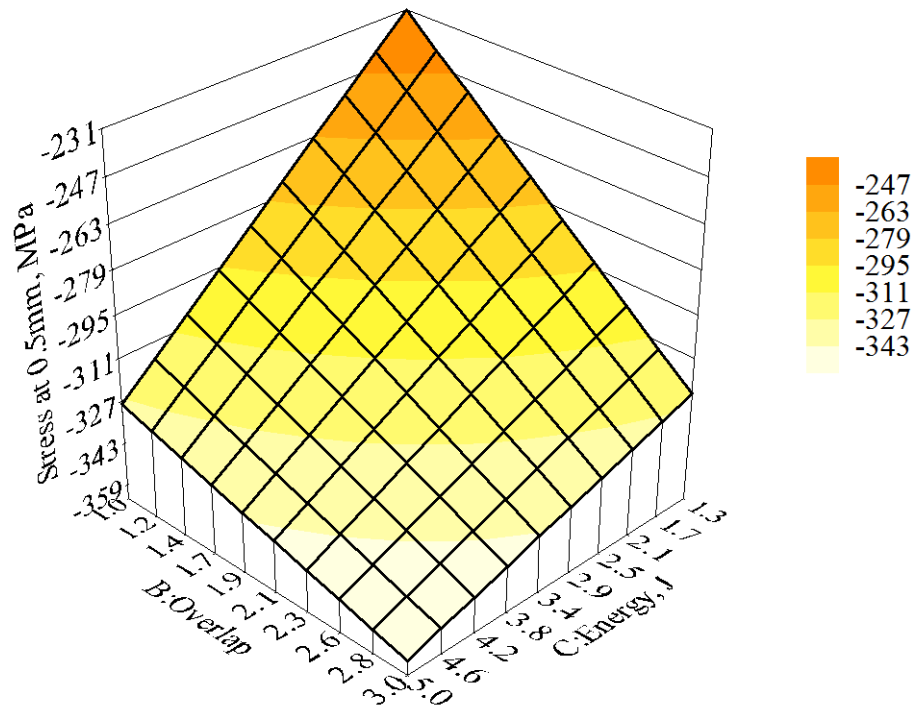


Figure 5.13 *Stress at 0.5 mm* response as a function of *overlap* and *energy* factors.

5.3 DOE: optimization of LSP process regarding the residual stresses

The relationship between the responses and factors built from the regression models as provided from the DOE software [143] are presented in Figure 5.14. The factor effects on the responses are compared in a row based on the slope angle. The *energy* factor has a quantitative nature; thus, it takes all values within the observation region 1.3–5J. The *optics* and *overlap* factors are qualitative and only the investigated discrete values are presented. For the convenience of comparison, the observation data are connected with lines. Considering all responses, the *optics* shows the highest slope, while *overlap* and *energy* have pretty much equal slope. This stands in agreement with the significance order of the factor effects on the responses: the *optics* is always of higher importance, while *overlap* and *energy* have comparable importance. The responses take their minimum values when the factors are at maximum values and vice versa.

For verification of the regression model, the response values obtained from the regression model at untested factor's combination: 1mm optics, two times overlap, 4.0 J energy, are presented in Figure 5.14. The predicted response values are following: $-257 \text{ MPa mm stress area}$, $-85 \text{ MPa stress at } 0.01 \text{ mm}$, $-326 \text{ MPa stress at } 0.5 \text{ mm}$. The experimental verification of the regression model in regard to the untested response values is discussed in the next chapter.

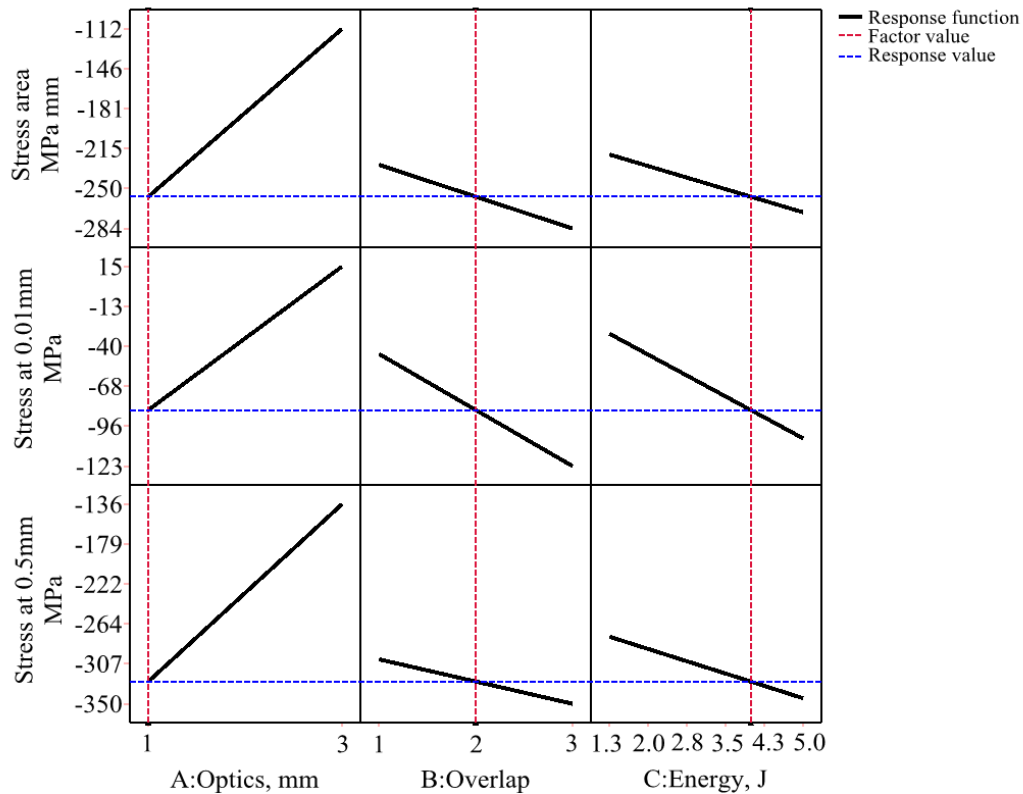


Figure 5.14 Identified relationship between the responses and factors.

In Figure 5.15, the *stress area* is plotted over the *energy* and *overlap* when using 1mm *optics*. The feasible regions of the *energy* and *overlap* variation corresponding to the *stress area* more negative than -200 MPa mm , -220 MPa mm , -250 MPa mm , and -290 MPa mm are illustrated in orange in Figure 5.15a), b), c), and d), respectively. The red curve shows the least factor values that provide the given *stress area* value and thereby divides the plot into two parts. In Figure 5.15a), b), c) it can be seen that the given *stress area* values can be achieved by increasing the number of *overlap* and keeping the *energy* at minimum level. Therefore, in order to generate the desired *stress area* value, one should adjust the *energy* and *overlap* levels based on the available laser energy and the cost of one LSP shot (one overlap). As shown in Figure 5.15d) the *stress area* of -290 MPa mm can be only achieved by applying maximum factor's levels: 5 J, 3 overlap.

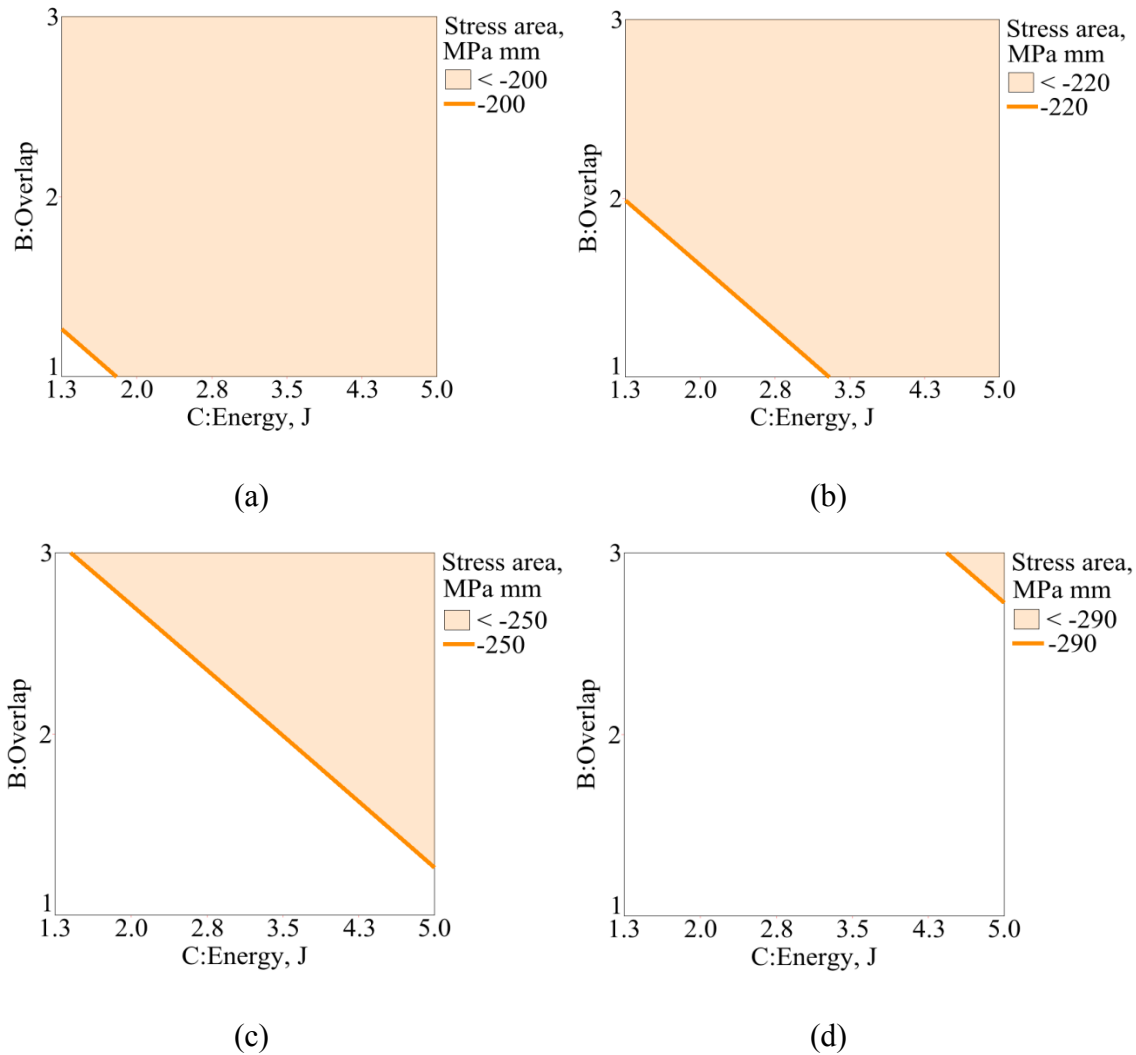


Figure 5.15 Feasible range of the *energy* and *overlap* variation for achieving: (a) *stress area* < -200 MPa mm, (b) *stress area* < -230 MPa mm, (c) *stress area* < -250 MPa mm, (d) *stress area* < -290 MPa mm. *Optics* 1 mm.

Figure 5.16 presents the *stress area* as a function of *energy* and *overlap* variation when using a 3mm *optics*. The feasible regions of the *energy* and *overlap* variation corresponding to the *stress area* more negative than -20 MPa mm, -70 MPa mm, -130 MPa mm and -200 MPa mm are illustrated in orange in Figure 5.16a), b), c) and d), respectively. All plots demonstrate higher influence of the *energy* on the response than the *overlap*. The red line which reflects the least factors combinations has a curvature. Figure 5.16a), b), c) depict that for achieving given level of the *stress area* either of factors — *energy* and *overlap* can be adjusted according to the available resources. As shown in Figure 5.16d) maximum *stress area* of -200 MPa mm requires using maximum energy of 5 J and 3 overlap.

When comparing Figure 5.15 (for 1 mm *optics*) and Figure 5.16 (for 3 mm *optics*), one can see that -200 MPa mm is a transition value of the *stress area* that characterizes transfer between 3 mm and 1mm *optics*.

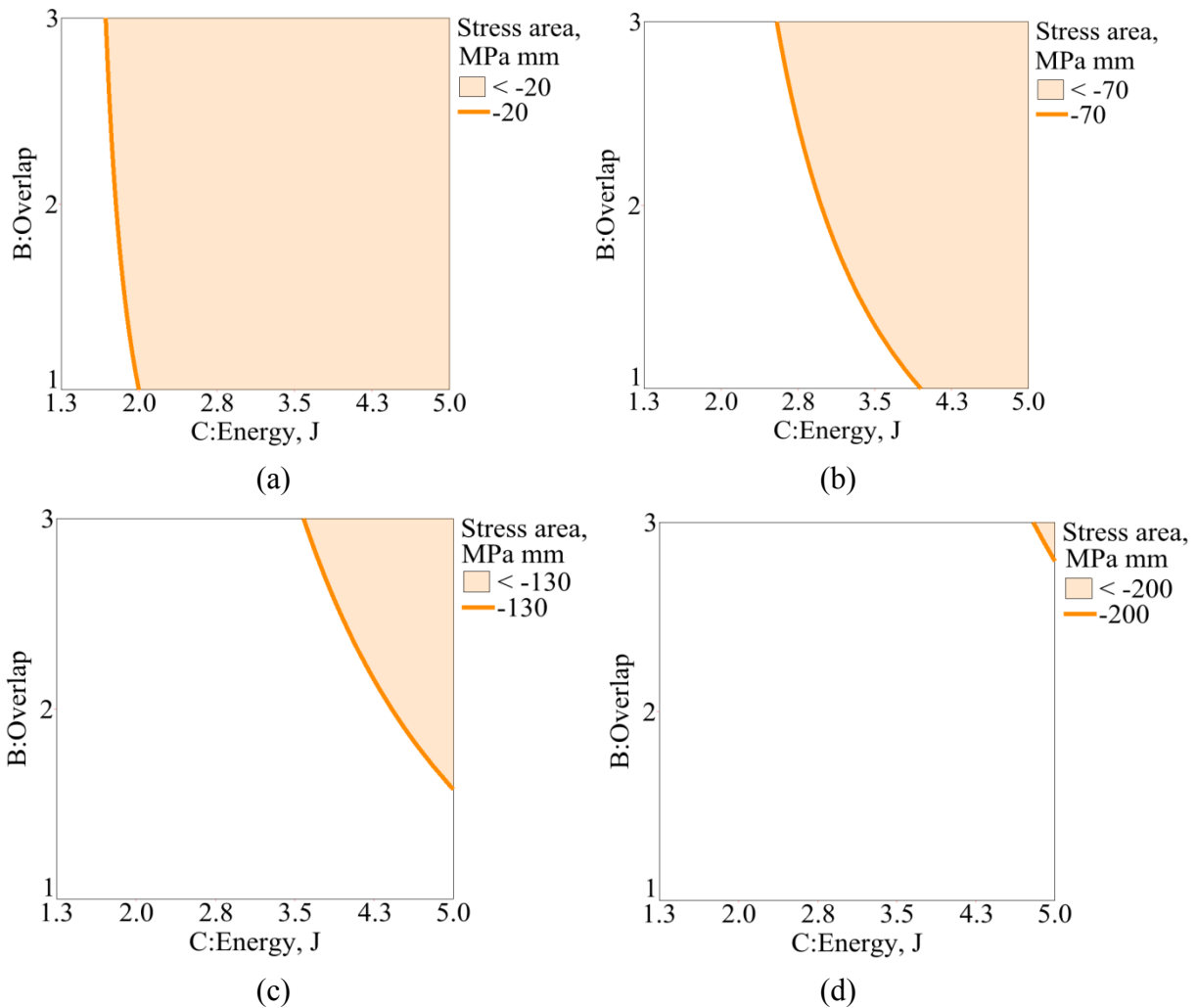


Figure 5.16 Feasible range of the *energy* and *overlap* variation for achieving: (a) *stress area* < -20 MPa mm, (b) *stress area* < -70 MPa mm, (c) *stress area* < -130 MPa mm, (d) *stress area* < -200 MPa mm. *Optics* 3 mm.

The optimization of *energy* and *overlap* for 1 and 3mm *optics* was performed in regard to *stress at 0.01 mm* and *stress at 0.5 mm* responses [143]. In Figure 5.17a), b) the *stress at 0.01 mm* and *stress at 0.5 mm* are plotted over the *overlap* and *energy* for 1 and 3mm *optics*, respectively. In Figure 5.17a) the green and orange curves show the least factor levels that provide the *stress at 0.01 mm* of -100 MPa and the *stress at 0.5 mm* of -300 MPa, respectively. The region of *energy* and *overlap* variation corresponding to the *stress at 0.5 mm* values more negative than -100 MPa fully covers the region of factor variation for *stress at 0.01 mm* values more negative than -300 MPa. The feasible region of *energy* and *overlap* variation lies between the 3.1–5.0 J and one to two times overlaps. As shown in Figure 5.17b) the 3mm *optics* is capable of providing only the

stress at 0.01 mm of -20 MPa by adjusting the energy and overlap to their highest levels of 5 J and three times, respectively.

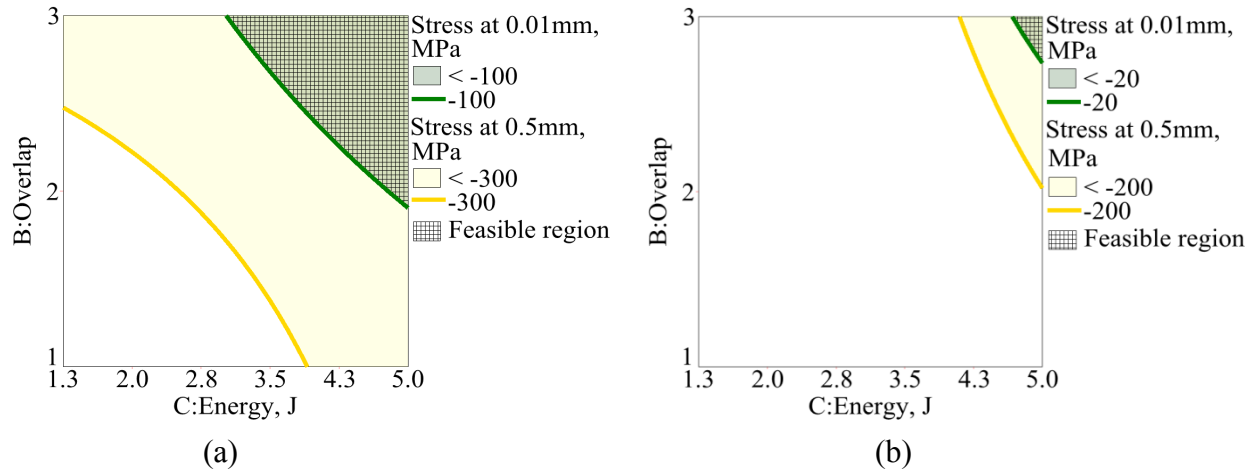


Figure 5.17 Feasible range of the energy and overlap variation for achieving: (a) stress at 0.01 mm < -100 MPa, stress at 0.5 mm < -300 MPa, optics 1 mm, (b) stress at 0.01 mm < -20 MPa, stress at 0.5 mm < -200 MPa, optics 3 mm.

The optimization of all residual stress responses for a 1mm optics is performed [143]. The stress area, stress at 0.01 mm and stress at 0.5 mm are plotted vs. the overlap and energy in Figure 5.18. The feasible region of all factors variation is equal to the acceptable region for stress at 0.01 mm. This means that within the investigated factor variations, the highest effort is required for achieving the desired stress at 0.01 mm compared to other responses.

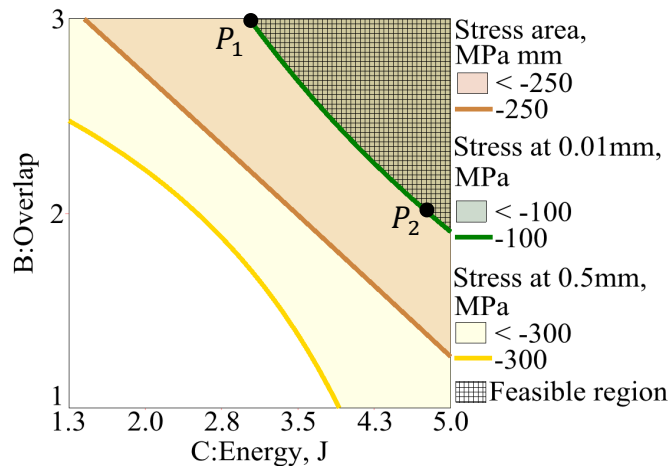


Figure 5.18 Residual stress responses optimization: the feasible range of the energy and overlap variation for 1mm optics.

As shown, the acceptable region of factor variations, corresponding to stress at 0.5 mm values more negative than -300 MPa, covers the regions of factor variations for other stress responses.

According to the feasible region, one can operate with minimum *energy* of 3.1 J and three times *overlap* (P_1) or maximum *energy* of 5 J and two times *overlap* (P_2). From the commercial point of view, the laser with the pulse energy of 3.1 J has a smaller price than the one with the pulse energy of 5.0 J. However, the increase in the number of overlap from two to three makes the processing time higher by 50%, thereby raising the cost of the laser treatment performance by 50% as well. It should be mentioned that operating with 1mm *optics* increases the processing time by the factor of 9 comparing with the 3mm *optics* in accordance with the treated areas.

5.4 DOE: experimental verification of the regression model

In Chapter 5.3, the prediction ability of the regression model for untested factors combination: 1mm *optics*, two times *overlap*, 4.0 J *energy* has been challenged and requires experimental verification which is scope of this section. For the given set of parameters the response values: -257 MPa mm *stress area*, -85 MPa *stress at 0.01 mm*, -326 MPa *stress at 0.5 mm* were returned by the model. The R^2 factor is reliably used as an indicator of how well new observations are predicted by the model. The only shortcoming of using R^2 for prediction is a disregard of the systematic experimental error, which is encountered in the new observations but is not involved in the regression model. However, this error is not significant and does not change the R^2 factor by more than 3–5%. R^2 factors are 81.91%, 93.61%, and 93.52% for response *stress at 0.01 mm*, *stress area*, and *stress at 0.5 mm*, respectively.

For the verification, three new specimens C(T)50 were identically treated with the given LSP parameters: 1mm *optics*, two times *overlap*, 4.0 J *energy* as shown in Figure 3.7 [143]. Then, the residual stresses were measured by the hole drilling. The measured stress profiles are presented in Figure 5.19. The analogous responses *stress at 0.01 mm*, *stress area*, and *stress at 0.5 mm* were determined from each of the measured stress profiles and accordingly averaged. The summary of the verification experiments is given in Table 5.5.

Table 5.5 The summary of verification experiments.

Number of experiment	Run order	A: Optics, mm	B: Overlap, number	C: Energy, J	Stress area, MPa mm	Stress at 0.01 mm, MPa	Stress at 0.5 mm, MPa
1	2	1	2	4.0	-274	-76	-339
2	1	1	2	4.0	-324	-127	-406
3	3	1	2	4.0	-284	-131	-353
Experiment: mean					-294	-111	-366
Prediction: value					-257	-85	-326
Prediction accuracy					0.87	0.77	0.89
R^2					0.94	0.82	0.94

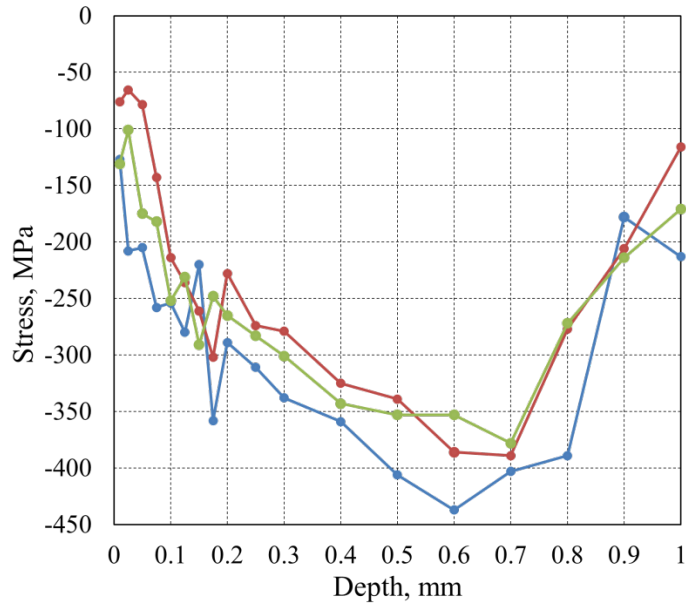


Figure 5.19 Residual stress profiles of the verification observations. LSP parameters: 1mm optics, 4.0 J energy, 2 overlap.

Furthermore, prediction accuracy was calculated as a ratio of the predicted value to an averaged experimental value and was compared with the R^2 factor. In terms of all responses, the prediction accuracy of the model is lower than its ability for data fitting. The observed differences are 7%, 5%, and 5% for the *stress area*, *stress at 0.01 mm*, and *stress at 0.5 mm*, respectively. The deterioration in prediction accuracy is caused by the measurement error of new observations, which is not included in the regression model.

The widely accepted level of the model prediction accuracy is 80%. Within the current experimental runs, only the *stress at 0.01 mm* demonstrates a slightly lower prediction accuracy of 77%, which is still acceptable within the framework. The prediction accuracy can be improved by performing additional observations at different factor levels or by performing extra replicates aimed to *stress at 0.01 mm*. The hole drilling measures the subsurface residual stresses at 0.01 mm depth less precisely due to the roughness of material surface and inaccurate definition of the position at which the driller touches the surface (null position). Therefore, the *stress at 0.01 mm* reflects the higher systematic measurement error.

5.5 DOE based on corrected residual stress profiles

5.5.1 Correction of measured residual stresses through the established methodology

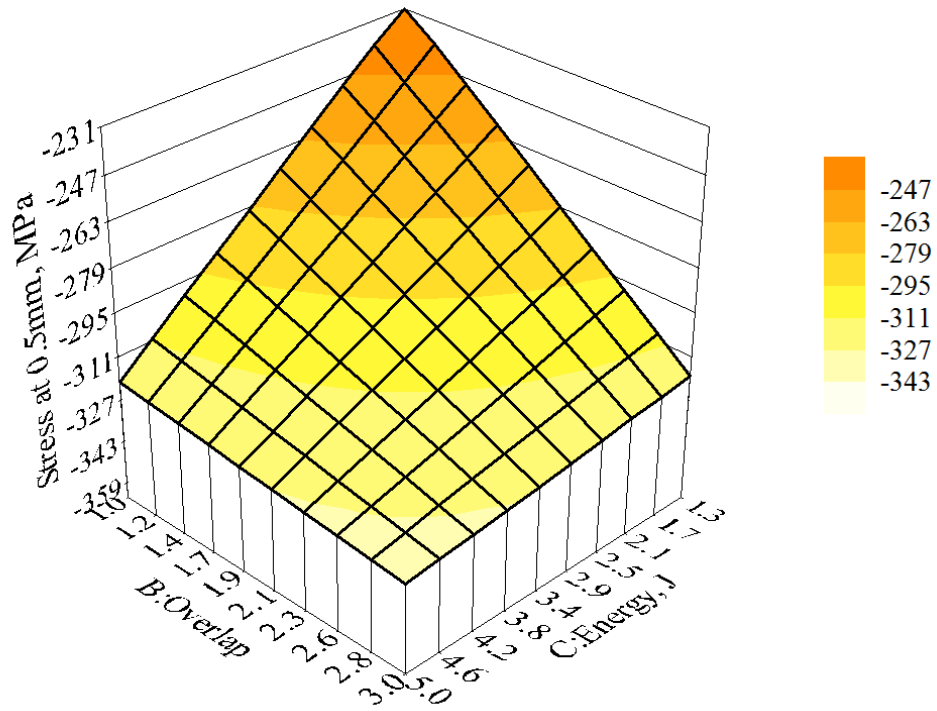
At the DOE optimization stage, various shapes and magnitudes of the residual stress profiles are examined. For the correction of the plasticity effect, which occurs when measuring LSP-shaped residual stresses approaching 80% of material yield strength, the established methodology using ANN is applied to all stress profiles. After the correction trained ANN returns the actual stress

profile regardless of the presence of plastic deformations, the stress profiles affected by nonlinearity are corrected, and no affected profiles are left unchanged.

Out of 50 experimental observations, 10 (20%) were corrected by ANN, while other observations remained unchanged. The required correction in the measured stress profiles (stress responses) and the corresponding LSP parameters are listed in Table A2. After correction, the *stress area* and *stress at 0.5 mm* are decreased up to 15%. *Stress at 0.01 mm* remains the same as prior to correction analogously with the profiles' correction discussed in Chapter 4.3.3, which is an artifact of the stress profile shapes used in the generation of ANN training patterns. Moreover, 15% of stress correction is comparable with 10–20% measurement error of the hole drilling equipped with ESPI and can be considered to be not significant when carrying out a single measurement. However, in the current work, the DOE is performed where a relationship between factor and response variables is obtained from the carefully planned experiments using statistical methods. Thus, the measurement error is considered by the regression model when predicting new observations. Therefore, the performed DOE is enhanced by including the correction of the measured stress profiles obtained through the ANN methodology.

5.5.2 Correction of the DOE regression model

The regression models of *stress at 0.5 mm* and *stress area* responses have been improved by taking into the account the stress correction of 10 observations. The response *stress at 0.5 mm*, as a function of *overlap* and *energy* factors for the corrected regression model, is presented in Figure 5.20. The *stress area* response as a function of *overlap* and *energy* factors for the corrected regression model is presented in Figure 5.21. Both surface functions in Figure 5.20 and Figure 5.21 show a similar pattern as Figure 5.13 and Figure 5.9, respectively: the *overlap* and *energy* have an almost equal influence on the *stress at 0.5 mm* and *stress area*, the responses decrease by increasing either factor. The surfaces are horizontally inclined at an angle of approximately 45 degrees. However, the corrected surface functions demonstrate higher curvature at higher negative values due to the reduction (correction) of the stress values approaching the yield strength of the material. Therefore, in the range of surface curvature, higher *overlap* and *energy* values have to be used in order to achieve the desired stress value. The minimum compressive *stress at 0.5 mm* increases from -359 MPa to -332 MPa and the minimum *stress area* increases from -298 MPa mm to -265 MPa mm.



The *stress area*, *stress at 0.01 mm* and *stress at 0.5 mm* are plotted over the *overlap* and *energy* for the corrected regression model in Figure 5.22. As demonstrated in Figure 5.20 and Figure 5.21, the corrected models show the curvature of *stress area* and *stress at 0.5 mm* functions, shifting the region of the minimum stress values towards the higher values. This makes the *stress at 0.01 mm* and *stress area* acceptable regions are almost identical after correction; they build up a feasible region of all responses. This means that after correction of stress profiles, *stress at 0.01 mm* and *stress area* — which directly influence the fatigue and fatigue crack propagation, respectively — require comparable effort for achieving desired values.

In conclusion, within the range of factor variations defined in the framework of DOE of LSP, the application of the correction by ANN methodology has slightly changed the regression model, because 80% of all observations did not reveal nonlinear deformations during the hole drilling measurements. However, there is a change in the minimum stress values and minimum integral stress area that can be achieved to lower values by 9% and 11%, respectively.

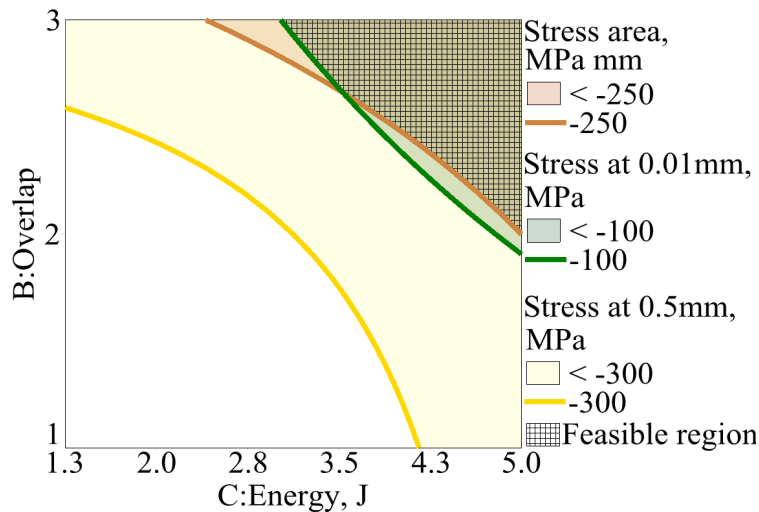


Figure 5.22 Residual stress responses optimization: the feasible range of the *energy* and *overlap* variation, 1mm *optics* for the corrected data.

5.6 Application of residual stresses for improvement of fatigue crack growth behavior

In this chapter, the FCP behavior of the C(T)50 specimens with the compressive residual stresses is demonstrated. For this reason, the LSP has been performed using different process parameters from the DOE-investigated range and, subsequently, FCP tests carried out, see also section 2.4.2.

A 2.0mm-thick AA2024T3 sheet without a clad layer was used in the experiments. The illustration of the C(T)50 specimen with the sequence of the LSP spots is presented in Figure 5.23. The results of fatigue crack propagation experiments and the corresponding LSP

5.6 Application of residual stresses for improvement of fatigue crack growth behavior

parameters are given in Table 5.6. LSP without coating was performed using a Q-switched Nd:YAG laser operating at 10 Hz with a pulse duration of 10 ns. According to the DOE results, a $1\text{ mm} \times 1\text{ mm}$ diffractive square optics was used. Two sides of each C(T)50 specimen were treated. The specimens had been “pre-cracked” 1 and 5 mm from the original crack tip of 10 mm. The pre-cracking was performed parallel to the rolling direction and the LSP treatment of $5\text{ mm} \times 5\text{ mm}$ area with 1mm *optics* was applied on the surface covering the crack tail of 1 mm length, as shown in Figure 5.23.

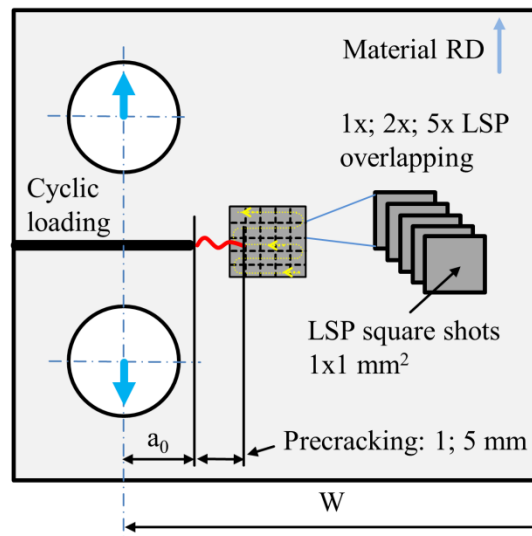


Figure 5.23 C(T)50 specimen for measurement of fatigue crack propagation after LSP treatment. $a_0=10\text{ mm}$, $W=50\text{ mm}$.

As shown in Table 5.6, the specimens with LSP treatment depict a significantly higher number of cycles required for propagating the fatigue crack to an a/W value of 0.6 (crack length, a , divided by the C(T)50 specimen width from the pin holes, W (50 mm), Figure 5.23). The maximum fatigue life extension of 14 times relative to the untreated specimen was achieved for the LSP 3J, 1×1 , 1×1 and minimum of 1.8 times for LSP 1.3J, 1×1 , 1×2 . The treatment conditions for LSP 5J, 1×1 , $5 \times$ and LSP 5J, 1×1 , $1 \times$ were excessive, which had led to the complete suppression of the crack growth; thus, these data could not be accounted for. For this reason, instead of 1 mm, pre-cracking of 5 mm was performed in the following tests; thus, the crack tracking starts from approx. $0.3 a/W$.

Table 5.6 Results of the fatigue crack propagation test

Specimen name	Laser shock peening parameters			Number of cycles to failure	Life extension, number	Pre-crack, mm
	Optics, mm	Energy, J	Overlap, number			
BM 1	-	-	-	27900	<i>reference:</i> 29525 cycles	-
BM 2	-	-	-	31150	<i>reference:</i> 29525 cycles	-
LSP 5J, 1×1, 5×	1	5	5	suspended	suspended	1
LSP 5J, 1×1, 1×	1	5	1	suspended	suspended	1
LSP 1.3J, 1×1, 1× 1	1	1.3	1	65400	2.2	5
LSP 1.3J, 1×1, 1× 2	1	1.3	1	53200	1.8	5
LSP 3J, 1×1, 1× 1	1	3	1	422000	14.3	5
LSP 3J, 1×1, 1× 2	1	3	1	280100	9.5	5
LSP 1.3J, 1×1, 2× 1	1	1.3	2	375000	12.7	5
LSP 1.3J, 1×1, 2× 2	1	1.3	2	275000	9.3	5

Figure 5.24 depicts the results of FCP tests performed using 1×1mm optics. In the first case, the effect of the overlap number on fatigue crack growth life while keeping the laser energy at 1.3 J is analyzed. The a/W vs. number of cycles N and the FCP rate, da/dN vs. a/W , are presented in Figure 5.24a) and c). Specimens with identical treatment conditions LSP 1.3J, 1×1, 2×1 and LSP 1.3J, 1×1, 2×2 show experimental scatter of 375,000 and 275,000 cycles. The average fatigue life improvement is 2 and 11 times for 1× and 2× overlaps respectively, due to the high compressive residual stresses in treated area. In the second case, the effect of laser energy on fatigue crack growth when performing only one overlap is analyzed and the FCP results are presented in Figure 5.24b), d). Identical specimens LSP 3J, 1×1, 1× 1 and LSP 3J, 1×1, 1×2 demonstrate experimental scatter of 422,000 and 280,100 cycles, where the average fatigue life extension is 12 times. When comparing these two cases, it can be seen that the increase in either the laser energy (3J) or a number of overlaps (2) leads to the comparable improvement of fatigue

5.6 Application of residual stresses for improvement of fatigue crack growth behavior

performance by the factors of 12 and 11, respectively. The correlation between the fatigue life improvement and the generated residual stress profiles achieved in DOE study for given LSP parameters can be established. In Figure 5.15b) and Figure 5.21, the *stress area* contour values of these two treatment conditions almost lie on the same isoline. Since the *stress area* has a strong effect on FCP, comparable *stress area* values of stress profiles demonstrate similar fatigue life improvement of treated specimens. In what follows, in order to achieve the desired fatigue life extension, the laser energy and the number of overlaps can be adjusted according to Figure 5.15 and Figure 5.21 for the required *stress area* value. As already mentioned in Section 5.3, the cost of LSP performance consists on the price of the laser according to the given pulse energy and the processing time which is defined by the optics in use and the number of overlaps. Therefore, LSP parameters should be adjusted to the levels which minimize the cost of LSP performance and provide desired FCP improvement.

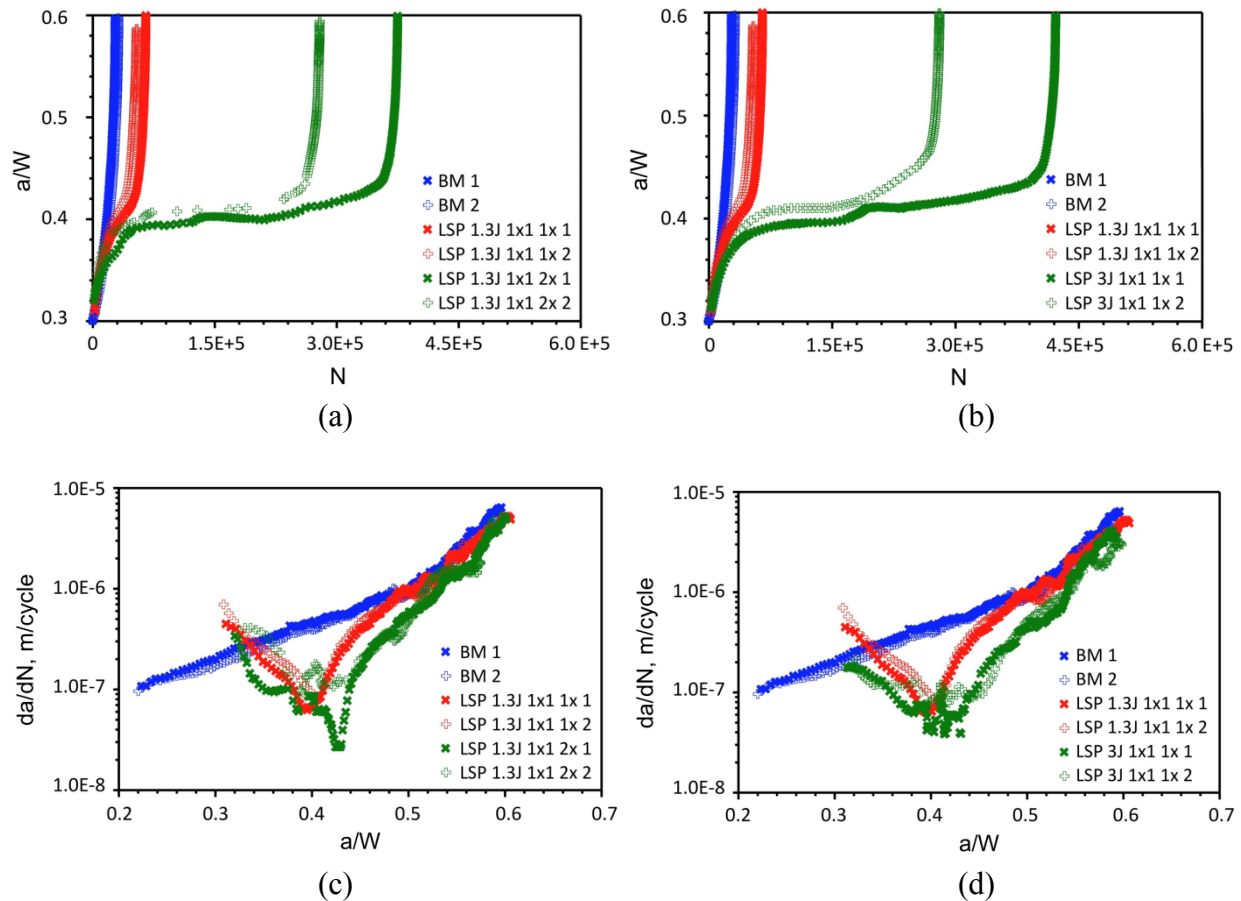


Figure 5.24 FCP test results: a/W vs. number of cycles N (a) LSP 1.3J, 1×1, 1× and 2×, (b) LSP 1.3J and 3J, 1×1, 1×; da/dN vs. a/W (c) LSP 1.3J, 1×1, 1× and 2×, (d) LSP 1.3J and 3J, 1×1, 1×.

In Figure 5.24c) and d), the comparable curves of the FCP rate da/dN throughout the whole a/W specimen range are presented. Analogous to the synchrotron analysis results obtained by Kashaev et al. [78], in the beginning of the FCP test, up to approximately 20,000 cycles ($a/W = 0.32$), treated specimens indicate slightly higher values of da/dN comparing with base material due to the presence of tensile residual stresses in front of the crack tip. When the crack reaches the compressive region, the crack growth rate da/dN decreases rapidly and meets its minimum at approx. $a/W = 0.4$. The significant mitigation of the fatigue crack propagation is clearly attributed to the presence of the deep compressive residual stresses in treated area, which cause the crack closure under the cyclic loading [78, 124, 128]. Beginning with an a/W value of approximately 0.4-0.42 (border of the LSP area), the FCP rate da/dN increases with an increasing a/W ; and at an a/W value of approximately 0.5, where tensile residual stresses occur, the FCP rates of specimens with the LSP treatment reach the FCP rate of the BM specimen.

5.7 Conclusions

The optimization of LSP process parameters — the laser pulse *energy*, the number of *overlaps* of LSP spots and the *optics* system, which constitute the cost of LSP performance — in regard to the generated residual stress profiles was conducted by employing the statistical methods of DOE. The quantities of the residual stress profile: *stress at 0.01 mm*, *stress at 0.5 mm* and the *stress area*, which strongly affect fatigue and fatigue crack growth behaviors, were used as optimization functions (responses). The general full factorial design consisting of 54 experiments was performed in order to systematically investigate all main and interaction factors (LSP parameters) effects on the responses (stress quantities). The stress quantities were carefully analyzed using statistical tools and the corresponding regression models were obtained. The accuracy of the regression models for prediction was experimentally validated according to the acceptance level of 80%.

DOE analysis shows that the number of *overlaps* and the laser pulse *energy* have almost equal significant effects and little interaction effect on stress quantities and, therefore, on residual stress profiles. Which means that the *overlap* and *energy* can be inverse proportionally varying in order to achieve desired stress profile, when keeping the *optics*.

The feasible region of LSP parameters variations, which leads to defined ranges of the stress quantities — *stress at 0.01 mm* < -100 MPa, *stress at 0.5 mm* < -300 MPa, *stress area* < -250 MPa mm —, was obtained. It is found that the highest effort is required for achieving the defined *stress at 0.01 mm* compared to other stress quantities; and only possible when 1×1 mm *optics* is used. According to the feasible region, one can operate with minimum *energy* of 3.1 J and three times *overlaps* or maximum *energy* of 5 J and two times *overlaps*. Commercially more profitable to work with the laser energy of 3.1 J because the laser price is smaller in comparison with the

lasers operating at the energy of 5.0 J. However, the increase in the number of *overlaps* from two to three raises the processing time by a factor of 1.5, which leads to an increase in cost of the laser treatment by 50%.

All measured stress profiles from DOE were subjected to the correction via the established ANN methodology. 20% of the stress profiles which were affected by the plastic deformation during the measurement were modified. Therefore, the regression models have been corrected as well. As a result, the minimum compressive *stress at 0.5 mm* is corrected from -359 MPa to -332 MPa and the minimum *stress area* is corrected from -298 MPa mm to -265 MPa mm; while *stress at 0.01 mm* remains unchanged. This corresponds to the raise of minimum stress values and minimum integral stress area of desired stress profiles by 9% and 11%, respectively. It is revealed, that when using 1×1 mm *optics* and the laser energy and a number of overlaps exceeding 3 J and 2 times, respectively, the generated residual stresses measured by the hole drilling technique require correction.

The fatigue crack propagation behavior of the LSP-treated specimens using the process parameters obtained in the DOE study has been investigated. LSP treatment conditions — 1.3 J, 2 overlaps and 3 J, 1 overlap — demonstrate significant fatigue life extension by the factor of 11 and 12, respectively, in relation to the base material; they generate the residual stress profiles with comparable integral stress area as predicted by DOE. This means that desired fatigue life extension can be achieved by adjusting the LSP parameters for required integral stress area according to the established DOE regression model. The main cause of the significant retardation of the fatigue crack growth is the crack closure effect under the cyclic loading, which is originated from the presence of the deep compressive residual stresses in the LSP-treated area.

6. Summary and conclusions

The hole drilling method determines residual stresses by measuring surface relaxations around the hole which are caused by the stress redistribution. The method assumes linear elastic material behavior which restricts it to measuring residual stresses below 60-70% of the yield strength. Therefore, when measuring residual stresses exceeding this limit plastic deformation arises, thereby causing the errors in stress determination. This problem has been addressed by several studies [27, 33–35], however the proposed solutions are limited to the specific materials and do not consider non-uniform stress gradients of up to 4000 MPa/mm, which are typical for laser shock peening (LSP).

In present work the methodology for the correction of the high residual stresses, which utilizes finite element modelling and artificial neural network (ANN), is established. In contrast to the recent studies, the novelty of this methodology lies in the practical and elegant way to correct any non-uniform stress profile for a wide range of stress levels and material behaviors typically used in industrial applications. The finite element model is experimentally validated on the stress profiles with a linear gradient generated in a AA2024-T3 alloy using a three-point bending testing system. The correction of LSP-generated stress profiles using the established ANN methodology is demonstrated. The main results achieved with the help of ANN are following:

- In extension of the commonly assumed 60% limit, the hole drilling method properly measures the LSP-shaped residual stress profiles up to 80% of the yield strength, because no or only very limited plasticity occurs in this case.
- Beyond this value, the normalized errors $\Delta\sigma_{avg}/\sigma_{yield}$ and $\Delta\sigma_{max}/\sigma_{yield}$ grow progressively and reaches maximum values of 43% and 110%, respectively.
- The errors' scatter reflects that, besides the stress magnitude, the effect of plasticity is strongly dependent on the combination of the shape of the stress profile and the depth where the peak values occur. Wherein the increasing width of the scatter band shows that the relevance of the profile shape gains in importance with increasing stress level $\sigma_{PD,max}/\sigma_{yield}$.
- The correction by the neural network significantly reduces the mean absolute errors to 10 MPa, which is comparable with the accuracy of hole drilling.

The established ANN correction methodology has demonstrated effective identification of “actual” stress profiles and can therefore be combined with the commercial residual stress measurement equipment such as “Prism” in order to account for the plasticity effect. The approach can be easily adapted for the correction of residual stresses generated by means of other surface modification techniques such as shot peening or hammer hardening, by including the occurring patterns in the training of the network, which carry the information about the

typical profile shapes and treated materials. The neural network needs to be trained with simulation data only once; then it can be used for stress correction of residual stress profiles with no need of caring for validity limits concerning the magnitude of residual stress related to the yield strength. This would promote the usage of the hole drilling method in industrial applications due to the accurate determination of the high residual stresses in metallic structures.

The laser shock peening (LSP) process has been optimized in regard to the generated residual stress profiles using design of experiments (DOE) techniques. It was experimentally demonstrated that the established regression model is capable of deriving accurate predictions of the residual stress profile when using given LSP parameters and vice versa. The proposed ANN methodology was applied for the correction of the measured stress profiles. The main achievements can be summarized as follows:

- LSP parameters — number of *overlaps* and laser pulse *energy* — have almost equal significant effects and little interaction effect on residual stress profiles, which means that they can be inverse proportionally varying in order to achieve desired stress profile, when keeping the *optics*.
- For achieving the stress quantities defined in present work — *stress at 0.01 mm* < -100 MPa, *stress at 0.5 mm* < -300 MPa, *stress area* < -250 MPa mm —, one has to operate with minimum *energy* of 3.1 J and three times *overlaps* or maximum *energy* of 5 J and two times *overlaps*. Where operating with the energy of 3.1 J requires cheaper laser, but an increase in the number of overlap from two to three rises the processing time by 50%, therefore, leading to the growth of cost of the laser treatment by 50% as well.
- Among the defined stress quantities, the highest effort is required for achieving the desired *stress at 0.01 mm*, and only possible when operating with 1×1 mm *optics*.
- Operating with 1×1 mm *optics* and the laser *energy* > 3 J, a number of *overlaps* > 2 times at the same time lead to the generation of high residual stresses which require a correction. As a result, the minimum compressive *stress at 0.5 mm* changes from -359 MPa to -332 MPa and the minimum *stress area* changes from -298 MPa mm to -265 MPa mm, which correspond to growth by 9% and 11%, respectively.

This study contributes to the understanding of the complex relationship between LSP parameters and induced residual stress profiles without investigating the intermediate processes, such as plasma generation and propagation of high pressure waves in the material. All these phenomena are included in the experimental data and modeled implicitly by the DOE.

Eventually, the LSP parameters achieved in the DOE study were used for the generation of desired residual stresses in the AA2024-T3 C(T)50 specimens. The main results are following:

- Significant retardation of the fatigue crack propagation leading to the fatigue life extension by a factor of 12 is primarily attributed to the crack closure effect under the cyclic loading which is caused by the deep compressive residual stresses in the LSP-treated area.
- LSP treatment conditions — 1.3 J, 2 overlaps and 3 J, 1 overlap — lead to comparable fatigue life extension by the factor of 11 and 12, respectively, in relation to the base material. According to the DOE study, this phenomenon is attributed to similar integral *stress area* values of generated stress profiles for these two cases.
- Hence, the desired fatigue life extension can be achieved by adjusting the LSP parameters for required integral *stress area* according to the established DOE regression model.

The current study provides a solid scientific basis for the tailored optimization of the LSP process. The generation of desired residual stress profiles in the metallic structures using the given LSP parameters, and the precise measurement of high stress profiles using the hole drilling will enhance the reproducibility of the fatigue life improvement; therefore, this will increase effectiveness of the treatment and reduce the cost of LSP performance.

In the present work, the potential of the LSP for the suppression of the fatigue crack growth was demonstrated on the laboratory scale. Therefore, the next step for the future work is to investigate the effect of LSP treatment on the fatigue crack growth behavior of the component-like specimens as they are typical for aircraft structures.

7. Bibliography

- [1] R. C. McClung , "A literature survey on the stability and significance of residual stresses during fatigue," *Fatigue & Fracture of Engineering Materials & Structures*, vol. 30, no. 3, pp. 173-205, 2007.
- [2] D. Ball and D. Lowry, "Experimental investigation on the effects of cold expansion of fastener holes," *Fatigue and Fracture of Engineering Materials and Structures* , vol. 21, no. 1, pp. 17-34, 1998.
- [3] K. Ding and L. Ye, *Laser shock peening. Performance and process simulation*, Cambridge: Woodhead Publishing, 2006.
- [4] G. S. Schajer, *Practical residual stress measurement methods*, Chichester: A John Wiley & Sons, Ltd, 2013.
- [5] D. Ball, "The influence of residual stress on the design of aircraft primary structure," *Journal of ASTM International* , vol. 5, no. 4, pp. 216-239, 2009.
- [6] X. Zhang, P. Irving, L. Edwards, M. Fitzpatrick, I. Sinclair and J. Lin, "The influence of residual stress on design and damage tolerance of welded aircraft structures," in *Proceedings of the 23rd ICAF Symposium of the International Committee on Aeronautical Fatigue*, Lausanne, 2005.
- [7] L. Edwards, M. E. Fitzpatrick, P. E. Irving, I. Sinclair, X. Zhang and D. Yapp, "An integrated approach to the determination and consequences of residual stress on the fatigue performance of welded aircraft structures," *Journal of ASTM International* , vol. 3, no. 2, pp. 1-17, 2006.
- [8] P. Irving, Y. E. Ma, X. Zhang, G. Servetti, S. Williams and G. Moore, "Control of crack growth rates and crack trajectories for enhanced fail safety and damage tolerance in welded structures," in *proceeding of the 25th ICAF Symposium of the Internationala Committee on Aeronautical Fatigue* , Rotterdam, 2009.
- [9] V. Richter-Trummer, S. Tavares, P. Moreira, M. de Figueiredo and P. de Castro, "Residual stress measurement using the contour and the sectioning methods in a MIG weld: Effects on the stress intensity factor," *Ciencia e Tecnologia dos Materials* , vol. 20, pp. 115-119, 2008.
- [10] D. Schnubel and N. Huber, "The influence of crack face contact on the prediction of fatigue crack propagation in residual stress fields," *Engineering Fracture Mechanics*, vol. 84, pp. 15-24, 2012.

- [11] L. Reid, "Sustaining an aging aircraft fleet with practical life enhancement methods," in *RTO-MP-079(ii) - Ageing Mechanisms and Control: Specialists' Meeting on Life Management Techniques for Ageing Air Vehicles*, Manchester, 2001.
- [12] Department of Defence USA, "Joint service specification guide aircraft structures," 2006.
- [13] Air Force Research Laboratory/VASM, Handbook for damage tolerance design, Dayton, OH, 2011.
- [14] M. McElhone and D. Rugg, "Experimental evaluation of the fatigue performance of aero-engine fan blade dovetails," in *Presentation for the AeroMat 2005*, 2005.
- [15] U. Heckenberger, E. Hombergsmeier, W. Bestenbostel and V. Holzinger, "LSP to improve the fatigue resistance of highly stressed AA7050 components," *Presentation for the 2nd International Conference on Laser Peening*, pp. 1-27, 2010.
- [16] O. Hatamleh, J. Lyons and R. Forman, "Laser and shot peening effects on fatigue crack growth in friction stir welded 7075-T7351 aluminium alloy joints," *International Journal of Fatigue*, vol. 29, no. 3, pp. 421-434, 2007.
- [17] O. Hatamleh, "A comprehensive investigation on the effects of laser and shot peening on fatigue crack growth in friction stir welded AA2195 joints," *International Journal of Fatigue*, vol. 31, no. 5, pp. 974-988, 2009.
- [18] S. Spanrad and J. Tong, "Characterisation of foreign object damage (FOD) and early fatigue crack growth in laser shock peened Ti-6Al-4V aerofoil specimens," *Materials Science and Engineering A*, vol. 528, no. 4-5, pp. 2128-2136, 2011.
- [19] G. S. Schajer, "Measurement of non-uniform residual stresses using the hole-drilling method. Part 1: stress calculation procedures," *Journal of engineering materials and technology ASME*, vol. 110, no. 4, pp. 338-343, 1988.
- [20] G. S. Schajer, "Measurement of non-uniform residual stresses using the hole-drilling method. Part 2: practical application of the Integral method," *Journal of engineering materials and technology ASME*, vol. 110, no. 4, pp. 344-349, 1988.
- [21] G. S. Schajer, "Hole-drilling and ring core methods," Fairmont Press, Lilburn, GA, 1996.
- [22] J. Lord, P. Re Grant and P. Whitehead, The measurement of residual stresses by the incremental hole drilling technique, Teddington, London: National Physical Laboratory, 2002.
- [23] E. M. Beaney, "Accurate measurement of residual stress on any steel using the centre hole drilling," *Strain*, vol. 12, no. 3, pp. 96-106, 1976.

-
- [24] F. Diaz, G. Kaufmann and G. Galizzi, "Determination of residual stresses using hole drilling and digital speckle pattern interferometry with automated data analysis," *Optics and Lasers in Engineering*, vol. 33, no. 1, pp. 39-48, 2000.
- [25] G. S. Schajer and J. I. Gazzarri, "Surface profiling using sequential sampling and inverse methods. Part I: Mathematical background," *Experimental Mechanics*, vol. 44, no. 5, pp. 473-479, 2004.
- [26] G. S. Schajer and M. Steinzig, "Full-field calculation of hole drilling residual stresses from electronic speckle pattern interferometry data," *Experimental Mechanics*, vol. 45, no. 6, pp. 526-532, 2005.
- [27] M. Beghini, L. Bertini and C. Santus, "A procedure for evaluating high residual stresses using the blind hole drilling method, including the effect of plasticity," *Journal of Strain Analysis for Engineering Design*, vol. 45, no. 4, pp. 301-318, 2010.
- [28] G. Cloud, *Optical methods of engineering analysis*, Cambridge: Cambridge University Press, 1995.
- [29] A. McDonach, J. McKelvie, P. MacKenzie and C. A. Walker, "Improved moiré interferometry and applications in fracture mechanics, residual stress and damaged composites," *Experimental Techniques*, vol. 7, no. 6, pp. 20-24, 1983.
- [30] M. Ya, H. Miao, X. Zhang and J. Lu, "Determination of residual stress by use of phase shifting moiré interferometry and hole-drilling method," *Optics and Lasers in Engineering*, vol. 44, no. 1, pp. 68-79, 2006.
- [31] R. Jones and C. Wykes, *Holographic and speckle interferometry*, 2nd ed, Cambridge: Cambridge University Press, 1989.
- [32] G. S. Schajer, "Application of finite element calculations to residual stress measurements," *Journal of engineering materials and technology ASME*, vol. 103, pp. 157-163, 1981.
- [33] R. Seifi and D. Salimi, "Effects of plasticity on residual stresses measurement by hole drilling method," *Mechanics of Materials*, vol. 53, pp. 72-79, 2012.
- [34] R. Moharami and I. Sattari-Far, "Experimental and numerical study of measuring high welding residual stresses by using the blind-hole-drilling technique," *Journal of Strain Analysis for Engineering Design*, vol. 43, no. 3, pp. 141-148, 2008.
- [35] G. Li, B. Liu and B. Li, "Influence of the hole-side plastic deformation as a result of the stress concentration on the accuracy of residual welding stress measurement by small blind hole relaxation method and its modification," in *Proceedings of the International Conference on Welding for Challenging Environments*, Toronto, ON, 1985.

- [36] Y. Traore, F. Hosseinzadeh and P. J. Bouchard, "Plasticity in the contour method of residual stress measurement," *Advanced Materials Research*, vol. 996, pp. 337-342, 2014.
- [37] F. Hosseinzadeh, Y. Traore, P. J. Bouchard and O. Muransky, "Mitigating cutting-induced plasticity in the contour method, part 1: experimental," *International Journal of Solids and Structures*, Vols. 94-95, pp. 247-253, 2016.
- [38] O. Muransky, C. J. Hamelin, F. Hosseinzadeh and M. B. Prime, "Mitigating cutting-induced plasticity in the contour method. Part 2: Numerical analysis," *International Journal of Solids and Structures*, Vols. 94-95, pp. 254-262, 2016.
- [39] S. Chupakhin, N. Kashaev and N. Huber, "Effect of elasto-plastic material behaviour on determination of residual stress profiles using the hole drilling method," *Journal of Strain Analysis for Engineering Design*, vol. 51, no. 8, pp. 572-581, 2016.
- [40] S. Chupakhin, N. Kashaev, B. Klusemann and N. Huber, "Artificial neural network for correction of effects of plasticity in equibiaxial residual stress profiles measured by hole drilling," *Journal of Strain Analysis for Engineering Design*, vol. 52, no. 3, pp. 137-151, 2017.
- [41] G. Totten, M. Howes and T. Inoue, *Handbook of residual stress and deformation of steel*, Materials Park, OH: ASM International, 2002.
- [42] P. J. Withers and H. K. Bhadeshia, "Residual stress, part 1: measurement techniques," *Materials, Science and Technology*, vol. 17, no. 4, pp. 355-365, 2001.
- [43] M. Kobayashia, T. Matsui and Y. Murakami, "Mechanism of creation of compressive residual stress by shot peening," *International Journal of Fatigue*, vol. 20, no. 5, pp. 351-357, 1998.
- [44] P. J. Withers, "Residual stress and its role in failure," *Reports on Progress in Physics*, vol. 70, no. 12, pp. 2211-2264, 2007.
- [45] G. S. Schajer, "Relaxation methods for measuring residual stresses: techniques and opportunities," *Experimental Mechanics*, vol. 50, no. 8, pp. 1117-1127, 2010.
- [46] K. Masubuchi, *Analysis of welded structures: residual stresses, distortion, and their consequences*, Kansas City, MO: Pergamon Press, 1980.
- [47] M. Sticchi, D. Schnubel, N. Kashaev and N. Huber, "Review of residual stress modification techniques for extending the fatigue life of metallic aircraft components," *Applied Mechanics Reviews*, vol. 67, no. 1, p. 9 pages, 2015.

- [48] L. Reid, "Sustaining an aging aircraft fleet with practical life enhancement methods," *Proceedings at the RTO applied vehicle technology panel specialists' meeting*, St. Joseph Print Group Inc., eds, vol. 32, pp. 1-10, 2003.
- [49] V. Schulze, *Modern mechanical surface treatment: states stability*, Weinheim: Wiley-VCH, 2006.
- [50] M. J. Pavier, C. G. C. Poussard and D. J. Smith, "Effect of residual stress around cold worked holes on fracture under superimposed mechanical load," *Engineering Fracture Mechanics*, vol. 63, no. 6, pp. 751-773, 1999.
- [51] L. Yongshou, S. Xiaojun, L. Jun and Y. Zhufeng, "Finite element method and experimental investigation on the residual stress fields and fatigue performance of cold expansion hole," *Materials & Design*, vol. 31, no. 3, pp. 1208-1215, 2010.
- [52] Q. Liu, P. Baburamani and C. Loader, "Effect of high temperature exposure on the mechanical properties of cold expanded open holes in 7050-T7451 aluminium alloy," Air Vehicles Division, DSTO Defence Science and Technology Organisation, Report No. DSTO-TN-0844, 2008.
- [53] Metal Improvement Company, "Shot Peening Applications, 9th ed.," Paramus, NJ, 2005.
- [54] S. Barter, L. Molent, K. Sharp and G. Clark, "Repair and life assessment of critical fatigue damaged aluminium alloy structure using a peening rework method," in *Proceedings of USAF ASIP Conference*, San Antonio, TX, 2000.
- [55] LAMBDA Technology Group, "Low plasticity burnishing," <http://www.lambdatechs.com/low-plasticity-burnishing-LPB.html> , February 27, 2017.
- [56] A. T. Bozdana, "On the mechanical surface enhancement techniques in aerospace industry – a review of technology," *Aircraft Engineering and Aerospace Technology*, vol. 77, no. 4, pp. 279-292, 2005.
- [57] N. Jayaraman, D. J. Hornbach and P. S. Prevey, "Mitigation of Fatigue and Pre-Cracking Damage in Aircraft Structures Through Low Plasticity Burnishing (LPB)," in *Proceedings of ASIP*, Palm Springs, CA, 2007.
- [58] D. Schnubel, M. Horstmann, V. Ventzke, S. Riekehr, P. Staron, T. Fischer and N. Huber, "Retardation of fatigue crack growth in aircraft aluminium alloys via laser heating – Experimental proof of concept," *Materials Science and Engineering: A*, vol. 546, pp. 8-14, 2012.

- [59] D. Schnubel and N. Huber, "Retardation of fatigue crack growth in aircraft aluminium alloys via laser heating – Numerical prediction of fatigue crack growth," *Computational Materials Science*, vol. 65, pp. 461-469, 2012.
- [60] D. Schnubel, M. Horstmann, P. Staron, T. Fischer and N. Huber, "Laser heating as approach to retard fatigue crack growth in aircraft aluminium structures," in *Proceedings of 1st International Conference of the International Journal of Structural Integrity*, Porto, 2012.
- [61] S. Soundarapandian and B. D. Narendra, "Laser surface hardening," in *Steel heat treating fundamentals and process*, Materials Park, OH, ASM International, 2013, pp. ASM Handbook, Vol. 4A.
- [62] C. Rubio-Gonzalez, C. Felix-Martinez, G. Gomez-Rosas, J. L. Ocana, M. Morales and J. A. Porro, "Effect of laser shock processing on fatigue crack growth of duplex stainless steel," *Materials Science and Engineering: A*, vol. 528, no. 3, pp. 914-919, 2011.
- [63] P. Peyre, R. Fabbro, P. Merrien and H. Lieurade, "Laser shock processing of aluminium alloys. Application to high cycle fatigue behaviour," *Materials Science and Engineering: A*, vol. 210, no. 1-2, pp. 102-113, 1996.
- [64] LSP Technology, "LaserPeen™ Process Overview," <http://www.lsp technologies.com/>, February 27, 2017.
- [65] A. H. Clauer and D. F. Lahrman, "Laser shock processing as a surface enhancement process," *Key Engineering Materials*, vol. 197, pp. 121-142, 2001.
- [66] C. Correa, L. Ruiz de Lara, M. Diaz, A. Gil-Santos, J. A. Porro and J. L. Ocana, "Effect of advancing direction on fatigue life of 316L stainless steel specimens treated by double-sided laser shock peening," *International Journal of Fatigue*, vol. 79, pp. 1-9, 2015.
- [67] T. J. Spradlin, "Process sequencing for fatigue life extension of large scale laser peened components," Wright State University, Dayton, OH,, PhD thesis, 2011.
- [68] G. Ivetic, I. Meneghin, E. Troiani, G. Molinari, J. Ocana, M. Morales, J. Porro, A. Lanciontti, V. Ristori, C. Polese, J. Plaisier and A. Lausi, "Fatigue in laser shock peened open-hole thin aluminium specimens," *Materials Science and Engineering: A*, vol. 534, pp. 573-579, 2012.
- [69] Y. Sano, T. Adachi, K. Akita, I. Altenberger, M. A. Cherif, B. Scholtes, K. Masaki, Y. Ochi and T. Inoue, "Enhancement of Surface Property by Low-Energy Laser Peening without Protective Coating," *Key Engineering Materials*, Vols. 345-346, pp. 1589-1592, 2007.

- [70] X. Zhang and Z. Wang, "Fatigue life improvement in fatigue-aged fastener holes using the cold expansion technique," *International Journal of Fatigue*, vol. 25, no. 9-11, pp. 1249-1257, 2003.
- [71] W. Z. Yan, X. S. Wang, H. S. Gao and Z. F. Yue, "Effect of split sleeve cold expansion on cracking behaviors of titanium alloy TC4 holes," *Engineering Fracture Mechanics*, vol. 88, pp. 79-89, 2012.
- [72] X. Song, W. C. Liu, J. P. Belnoue, J. Dong, G. H. Wu, W. J. Ding, S. A. J. Kimber, T. Buslaps, A. J. G. Lunt and A. M. Korsunsky, "An eigenstrain-based finite element model and the evolution of shot peening residual stresses during fatigue of GW103 magnesium alloy," *International Journal of Fatigue*, vol. 42, pp. 284-295, 2012.
- [73] G. H. Farrahi, G. H. Majzoobi, A. H. Mahmoudi and N. Habibi, "Fatigue life of shot peened welded tubular joint," in *Proceedings of the World Congress on Engineering, Vol 3*, London, 2012.
- [74] M. Aghaie-Khafri, M. Amin and A. H. Momeni, "Life assessment and life extension of an aircraft wheel," *Advances in Mechanical Engineering*, vol. 4, p. 6 pages, 2012.
- [75] S. Q. Jiang, J. Z. Zhou, Y. J. Fan, S. Huang and J. F. Zhao, "Prediction on Residual Stress and Fatigue Life of Magnesium Alloy Treated by Laser Shot Peening," *Materials Science Forum*, Vols. 626-627, pp. 393-398, 2009.
- [76] J. Z. Zhou, S. Huang, J. Sheng, J. Z. Lu, C. D. Wang, K. M. Chen, H. Y. Ruan and H. S. Chen, "Effect of repeated impacts on mechanical properties and fatigue fracture morphologies of 6061-T6 aluminum subject to laser peening," *Materials Science and Engineering: A*, vol. 539, pp. 360-368, 2012.
- [77] C. Ye, Y. Liao and G. J. Cheng, "Warm laser shock peening driven nanostructures and their effects on fatigue performance in aluminum alloy 6160," *Advanced Engineering Materials*, vol. 12, no. 4, pp. 291-297, 2010.
- [78] N. Kashaev, V. Ventzke, M. Horstmann, S. Chupakhin, S. Riekehr, R. Falck, E. Maawad, P. Staron, N. Schell and N. Huber, "Effects of laser shock peening on the microstructure and fatigue crack propagation behaviour of thin AA2024 specimens," *International Journal of Fatigue*, vol. 98, pp. 223-233, 2017.
- [79] S. Zabeen, M. Preuss and P. J. Withers, "Residual stresses caused by head-on and 45° foreign object damage for a laser shock peened Ti-6Al-4V alloy aerofoil," *Materials Science and Engineering: A*, vol. 560, pp. 518-527, 2013.

- [80] G. H. Majzoobi, K. Azadikhah and J. Nemati, "The effects of deep rolling and shot peening on fretting fatigue resistance of Aluminum-7075-T6," *Materials Science and Engineering: A*, vol. 516, no. 1-2, pp. 235-247, 2009.
- [81] V. Backer, F. Klocke, H. Wegner, A. Timmer, R. Grzhibovskis and S. Rjasanow, "Analysis of the deep rolling process on turbine blades using the FEM/BEM-coupling," in *IOP Conference Series: Materials Science and Engineering, Volume 10, Number 1*, Sydney, 2010.
- [82] C. M. Gill, N. Fox and P. J. Withers, "Shakedown of deep cold rolling residual stresses in titanium alloys," *Journal of Physics D: Applied Physics*, vol. 41, no. 17, p. 174005 (5 pages), 2008.
- [83] R. K. Shiue, C. T. Chang, M. C. Young and L. W. Tsay, "The effect of residual thermal stresses on the fatigue crack growth of laser-surface-annealed AISI 304 stainless steel: Part I: computer simulation," *Materials Science and Engineering: A*, vol. 364, no. 1-2, pp. 101-108, 2004.
- [84] C. D. Jang, H. C. Song and C. H. Lee, "Fatigue life extension of a through-thickness crack using local heating," in *Proceedings of the 12th International Offshore and Polar Engineering Conference*, Kitakyushu, 2002.
- [85] S. Bhamare, G. Ramakrishnan, S. R. Mannava, K. Langer and V. K. Vasudevan, "Simulation-based optimization of laser shock peening process for improved bending fatigue life of Ti-6Al-2Sn-4Zr-2Mo alloy," *Surface and Coatings Technology*, vol. 232, pp. 464-474, 2013.
- [86] M. Frija, R. B. Sghaier, C. Bouraoui and R. Fathallah, "Optimizing Residual Stress Profile Induced by Laser Shock Peening Using DOE Technique," *Applied Mechanics and Materials*, vol. 146, pp. 83-95, 2012.
- [87] T. V. Sibalija, S. Z. Petronic, V. D. Majstorovic and A. Milosavljevic, "Modelling and optimisation of laser shock peening using an integrated simulated annealing-based method," *The International Journal of Advanced Manufacturing Technology*, vol. 73, no. 5, pp. 1141-1158, 2014.
- [88] D. Sokol, A. Clauer, R. Ravindranath and D. F. Lahrman, "Applications of Laser Peening to Titanium Alloys," in *ASME/JSME 2004 Pressure Vessels and Piping Division Conference*, San Diego, CA, 2004.
- [89] M. Achintha, D. Nowell, D. Fufari, E. E. Sackett and M. R. Bache, "Fatigue behaviour of geometric features subjected to laser shock peening: Experiments and modelling," *International Journal of Fatigue*, vol. 62, pp. 171-179, 2014.

- [90] W. Braisted and R. Brockman, "Finite element simulation of laser shock peening," *International Journal of Fatigue*, vol. 21, no. 7, pp. 719-724, 1999.
- [91] N. Hfaiedh, P. Peyre, H. Song, I. Popa, V. Ji and V. Vignal, "Finite element analysis of laser shock peening of 2050-T8 aluminum alloy," *International Journal of Fatigue*, vol. 70, pp. 480-489, 2015.
- [92] C. Cellard, D. Reiraint, M. Francois, E. Rouhaud and D. Saunier, "Laser shock peening of Ti-17 titanium alloy: Influence of process parameters," *Materials Science and Engineering A*, vol. 532, pp. 362-372, 2012.
- [93] A. Warren, Y. Guo and S. Chen, "Massive parallel laser shock peening: Simulation, analysis, and validation," *International Journal of Fatigue*, vol. 30, no. 1, pp. 188-197, 2008.
- [94] M. Ebrahimi, S. Amini and S. Mahdavi, "The investigation of laser shock peening effects on corrosion and hardness properties of ANSI 316L stainless steel," *The International Journal of Advanced Manufacturing Technology*, vol. 88, no. 5, pp. 1557-1565, 2017.
- [95] H. Kamkarrad, S. Narayanswamy and M. Keshmiri, "High repetition laser shock peening on magnesium based biodegradable alloys," *Journal of Laser Micro/Nanoengineering*, vol. 10, no. 3, pp. 291-297, 2015.
- [96] U. Trdan, J. Ocana and J. Grum, "Surface modification of aluminium alloys with laser shock processing," *Journal of Mechanical Engineering*, vol. 57, no. 5, pp. 385-393, 2011.
- [97] A. T. DeWald and M. R. Hill, "Eigenstrain-based model for prediction of laser peening residual stresses in arbitrary three-dimensional bodies," *Journal of Strain Analysis for Engineering Design*, vol. 44, no. 1, pp. Part 1:1-11, Part 2:13-27, 2009.
- [98] G. S. Schajer and M. B. Prime, "Use of inverse solutions for residual stress measurements," *Journal of Engineering Materials and Technology*, vol. 128, no. 3, pp. 375-382, 2006.
- [99] J. Lu, Handbook of measurement of residual stresses, Lilburn: Fairmont, 1996.
- [100] G. S. Schajer, "Residual stresses: measurement by destructive methods," in *Encyclopedia of Materials: Science and Technology, Section 5a*, Oxford, Elsevier Science, 2001.
- [101] M. B. Prime, "Residual stress measurement by successive extension of a slot: the crack compliance method," *Applied Mechanics Reviews*, vol. 52, no. 2, pp. 75-96, 1999.
- [102] W. Cheng and I. Finnie, Residual stress measurement and the slitting method, New York: Springer, 2007.

- [103] M. B. Prime, "Cross-sectional mapping of residual stresses by measuring the surface contour after a cut," *Journal of Engineering Materials and Technology*, vol. 123, no. 2, pp. 162-168, 2001.
- [104] A. T. DeWald and M. R. Hill, "Multi-axial contour method for mapping residual stresses in continuously processed bodies," *Experimental Mechanics*, vol. 46, no. 4, pp. 473-490, 2006.
- [105] P. Pagliaro, "Mapping multiple residual stress components using the contour method and superposition," Universita Degli Studi di Palermo, PhD thesis, 2008.
- [106] P. Pagliaro, M. B. Prime, H. Swenson and B. Zuccarello, "Measuring multiple residual-stress ccomponents using the contour method and multiple cuts," *Experimental Mechanics*, vol. 50, no. 2, pp. 187-194, 2010.
- [107] American Society for Testing and Materials (ASTM), "Standard test method for determining residual stresses by the hole-drilling strain-gage method, standard test method E837-08," American Society for Testing and Materials, West Conshohocken, PA, 2008.
- [108] Measurements Group, "Measurement of residual stresses by hole-drilling strain gage method, Tech note TN-503-6," Vishay Measurements Group, Raleigh, NC., 2001.
- [109] P. V. Grant, J. D. Lord and P. S. Whitehead, The measurement of residual stresses by the incremental hole drilling technique, Measurement good practice guide. No.53, National Physical Laboratory, UK, 2002.
- [110] S. Kiel, "Experimental determination of residual stresses with the ring-core method and an on-Line measuring system," *Experimental Techniques*, vol. 16, no. 5, pp. 17-24, 1992.
- [111] A. Ajovalasit, G. Petrucci and B. Zuccarello, "Determination of non-uniform residual stresses using the ring-core method," *Journal of Engineering Materials and Technology*, vol. 118, no. 2, pp. 224-228, 1996.
- [112] P. Sarga and F. Menda, "Comparison of ring-core method and hole-drilling method used for determining residual stresses," *American Journal of Mechanical Engineering*, vol. 1, no. 7, pp. 335-338, 2013.
- [113] American Society for Testing and Materials (ASTM) International, "E 837-13. Standart test method for determination residual stresses by the hole-drilling strain-gage method," American Society for Testing and Materials (ASTM) International, West Conshohocken, PA , 2013.
- [114] H. Boyer, Atlas of fatigue curves, ASM International, 1986.

- [115] M. Mitchell, *Fundamentals of Modern Fatigue Analysis for Design, Fatigue and Fracture*, 19: ASM International, 1996.
- [116] C. Correa, L. Ruiz de Lara, M. Diaz, J. A. Porro, A. Garcia-Beltran and J. L. Ocana, "Influence of pulse sequence and edge material effect on fatigue life of Al2024-T351 specimens treated by laser shock processing," *International Journal of Fatigue*, vol. 70, pp. 196-204, 2015.
- [117] M. Janssen, J. Zuidema and R. Wanhill, *Fracture Mechanics*, Delft: Spon Press, 2004.
- [118] G. Servetti and X. Zhang, "Predicting fatigue crack growth rate in a welded butt joint: The role of effective R ratio in accounting for residual stress effect," *Engineering Fracture Mechanics*, vol. 76, no. 11, pp. 1589-1602, 2009.
- [119] A. P. Parker, "Stress Intensity Factors, Crack Profiles, and Fatigue Crack Growth Rates in Residual Stress Fields," *ASTM STP*, vol. 776, pp. 13-31, 1982.
- [120] C. D. Liljedahl, O. Zanellato, M. E. Fitzpatrick, J. Lin and L. Edwards, "The effect of weld residual stresses and their re-distribution with crack growth during fatigue under constant amplitude loading," *International Journal of Fatigue*, vol. 32, no. 4, pp. 735-743, 2010.
- [121] Y. Lee, C. Chung, Y. Park and H. Kim, "Effects of redistributing residual stress on the fatigue behaviour of SS330 weldment," *International Journal of Fatigue*, vol. 20, pp. 565-573, 1998.
- [122] C. Gardin, S. Courtin, G. Bezzine, D. Bertheau and H. Hamouda, "Numerical simulation of fatigue crack propagation in compressive residual stress fields of notched round bars," *Fatigue and Fracture of Engineering Materials and Structures*, vol. 30, pp. 231-242, 2007.
- [123] M. H. Gozin and M. Aghaie-Khafri, "2D and 3D finite element analysis of crack growth under compressive residual stress field," *International Journal of Solids and Structures*, vol. 49, no. 23-24, pp. 3316-3322, 2012.
- [124] J. Sheng, S. Huang, J. Zhou, S. Xu, S. Xu and H. Zhang, "Effect of laser peening with different energies on fatigue fracture evolution of 6061-T6 aluminum alloy," *Optics & Laser Technology*, vol. 77, pp. 169-176, 2016.
- [125] S. Zabeen, M. Preuss and P. Withers, "Evolution of a laser shock peened residual stress field locally with foreign object damage and subsequent fatigue crack growth," *Acta Materialia*, vol. 83, pp. 216-226, 2015.
- [126] J. Zhao, Y. Dong and C. Ye, "Laser shock peening induced residual stresses and the effect on crack propagation behavior," *International Journal of Fatigue*, Vols. 100, 1, pp. 407-417, 2017.

- [127] G. Yoder, L. Cooley and T. Crooker, "Quantitative analysis of microstructural effects on fatigue crack growth in widmanstätten Ti-6Al-4V and Ti-8Al-1Mo-1V," *Engineering Fracture Mechanics*, vol. 11, no. 4, pp. 805-816, 1979.
- [128] M.-Z. Ge and J.-Y. Xiang, "Effect of laser shock peening on microstructure and fatigue crack growth rate of AZ31B magnesium alloy," *Journal of Alloys and Compounds*, vol. 680, pp. 544-552, 2016.
- [129] ASM Aerospace Specification Metals Inc, "Aluminum 2024-T3," <http://asm.matweb.com/search/SpecificMaterial.asp?bassnum=MA2024T3>, 2007, accessed 28 February 2017.
- [130] Z. Huda, N. I. Taib and T. Zaharinie, "Characterization of 2024-T3: An aerospace aluminum alloy," *Materials Chemistry and Physics*, vol. 113, no. 2-3, pp. 515-517, 2009.
- [131] E. P. DeGarmo, J. T. Black and R. A. Kohser, *Materials and processes in manufacturing*. 9th ed., John Wiley & Sons, Inc: New York, 2003.
- [132] H. Kacar, E. Atik and C. Meric, "The effect of precipitation-hardening conditions on wear behaviours at 2024 aluminium wrought alloy," *Journal of Materials Processing Technology*, vol. 142, no. 3, pp. 762-766, 2003.
- [133] J. Enz, V. Khomenko, S. Riekehr, V. Ventzke, N. Huber and N. Kashaev, "Single-sided laser beam welding of a dissimilar AA2024-AA7050 T-joint," *Materials & Design*, vol. 76, pp. 110-116, 2015.
- [134] M. Steinzig and E. Ponslet, "Residual stress measurement using the hole drilling method and laser speckle interferometry: part 1," *Experimental techniques SEM*, vol. 27, no. 3, pp. 43-46, 2003.
- [135] ASTM E647-05, "Standard test method for measurement of fatigue crack growth rates," 2005.
- [136] C. F. Jeff Wu, *Experiments. Planning, analysis, and parameter design optimization*, New York: John Wiley and Sons, Inc, 2000.
- [137] D. C. Montgomery, *Design and analysis of experiments*, 5th ed., New York: John Wiley & Sons, Inc., 2001.
- [138] G. E. Box, W. G. Hunter and J. S. Hunter, *Statistics for experimenters*, New York: John Wiley & Sons, Inc., 1978.
- [139] W. Q. Meeker and L. A. Escobar, *Statistical methods for reliability data*, New York: John Wiley & Sons, Inc., 1998.

-
- [140] ReliaSoft Corporation, Experiment design & analysis reference, Tucson, AZ: ReliaSoft Publishing, 2015.
- [141] ReliaSoft, User's guide DOE++, ReliaSoft Publishing, 2014.
- [142] C. F. J. Wu and M. Hamada, Experiments: planning, analysis and parameter design optimization, New York: John Wiley & Sons, Inc., 2000.
- [143] ReliaSoft Corporation, Quick start guide, Tucson: ReliaSoft Publishing, 2015.
- [144] G. S. Schajer, "Advances in hole-drilling residual stress measurements," *Experimental Mechanics*, vol. 50, no. 2, pp. 159-168, 2010.
- [145] MSC software, Partan user's guide, Santa Ana, CA: MSC software, 2012.
- [146] Dassault Systemes, ABAQUS 6.13 user's manual, Velizy-Villacoublay: Dassault Systemes, 2013.
- [147] M. Lutz, Learning python, Sebastopol, CA: O'Reilly Media, 2009, p. 1216.
- [148] S. Haykin, A comprehensive foundation, New York: Pearson education , 1998.
- [149] G. Yagawa and H. Okuda, "Neural networks in computational mechanics," *Archives of Computational Methods in Engineering*, vol. 3, no. 4, pp. 435-512, 1996.
- [150] R. Willumeit, F. Feyerabend and N. Huber, "Magnesium degradation as determined by artificial neural networks," *Acta Biomaterialia*, vol. 9, no. 10, pp. 8722-8729, 2013.
- [151] N. Huber and C. Tsakmakis, "Determination of constitutive properties from spherical indentation data using neural networks. Part i: the case of pure kinematic hardening in plasticity laws," *Journal of the Mechanics and Physics of Solids*, vol. 47, no. 7, pp. 1569-1588, 1999.
- [152] N. Huber and C. Tsakmakis, "Determination of constitutive properties from spherical indentation data using neural networks. Part ii: plasticity with nonlinear isotropic and kinematic hardening," *Journal of the Mechanics and Physics of Solids*, vol. 47, no. 7, pp. 1589-1607, 1999.
- [153] N. Huber, I. Tsagrakis and C. Tsakmakis, "Determination of constitutive properties of thin metallic films on substrates by spherical indentation using neural networks," *International Journal of Solids and Structures*, vol. 37, no. 44, pp. 6499-6516, 2000.

- [154] N. Huber, A. Konstantinidis and C. Tsakmakis, "Determination of Poisson's ratio by spherical indentation using neural networks: Part I. Theory," *Journal of Applied Mechanics ASME*, vol. 68, no. 2, pp. 218-223, 2001.
- [155] N. Huber and C. Tsakmakis, "Determination of Poisson's ratio by spherical indentation using neural networks. Part II: identification method," *Journal of Applied Mechanics*, vol. 68, no. 2, pp. 224-229, 2001.
- [156] N. Huber, W. D. Nix and H. Gao, "Identification of elastic-plastic material parameters from pyramidal indentation of thin films," *Proceedings of the Royal Society A*, vol. 458, no. 2023, pp. 1593-1620, 2002.
- [157] E. Tyulyukovskiy and N. Huber, "Identification of viscoplastic material parameters from spherical indentation data: Part I. Neural networks," *Journal of Materials Research*, vol. 21, no. 3, pp. 664-676, 2006.
- [158] M. Riedmiller and H. Braun, "A direct adaptive method for faster backpropagation learning: the RPROP algorithm," in *IEEE International Conference on Neural Networks*, San Francisco, 1993.
- [159] C. Correa, D. Peral, J. Porro, M. Diaz, L. Ruiz de Lara, A. Garcia-Beltran and J. L. Ocana, "Random-type scanning patterns in laser shock peening without absorbing coating in 2024-T351 Al alloy: A solution to reduce residual stress anisotropy," *Optics and Laser Technology*, vol. 73, pp. 179-187, 2015.
- [160] J. L. Ocana, C. Correa, A. Garcia-Beltran, J. A. Porro, M. Diaz, L. Ruiz-de-Lara and D. Peral, "Laser Shock Processing of thin Al2024-T351 plates for induction of through-thickness compressive residual stresses fields," *Journal of materials processing technology*, vol. 223, pp. 8-15, 2015.

Appendix

Table A1 Summary of designed experiments

Number of experiments	Run order	A: Optics, mm	B: Overlap, number	C: Energy, J	Stress area, MPa mm	Stress at 0.01 mm, MPa	Stress at 0.5 mm, MPa
1	39	1	1	1.3	-160	24	-201
2	48	1	1	1.3	-155	23	-181
3	53	1	1	1.3	-262	-71	-304
4	1	1	2	1.3	-231	-46	-271
5	11	1	2	1.3	-219	-29	-300
6	13	1	2	1.3	-151	-3	-168
7	18	1	3	1.3	-271	-81	-374
8	37	1	3	1.3	-251	-43	-300
9	44	1	3	1.3	-	-	-
10	19	1	1	3	-210	-7	-258
11	21	1	1	3	-	-	-
12	24	1	1	3	-220	-34	-304
13	4	1	2	3	-313	-116	-411
14	29	1	2	3	-	-	-
15	34	1	2	3	-291	-70	-390
16	9	1	3	3	-161	-2	-214
17	17	1	3	3	-302	-143	-384
18	22	1	3	3	-298	-120	-371
19	6	1	1	5	-220	-46	-289
20	14	1	1	5	-204	-17	-275
21	33	1	1	5	-	-	-
22	45	1	2	5	-298	-149	-365
23	47	1	2	5	-280	-108	-359
24	54	1	2	5	-303	-164	-398
25	12	1	3	5	-300	-197	-321
26	31	1	3	5	-294	-117	-382
27	35	1	3	5	-260	-78	-310
28	5	3	1	1.3	7	51	41
29	7	3	1	1.3	7	51	41
30	30	3	1	1.3	7	51	41
31	16	3	2	1.3	7	51	41
32	42	3	2	1.3	7	51	41

Table A1 Summary of designed experiments

Number of experiments	Run order	A: Optics, mm	B: Overlap, number	C: Energy, J	<i>Stress area,</i> MPa mm	<i>Stress at 0.01 mm,</i> MPa	<i>Stress at 0.5 mm,</i> MPa
33	52	3	2	1.3	7	51	41
34	8	3	3	1.3	7	51	41
35	50	3	3	1.3	7	51	41
36	51	3	3	1.3	7	51	41
37	2	3	1	3	-43	43	-31
38	20	3	1	3	-65	59	-52
39	38	3	1	3	-54	52	-51
40	3	3	2	3	-93	10	-110
41	27	3	2	3	-78	63	-96
42	41	3	2	3	-100	19	-128
43	28	3	3	3	-96	-5	-122
44	40	3	3	3	-103	13	-126
45	49	3	3	3	-82	80	-103
46	10	3	1	5	-80	21	-111
47	23	3	1	5	-74	89	-97
48	43	3	1	5	-102	-18	-118
49	26	3	2	5	-144	-4	-200
50	32	3	2	5	-172	-31	-223
51	46	3	2	5	-163	-10	-194
52	15	3	3	5	-202	-25	-252
53	25	3	3	5	-233	-13	-299
54	36	3	3	5	-180	-38	-222

Table A2 Summary of designed experiments which required correction.

Number	Run order	Optics, mm	Overlap, number	Energy, J	Stress area, MPa mm		Stress at 0.01 mm, MPa		Stress at 0.5 mm, MPa	
					Orig.	Corr.	Orig.	Corr.	Orig.	Corr.
1	4	1	2	3	-313	-274	-116	-116	-411	-357
2	34	1	2	3	-291	-270	-70	-70	-390	-362
3	17	1	3	3	-302	-274	-143	-143	-384	358
4	22	1	3	3	-298	268	-120	-120	-371	-347
5	45	1	2	5	-298	-271	-149	-149	-365	-351
6	47	1	2	5	-280	-254	-108	-108	-359	-345
7	54	1	2	5	-303	-275	-164	-164	-398	-362
8	12	1	3	5	-300	-272	-197	-197	-321	-310
9	31	1	3	5	-294	-269	-117	-117	-382	-341
10	35	1	3	5	-260	-237	-78	-78	-310	-303

List of publications

Journals

S. Chupakhin, N. Kashaev, B. Klusemann and N. Huber. “Artificial neural network for correction of effects of plasticity in equibiaxial residual stress profiles measured by hole drilling,” *Journal of Strain Analysis for Engineering Design*, vol.52, no. 3, pp. 137–151, 2017.

S. Chupakhin, N. Kashaev and N. Huber. “Effect of elasto-plastic material behaviour on determination of residual stress profiles using the hole drilling method,” *Journal of Strain Analysis for Engineering Design*, vol. 51, no. 8, pp. 572–581, 2016.

N. Kashaev, V. Ventzke, M. Horstmann, S. Chupakhin, S. Riekehr, R. Falck, E. Maawad, P. Staron, N. Schell and N. Huber. “Effects of laser shock peening on the microstructure and fatigue crack propagation behaviour of thin AA2024 specimens,” *International Journal of Fatigue*, vol. 98, pp. 223–233, 2017.

Conferences

S. Chupakhin, N. Kashaev and N. Huber. “Effect of elastic-plastic material behaviour on determination of laser shock peening induced residual stress profiles using the hole drilling method,” Oral presentation at the *5th International Conference on Laser Peening and Related Phenomena*, Cincinnati, 2015.

S. Chupakhin, N. Kashaev, B. Klusemann and N. Huber. “Application of neural network for correction of hole drilling plasticity effect when measuring LSP induced residual stresses,” Oral presentation at the *6th International Conference on Laser Peening and Related Phenomena*, Pretoria and Skukuza, 2016.

Curriculum vitae

Family name	Chupakhin
Given name	Sergey
Nationality	Russian Federation
Date of birth	28.09.1989
Place of birth	Kursk, Russia
09/1996–06/2005	Primary and secondary school in Kursk
09/2005–06.2007	High school in Kursk
09/2007–08/2011	Bauman Moscow State Technical University, Bachelor's degree in Power Engineering
09/2011–06/2013	Bauman Moscow State Technical University, Master of Science in Power Engineering
08/2013–12/2017	Helmholtz-Zentrum Geesthacht, Zentrum für Material- und Küstenforschung GmbH, PhD student in the department of Joining and Assessment in the Institute of Materials Research, Materials Mechanics